Mid-Infrared Pulse Shaping and Two-Dimensional Spectroscopy of Open Quantum Systems in Liquid Solution

by

Matthew R Ross

A dissertation submitted in partial fulfillment
of the requirements for the degree of
Doctor of Philosophy
(Applied Physics)
in The University of Michigan
2012

Doctoral Committee:

Assistant Professor Kevin J. Kubarych, Chair
Professor Eitan Geva
Professor Roseanne J. Sension
Assistant Professor Jennifer P. Ogilvie

For my wife Katie.

TABLE OF CONTENTS

LIST OF FIGURES

Figure

LIST OF TABLES

Table

CHAPTER I

Introduction

Chemical reactions involve dynamic time scales spanning many orders of magnitude. Protein folding may take milliseconds to hours,[1] whereas the underling hydrogen bond dynamics holding proteins together have a typical time scale of picoseconds.[2;3]. That is as much as a 13 order-of-magnitude difference. Diamonds convert to graphite over millions of years[4] and charge transfer reactions can occur on very fast timescales.[5;6] The challenge of such disparate time scales confronts both theory and experiment. Multi-dimensional (MD) infrared spectroscopy can help reveal system dynamics over femtosecond to hundreds of picosecond or longer timescales.[7]

In this work, I will discuss the use of two-dimensional infrared (2DIR) to address several basic questions: How can we understand strong system-bath coupling? How much detail can be extracted about the Hamiltonian of a reacting system? How well can the complicated dynamics of a reaction be simplified to basic concepts such as viscosity, friction, and a reaction coordinate? Our lab's two-dimensional infrared (2DIR) equilibrium and non-equilibrium spectroscopy and the proposed mid-IR pulse shaping allow us to address these questions.

A significant part of this work was the development of a pulse shaping based 2DIR system. While pulse shaping in the visible and near-IR has been in use for some time[8–10], materials and technology development has only recently allowed direct

pulse shaping in the mid-infrared spectral region.[11–13] Not only does our shaper allow for 2DIR measurements, but it also allows for expansion of experimental techniques new to mid-infrared spectroscopy which were previously limited to higher optical frequencies. For example, coherent control[14–16], quantum process tomagraphy,[17;18] and a spectroscopy based on Schrödinger's cat state spectroscopy[19;20] are all possible. Information gathered from these experiments will aid in understanding of many system vibrational Hamiltonians and could inform the design of new molecular systems such as metaloenzymes, as will be discussed later.

1.1 Background on Techniques

The ability to better understand solution-solvent dynamics[21;22] and structural information, as told by vibrational coupling[7;23;24] are two significant areas of current research in condensed phase systems. MD spectroscopy can improve our understanding of solution phase reactions, solvent dynamics and internal system dynamics.

1.1.1 Linear Spectroscopy

Dispersing of light and subsequent analysis of the spectrum has a long history[25] and has lead to many profound achievements in science.[25] Even quantum theory owes its existence in part to the observation of discrete lines within linear spectrum. Many early spectra were taken using non-coherent light sources over a broad range of wavelengths with minimal spectral resolution. However, eventually technological advances such as lasers allowed researchers to determine that it is often more convenient to consider the time-dependent response to a pulse of light. Pump-probe spectroscopy and Fourier transform spectroscopy are two examples of this which are both used, to different ends, in modern spectroscopic research.

For the first order single field interaction system response we have the polarization given by Zanni[26] in the rotating wave approximation with our laser field within the

retime of linear system response

$$P^{(1)}(t) = \int_0^\infty E(t-\tau)R^{(1)}(\tau)d\tau. \quad (1.1)$$

Due to this interpretation of $R^{(n)}$ as the nth response, $P^{(n)}(t)$ is typically referred to as the n^{th}-order, time-dependent polarization. Under some additional approximations, we simplify this to the nth-order response function, given the symbol $R^{(n)}$. The Fourier transform of the $n = 1$ impulse response gives the frequency-dependent complex-valued response function, which associated with normal linear absorption spectra (real part) and refraction (imaginary part).

After such a linear spectrum is obtained, one can work to get the most information that is possible from interpretation of the spectrum. The spectrum will give the energy levels, relative strengths, and line shapes of allowed absorptions. The liquid-phase solvent environment has many possible configurations, as such there will be fluctuations in the environment of any given system. These fluctuations induce subsequent fluctuations in $R^{(n)}$ and thus the spectrum. The nature of these fluctuations gives rise to the line shapes seen in linear spectra of condensed phase systems. One can attempt analyzing the shape of peaks to extract model-dependent information, such as with Kubo's stochastic theory of line shapes[27]. However, the similarity of line shapes arising from disparate mechanisms makes unambigous interpretation of line shapes difficult. For example, a glass-forming systems with varying amounts of both fast β reorientation and slower α reorientation cam all show the same linear spectra line shape.[3]

1.2 Higher Order Spectroscopies

Consider the third-order optical response as The instantaneous non-linear material polarization is given by

$$\begin{aligned}\vec{P}^{(3)}(t) \quad \propto \quad & \int_0^\infty \int_0^\infty \int_0^\infty E_3(t-\tau_3)E_2(t-\tau_3-\tau_2) \times \\ & E_1(t-\tau_3-\tau_2-\tau_1)R^{(3)}(\tau_3,\tau_2,\tau_1)d\tau_1 d\tau_2 d_{\tau_3} \end{aligned} \tag{1.2}$$

with τ_1, τ_2, and τ_3 integration variables.

We can define the system response in terms of the system density matrix. Following the derivation of Boyd,[28] for the case of a small energetic perturbation, $\rho^{(3)}_{nm}$, of the system due to the presence of light we have the perturbation

$$\rho^{(3)}_{nm} \quad = \quad e^{-(i\omega_{nm}+\gamma_{nm})t} \int_{-\infty}^{t} \frac{-i}{\hbar} \left[\hat{V}, \hat{\rho}^{(2)}\right]_{nm} e^{(i\omega_{nm}+\gamma_{nm})\tau} d\tau, \tag{1.3}$$

Using the notation of Boyd, with the integration variable changed to τ and the second order perturbation, $\rho^{(2)}_{\nu m}$ is given by Boyd's equation (3.6.7). Since our system potential is

$$\hat{V} \quad = \quad -\vec{\mu} \cdot \vec{E}(t) \tag{1.4}$$

We can simplify the commutator as

$$\left[\hat{V}, \hat{\rho}^{(2)}\right]_{nm} \quad = \quad -\sum_{\nu} \left(\mu_{n\nu}\rho^{(2)}_{\nu m} - \rho^{(2)}_{n\nu}\mu_{\nu m}\right) \cdot \vec{E}(t). \tag{1.5}$$

With some rearrangement, this gives

$$\begin{aligned}\rho^{(3)}{}_{+nm} &= \frac{1}{\hbar}\sum_{\nu l}\sum_{pqr}\left[\frac{\mu_{n\nu}\cdot\vec{E}(\omega_r)K_{\nu ml}}{\omega_{nm}-\omega_p-\omega_q-\omega_r-i\gamma_{nm}}\right. \\ &= \left.-\frac{\mu\cdot\vec{E}(\omega_r)K_{n\nu l}}{\omega_{nm}-\omega_p-\omega_q-\omega_r-i\gamma_{nm}}\right] \end{aligned} \tag{1.6}$$

Since the third order polarization is given by

$$\begin{aligned}P_i(\omega_o+\omega_n+\omega_m) &= \sum_{ijl}\sum_{(mno)}\chi^{(3)}(\omega_o+\omega_n+\omega_m,\omega_o,\omega_n,\omega_m) \\ &= \times\vec{E}_j(\omega_o)\vec{E}_k(\omega_n)\vec{E}_l(\omega_m)\end{aligned} \tag{1.7}$$

We can get the third order susceptibility, $\chi^{(3)}$ as

$$\chi^{(3)}_{kjih}(\omega_1+\omega_2+\omega_3,\omega_3,\omega_2,\omega_1) = \frac{N}{\hbar^3}\mathcal{P}_I\sum_{\nu nml}\rho^{(0)}_{ll}\times\Big\{$$

$$\frac{\mu^k_{l\nu}\mu^j_{\nu n}\mu^i_{nm}\mu^h_{ml}}{(\omega_{\nu l}-\omega_1-\omega_2-\omega_3-i\gamma_{\nu l})(\omega_{nl}-\omega_1-\omega_2-i\gamma_{nl})(\omega_{ml}-\omega_1-i\gamma_{ml})}+ \tag{1.8a}$$

$$\frac{\mu^h_{l\nu}\mu^k_{\nu n}\mu^j_{nm}\mu^i_{ml}}{(\omega_{n\nu}-\omega_1-\omega_2-\omega_3-i\gamma_{n\nu})(\omega_{m\nu}-\omega_p-\omega_2-i\gamma_{m\nu})(\omega_{\nu l}+\omega_1+i\gamma_{\nu l})}+ \tag{1.8b}$$

$$\frac{\mu^i_{l\nu}\mu^k_{\nu n}\mu^j_{nm}\mu^h_{ml}}{(\omega_{n\nu}-\omega_1-\omega_2-\omega_3-i\gamma_{n\nu})(\omega_{\nu m}+\omega_1+\omega_2+i\gamma_{\nu m})(\omega_{ml}-\omega_1-i\gamma_{ml})}+ \tag{1.8c}$$

$$\frac{\mu^h_{l\nu}\mu^i_{\nu n}\mu^k_{nm}\mu^j_{ml}}{(\omega_{m\nu}-\omega_1-\omega_2-\omega_3-i\gamma_{mn})(\omega_{nl}+\omega_1+\omega_2+i\gamma_{nl})(\omega_{\nu l}+\omega_1+i\gamma_{\nu l})}+ \tag{1.8d}$$

$$\frac{\mu^j_{l\nu}\mu^k_{\nu n}\mu^i_{nm}\mu^h_{ml}}{(\omega_{\nu n}+\omega_1+\omega_2+\omega_3+i\gamma_{\nu n})(\omega_{nl}-\omega_1-\omega_2-i\gamma_{nl})(\omega_{ml}-\omega_1-i\gamma_{ml})}+ \tag{1.8e}$$

$$\frac{\mu^h_{l\nu}\mu^j_{\nu n}\mu^k_{nm}\mu^i_{ml}}{(\omega_{nm}+\omega_1+\omega_2+\omega_3+i\gamma_{nm})(\omega_{m\nu}-\omega_1-\omega_2-i\gamma_{m\nu})(\omega_{\nu l}+\omega_1+i\gamma_{\nu l})}+ \tag{1.8f}$$

$$\frac{\mu^i_{l\nu}\mu^j_{\nu n}\mu^k_{nm}\mu^h_{ml}}{(\omega_{nm}-\omega_1+\omega_2+\omega_3-i\gamma_{nm})(\omega_{\nu m}+\omega_1+\omega_2+i\gamma_{m\nu})(\omega_{ml}-\omega_1-i\gamma_{ml})}+ \tag{1.8g}$$

$$\frac{\mu^h_{l\nu}\mu^i_{\nu n}\mu^j_{nm}\mu^k_{ml}}{(\omega_{ml}+\omega_1+\omega_2+\omega_3+i\gamma_{ml})(\omega_{nl}+\omega_1+\omega_2+i\gamma_{nl})(\omega_{\nu l}+\omega_1+i\gamma_{\nu l})}\Big\}, \tag{1.8h}$$

where we will take $\vec{E}_1$, $\vec{E}_2$, and $\vec{E}_3$ to be three coincident electric fields or optical pulses. Consider these three laser pulses with wavevectors $\vec{k}_1$, $\vec{k}_2$, and $\vec{k}_3$ incident on

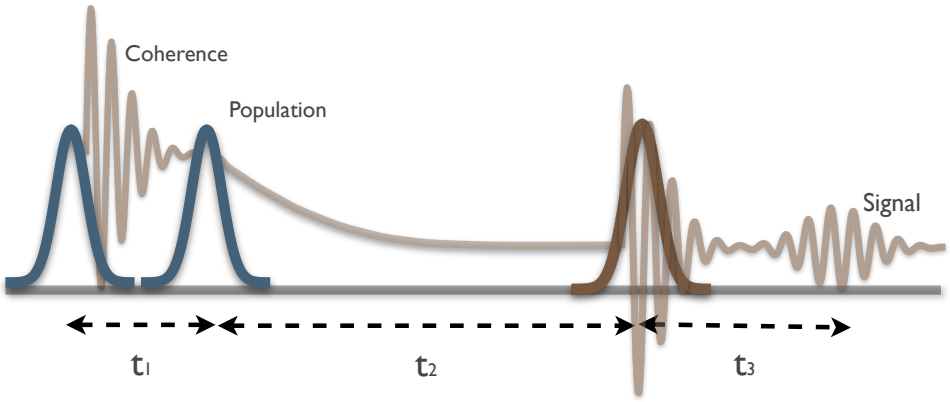

Figure 1.1: Pulse sequence for two-dimensional spectroscopy. Pulse $\vec{E}_1$ puts the system into a coherence between the ground state and the target state. Pulse $\vec{E}_2$ locks in a population a time t_1 later. After a waiting time t_2, between 0 and a few hundred ps, pulse $\vec{E}_3$ returns the system to a coherence which emits the signal $\vec{E}_{sig}$ after a time t_3.

a sample with frequencies ω_1, ω_2, ω_2 at, or near, resonance with one of the energy levels $E_\nu \geq E_n \geq E_m \geq E_l$. We have used the permutation operator $\mathcal{P}_I$, this results in a total of 48 terms. Naturally, there is a great deal of simplification if some or all of ω_1, ω_2 and ω_3 are not unique. However, such degenerate cases would not allow full consideration of all possible system paths in a system with third-order response. The main point to take from this expression is that there is a complicated dependance of the third order response on the excitation energies $(\omega_p, \omega_q, \omega_r)$, the system polarizapility (in $\vec{\rho}^{(0)}$), and the dipoles $(\vec{\mu})$.

1.2.1 Feynman Diagrams for Spectroscopy

High-energy physicists have long used specialized diagrams to represent complicated physical process and the relevant integral representations of those processes. Such a convention is also common in multidimensional spectroscopy, where there are many possible paths and phase matching conditions. Figure 1.2 shows one sample

ladder and Feynman diagram for a process involving a four wave interaction including populating the state $|a\rangle$. In figure 1.2a we have a ladder diagram showing a ground state $|0\rangle$ and two excited states $|a\rangle$ and $|b\rangle$. Each arrow represents a field interaction. Dashed arrows represent a bra interaction, resulting in a coherence in this case, and solid lines are a ket interaction, resulting in a population here. The Feynman diagram, in figure 1.2b emphasizes the density matrix elements at each time. Arrows pointed to the diagram represent absorptions and arrows pointed away are emissions. In both diagrams, the sinuated blue arrow is the detected signal. The time sequence for these diagrams in left to right in the ladder and bottom to top in the Feynman diagram. t_1, t_2, and t_3 are temporal separations of optical fields $\vec{E}_1$ and $\vec{E}_2$, $\vec{E}_2$ and $\vec{E}_3$, and $\vec{E}_3$ and $\vec{E}_{sig}$, as defined in figure 1.1. If we are to calculate the system evolution at each time, we must calculate $G(t)$, the greens function for time evolution, for the conditions shown at the respective times. Figure 1.3 expands on this to show Feynman diagrams for each of the third-order response terms (1.8a)-(1.8h).

1.2.2 Phase Matching Geometry

During an actual experiment many of the third-order signal pathways of figures 1.3 and 1.4 are present. However, only a limited number will be phase matched in any single direction. Consider the light fields $\vec{E}_1$, $\vec{E}_2$, $\vec{E}_3$ and $\vec{E}_{sig}$ having wavevectors $\vec{k}_1$, $\vec{k}_2$, $\vec{k}_3$, and $\vec{k}_{sig}$. We must have

$$\vec{k}_{sig} = \pm\vec{k}_1 \pm \vec{k}_2 \pm \vec{k}_3 \tag{1.9}$$

where we allow every combination of each term either positive or negative. In general, each $\vec{k}_n$ will have a unique direction, resulting in many possible $\vec{k}_{sig}$. The optical geometry chosen by the experimenter determine which $\vec{k}_{sig}$ will be measured, and which, if any, of $\vec{k}_1$, $\vec{k}_2$, and $\vec{k}_3$ are degenerate. For 2DIR, we first consider only

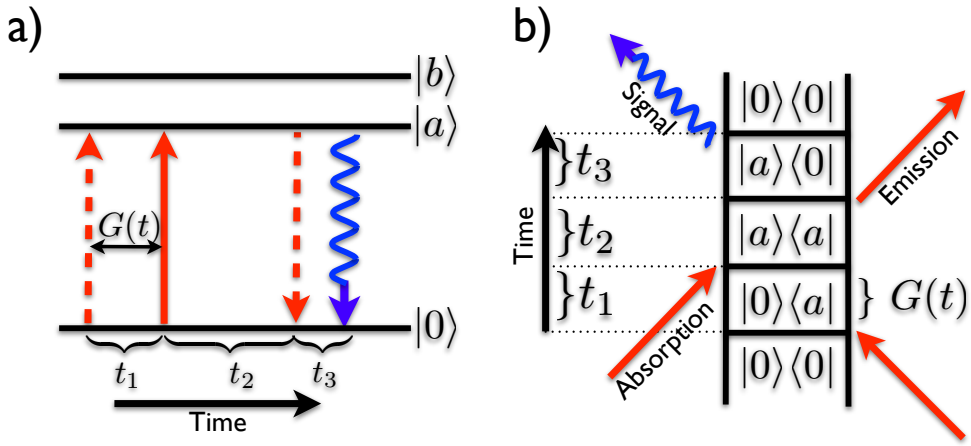

Figure 1.2: Sample ladder and Feynman diagrams for third order spectroscopy. In (a) we have a ladder diagram showing a ground state $|0\rangle$ and two excited states $|a\rangle$ and $|b\rangle$. Each arrow represents a field interaction. Dashed arrows represent bra interaction and solid lines result in a ket interaction The Feynman diagram (b) emphasizes the density matrix elements at each time. Arrows pointed to the diagram represent absorptions and arrows pointed away are emissions. In both diagrams, the blue arrow is the detected signal.

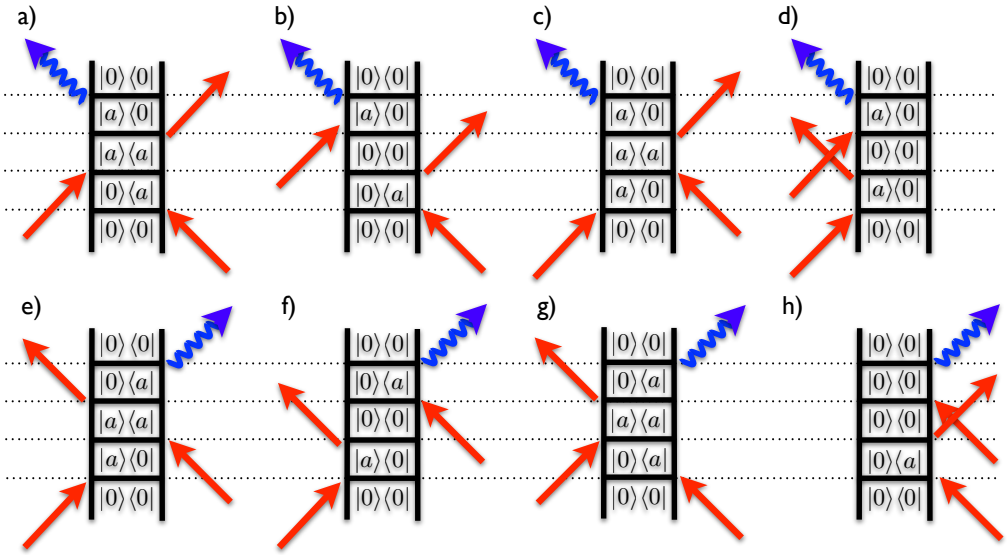

Figure 1.3: All Feynman diagrams for third-order spectroscopy. Only those diagrams that survive the rotating wave approximation are included. Diagrams (a)-(h) correspond to equation 1.8a-1.8h respectively

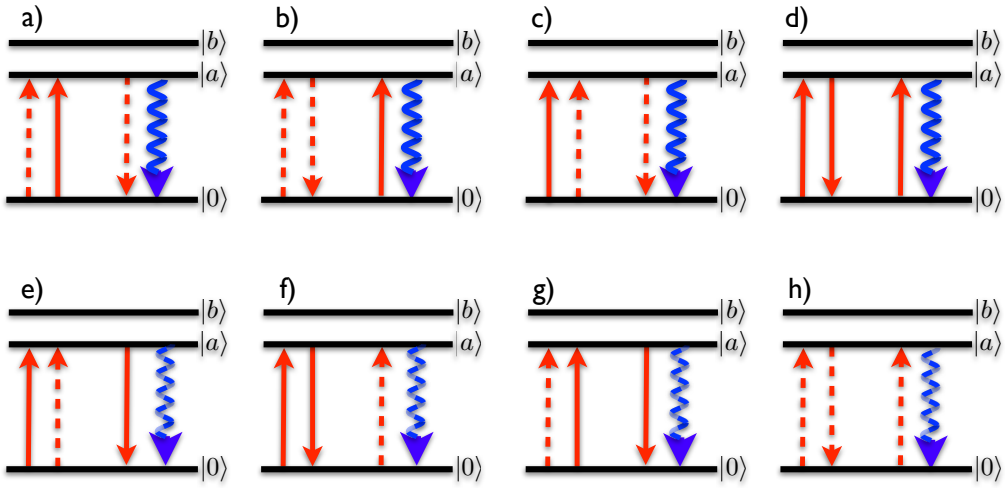

Figure 1.4: All Ladder diagrams for third-order spectroscopy. Only those diagrams that survive the rotating wave approximation are included. Diagrams (a)-(h) correspond to equation 1.8a-1.8h respectively

$\vec{k}_{sig} = \pm\vec{k}_1 \pm \vec{k}_2 + \vec{k}_3$. Next we consider all possible paths for the above listed paths. We can break the signal wavevectors into two useful groups, rephasing $\vec{k}_R$, and non-rephasing $\vec{k}_{NR}$

$$\vec{k}_R = -\vec{k}_1 + \vec{k}_2 + \vec{k}_3 \tag{1.10}$$

$$\vec{k}_{NR} = \vec{k}_2 - \vec{k}_1 + \vec{k}_3 \tag{1.11}$$

If we compare the signs of $\vec{k}_1$ and $\vec{k}_3$ for these pathways, we see that they are the same for non-rephasing and different for rephasing. The opposite sign in rephasing result in the opposite evolution of phases during t_1 and t_3. That results in the phases realigning for the measurement and, baring stochastic fluctuations, a large signal. The non-rephasing path has the same signs during both periods of coherent time evolution, so phases in slightly different environments continue to diverge.

In the three-beam geometry, three experimental beams are sent in at each of the three corners of a square to interact with the sample, as shown in figure 1.5a. The signal beam for this phase-matched geometry is propagating out from the sample

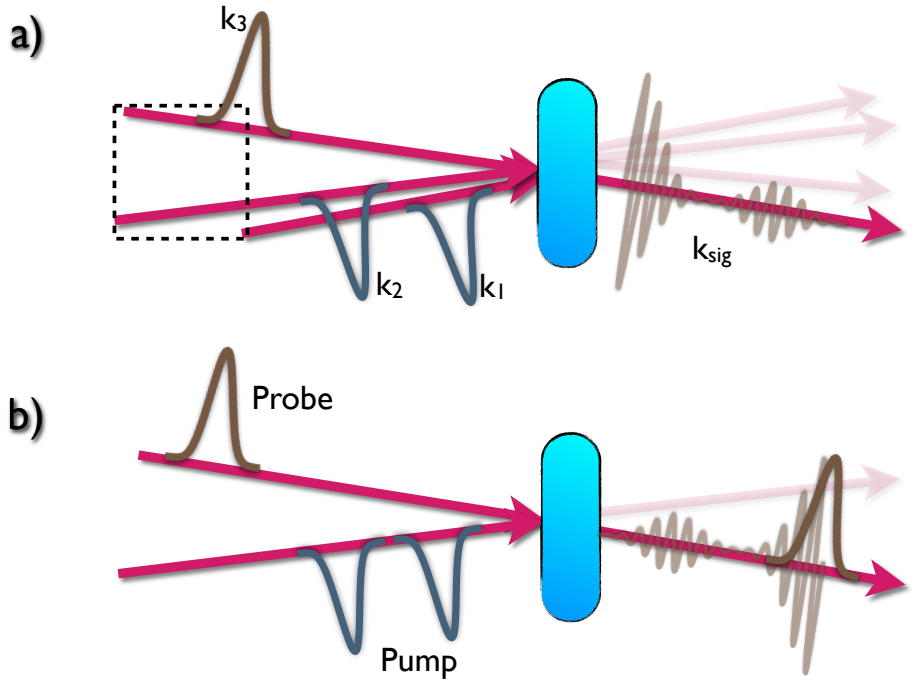

Figure 1.5: Geometry of three-beam and pump-probe experiments. (a) is the geometry of optical beams at the sample cell for square phase matching. (b) is the geometry of optical beams for pump-probe. In pump-probe 2D, each of the two pump pulses function as both $\vec{k}_1$ and $\vec{k}_2$

along the 4th corner of the square. The significant advantage of this is that the signal is produced in a background free direction. Additionally, for 2D spectroscopy the three-beam geometry has the advantage of easily separable rephasing and non-rephasing spectra which, with additional effort, can be combined to form an absorptive spectrum.[29;30] However, the experimental complications of overlapping multiple short-time-duration beams in a small sample volume with the proper geometry, is not negligible.

The pump-probe geometry, shown in figure 1.5b is slightly simpler. In this situation only 2 beams are required to overlap at the sample. This results from $\vec{k}_1$ and $\vec{k}_2$ being degenerate, which also makes $\vec{k}_3$ and $\vec{k}_{sig}$ degenerate. The disadvantage of this geometry, however, is that the signal co-propagates with the probe beam meaning that any signal has the probe as a background. Typically, this is overcome in most pump-probe spectroscopy experiments by chopping the pump beam on and off allowing for a comparison of probe spectra with the pump on and probe-only spectra. In the case of phase shaped experiments, however, the method of phase cycling minimizes the lost laser shots due to measuring of probe-only spectra, which contain no signal. This will be discussed further in section 2.1.1.1. The pump-probe geometry has the advantage of always acquiring absorptive spectra in 2D spectrometry. This results from the indistinguishability the of $\vec{k}_1$ and $\vec{k}_2$ in the 2D pulse sequence because of phase matching conditions. This can be an advantage or disadvantage depending on the needs of any particular experiment.

1.3 2D Spectroscopy

Multi-dimensional spectroscopy can overcome some of the limitations of linear spectroscopies.[31] Understanding line shape and position in MD spectroscopy gives information on the system environment and relaxation mechanisms,[21;32–39] as well as informing the study of molecular structure.[23;40–45] The application to understanding

molecular structure was recognized early, but quickly found to be very complicated. The 2D spectra obtained in early protein measurements demonstrated that much work must be done to fully understand the features in a 2DIR spectrum. 2D spectroscopy using NMR is well-established. The relatively simple Hamiltonian for nuclear resonances allows for straightforward interpretation of 2D NMR[46]. Moreover, the extremely narrow resonances of NMR result in a great seal of structural information that the overlapping modes of condensed-phase optical spectrum will often obscure. Unfortunately, the dynamical information that NMR can retrieve is limited due to NMR's relatively long time scales. 2DIR with isotope substitution was later shown to be effective in peptide structure determination[24], however, it has yet to be shown that this is has potential as a practical technique.

For most 2DIR experiments, three beams interact with a sample and one signal field is emitted, as diagramed in figure 1.1. This is a four wave nonlinear interaction and involves $\chi^{(3)}$[28]. The first pulse establishes a coherence in the system which the second pulse fixes to a population. The third pulse establishes a coherence that results in the emission of a signal.

We find that there are two relevant third-order response functions under the Condon and Gaussian approximations[47]:

$$R_{\pm}^{(3)} = \left\langle \exp\left[\pm i \int_0^{t_1} \omega(\tau) d\tau - i \int_{t_2+t_1}^{t_3+t_2+t_1} \omega(\tau) d\tau \right] \right\rangle .$$

where we take $\vec{E}_i$ to be a pulse of light at time t_i after the previous pulse with frequency ω_i, such as the three pulses figure 1.1a. Here, the opposite signs indicate rephasing and non-rephasing pathways. These differ in that the phase evolution in the rephasing pathway undo the phase evolution during t_1 producing an echo at $t_3 = t_1$. Taking a closer look at this, we recognize that the first integral involves the time between the first two pulses, when the system evolves in a coherence. Similarly the

second term, between the third pulse and detection, involves a second evolution of coherence.

The 2D spectrum is then retrieved by a Fourier transform.

$$\begin{aligned} R_{\pm}^{(3)}(t_2;\omega_1,\omega_3)) &= \int_0^{\infty}\int_0^{\infty} dt_1 dt_3 R_{\pm}^{(3)} e^{i(\omega_3 t_3 - \omega_1 t_1)} \\ R^{(3)}(t_2;\omega_1,\omega_3) &= \Re\left(R_{+}^{(3)}(t_3;\omega_1,\omega_3) + R_{-}^{(3)}(t_3;\omega_1,\omega_3)\right) \end{aligned}$$

The laser pulses used to perform these interactions are sufficiently spectrally broad to excite all the vibrational modes of interest. This may seem like it would cause a large amount of signal from paths that are not desired, but the phase matching condition selects for only the Liouville pathways that the experimenter wishes to probe. Moreover, the signal is normally detected in a background-free direction using a non-collinear geometry. Since typical time scales of response functions are very fast compared to methods for direct measurements electric field, interference-based 2DIR detection is used. That is either time or frequency domain interferometry between a reference local oscillator field and the emitted signal field.

The phase of the signal in the pump-probe geometry with both $\vec{k}_1 - \vec{k}_2 + \vec{k}_3$ and $-\vec{k}_1 + \vec{k}_2 + \vec{k}_3$ phase matched is

$$\begin{aligned} \phi_{sig} &= \pm(\phi_2 - \phi_2) + \phi_{probe} - \phi_{pump} \quad (1.12) \\ &= \pm(\phi_1 - \phi_2). \quad (1.13) \end{aligned}$$

The important point to take away form this is that the phase of the signal depends only on the relative phases between $\vec{k}_1$ and $\vec{k}_2$

A sample 2D spectrum is shown in figure 1.6. This spectrum is of dicarbonylacetylacetonato rhodium(I) (RDC) in hexane, a system with two narrow carbonyl absorptions. This was an early spectrum taken with the 2D spectrometer system

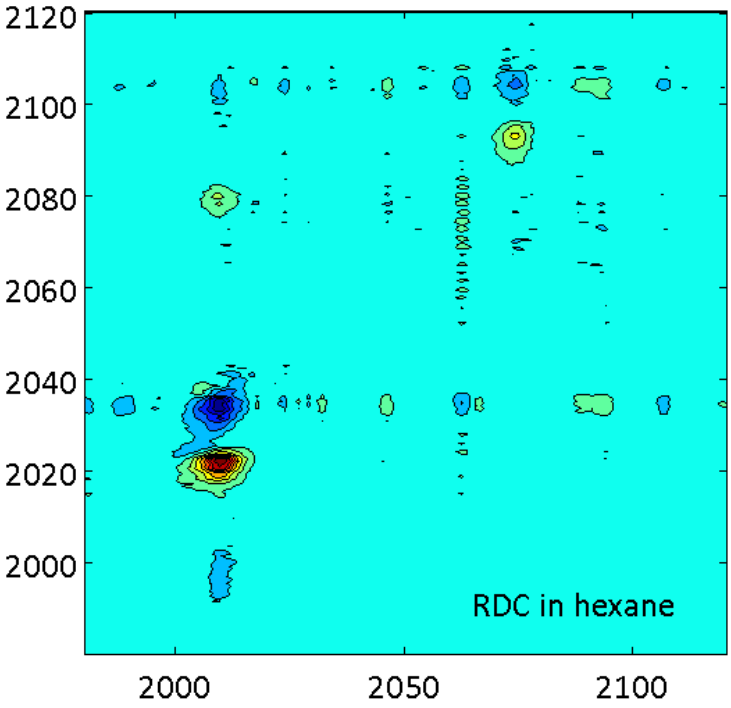

Figure 1.6: Sample 2DIR spectrum of RDC in hexane.

discussed in chapter II.

Measurements from 2D

2D spectra are rich in structural and dynamical information. As in the case of 1D spectrum, it is possible to look at several spectral properties to retrieve as much information as possible from a spectrum. Specifically, the peak location, sign, amplitude and shape all give information about the system. Moreover, as with the pump-probe spectrum, we can change the waiting time delay in a 2D sequence, t_2 in the sequence as show in figure 1.1. While many peak locations would be known from 1D experiments, the presence or relative strength of off-diagonal peaks gives information about couplings between the system's internal states and energy transfer in the system, which cannot be measured with a simple linear spectrum.

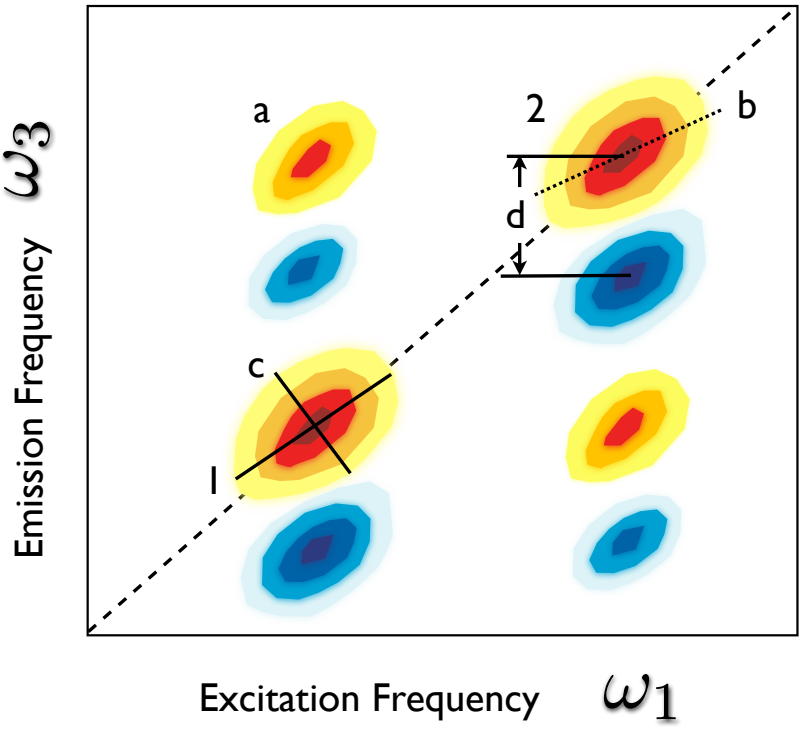

Figure 1.7: Cartoon of Typical 2DIR spectrum. Positive (red) and negative (blue) represent ground state bleaches and excited state absorption, respectively. (a) represents a cross-peak for peaks 1 and 2. (b) is the relative angle for peak 2. (c) shows measurements to get ellipticity (d) shows anharmonicity.

1.3.1 Peak Locations and Intensities

The 2D peak locations (where the ω_1 axis is the energy level of the excitation and the ω_3 axis represents the emission frequency) are relatively simple to interpret as the energy levels of vibrational states (Figure 1.7). Two-dimensional spectroscopy is capable of measuring peak locations. That is the energy associated with any given transition. Moreover, one can use strong peaks to enhance understanding of weaker peaks in two-dimensional spectroscopy. Naturally, peak amplitudes give relative strengths of absorption for on-diagonal peaks. The off-diagonal peaks give information on the couplings between vibrational levels (Figure 1.7a). Coupling strength is determined by the relative angles of system dipoles and IR pulse polarization. Recall that the third-order response had terms including $\mu^a_{l\nu}\mu^b_{\nu n}\mu^c_{nm}\mu^d_{ml}$ which reduces to $(\mu^1_{l\nu})^2(\mu^{sig}_{nm})^2$ in this case. 2DIR aids in understanding the geometrical structural of systems by measuring relative angles and distance, thus informing the structural knowledge of specific features.[24;48;49]

Information on states with weak transition dipole moments can be extracted by exploiting the fact that off-axis peaks have an intensity related to both transition dipole moments that they connect.[48;50]

Anharmonicity of a system is directly retrieved from 2DIR, since the sign of a peak in 2DIR can indicate the number of quanta in the transition and 2D spectra generally allow for better separation of nearby spectral features. For example, the typical one-quantum states may be set to be negative and relates to those paths that only involve the first excited state of a system. We call these a ground state bleach (GSB). These are called excited state absorptions (ESA) and are typically set to be positive peaks. These would indicate a two-quantum state of the system probed having been on the first excited state when the probe arrives and then we measure absorption from this excited state to a higher excited state. The anharmonicity is given by the offset between one- and two-quantum transition peaks (Figure 1.7d.)

Lineshapes are more informative in 2D spectra compared with linear spectra.[29] 2D, or higher multi-dimensional spectra, allow for separately resolving homogeneous and inhomogeneous line shapes and tracking the timescales by which the relevant transitions sample all of the available states.

1.3.2 Chemical Exchange

One useful measurement from 2D is chemical exchange measurements by monitoring cross peak growth. The basic idea is illustrated in figure 1.8. In figure 1.8a, a $t_2 = 0$ ps waiting time spectrum is shown given a system with two distinct peaks. Each of the two peaks, blue and green, have some population of molecules as indicated in the top of figure 1.8a. With d$t_2 = 0$ ps, there is no time for species to enter interconvert. Figure 1.8b shows the ladder diagram of the energy levels in the system. If, by some means, during the waiting time of the experiment individual molecules interconvert between energy levels, there will be some off diagonal population as indicated in figure 1.8c. Consider the lower right yellow peak. This indicates a molecule that was excited at the higher frequency mode but later detected at the lower frequency mode. Similarly, the upper left peak is excitation of the lower frequency mode an detection at the higher frequency mode. If we waited a longer key to waiting time, we may be in the situation illustrated in figure 1.8d in which more molecules have interconverted, making larger off axis peak intensities.

The first use of 2DIR with this interpretation was by Woutersen *et. al.* in a study of Hydrogen-bond formation and breaking in N-methylacetamide.[51] Since then there have been many other studies of chemical processes measured by this technique such as complex formation with a solute,[21], hydrogen bond formation[52;53] and migration,[54;55] rotation about a bond,[56] and isomerization in metal carbonyls.[37;57;58]

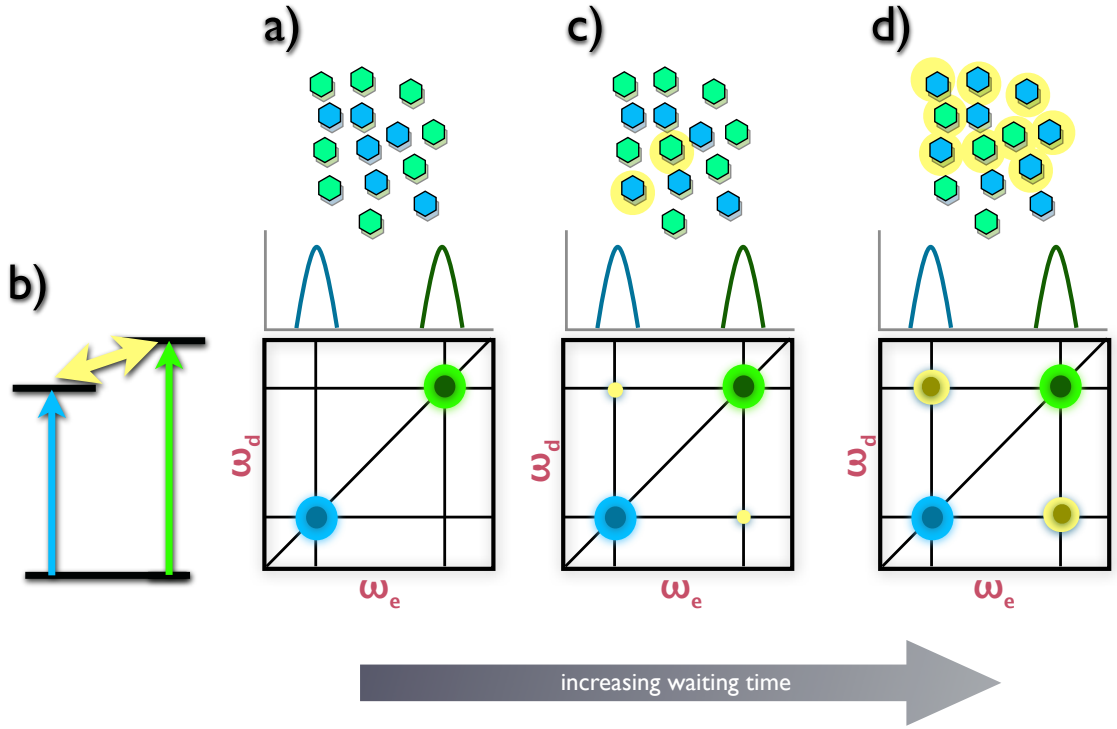

Figure 1.8: Cartoon of chemical exchange measured by 2D spectroscopy.

1.3.3 Spectral Diffusion

In a system undergoing continuous fluctuations, we may expect a continually changing potential field that any given system mode experiences. As a variable potential field will result in a variable frequency for any given transition, we can observe these fluctuations to get a timescale for this sampling of accessible potential energy configurations. We measure the correlation between the initial frequency and the frequency at later times. This is called the Frequency-Frequency Correlation Function (FFCF). In the field of multidimensional spectroscopy this is referred to as the spectral diffusion.[59–65] The basic measurement is taken by observing the shape of individual peaks in the 2D spectrum as they evolve with increased t_2 waiting time. To make this quantitative, the ellipticity of the peak, the slope of the center line, or ratios of rephasing and non-rephasing spectra are taken.

In general a correlation function is used to determine how closely any two functions or values relate. Often this is done as a function of time, but can also be done in other coordinates. In the case of the FFCF, we look to relate how the fluctuations of frequency about the nominal average transition frequency correlate as a function of time. We relate the initial value of this fluctuation, $\delta\omega(0)$ to the fluctuation at a later time, $\delta\omega(t)$, in

$$C_{FF}(t) = \langle \delta\omega(0)\delta\omega(t) \rangle \tag{1.14}$$

$$= \int_0^t \delta\omega(t)\delta\omega(t+\tau)d\tau \tag{1.15}$$

Figure 1.9 is a cartoon of this. In 1.9a we have a fluctuation $\delta\omega(t)$ which quickly devolves into random noise. Since the value at any given time does not accurately predict the value at the times around it, there is a very short temporal correlation and the FFCF has a fast decay, as shown in figure 1.9b. In 1.9c, we have a different $\delta\omega(t)$, which has more longer term correlations. at any given time, the value relates

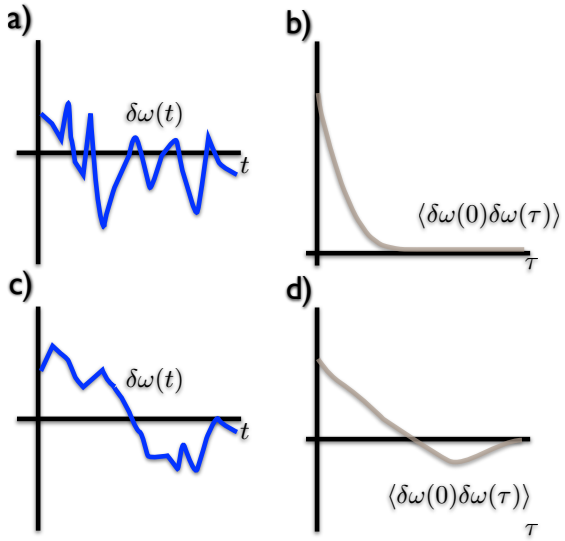

Figure 1.9: Cartoon of the FFCF function.

reasonably well to the values at other nearby points, this results in a longer-term correlation function and slower decay, as shown in 1.9d. Figure 1.9d also has a negative component, which is possible. In 1.9c, the points in the early time are opposite in sign compared to those at later times with similar values, causing a negative component to the FFCF. While this is not often seen in dissipative systems, such as a molecular vibration in solution, is possible. As an aside, we choose the frequency to be a fluctuating frequency about a central value and the full frequency would cause a large offset and $C_{FF}(t)$ would never go to zero.

An additional method to extract related information is to extend the 2D measurement to three-dimensional spectroscopy.[62] In most cases, the line shape is correlated to solute-solvent dynamics, and the main considerations have been characteristic angles (Figure 1.7b) and ellipticity (Figure 1.7c.) For example, a long thin ellipse parallel to the diagonal indicates inhomogeneous broadening, whereas a more round shape indicates homogeneous broadening.

More complicated line shapes have been considered also.[2;66] Complex peak shape analysis generally requires some physical intuition as to how there may be a rela-

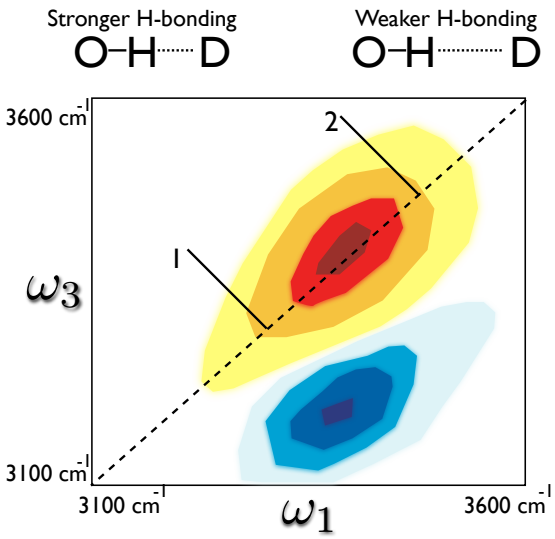

Figure 1.10: Cartoon of 2D-IR from hydrogen bonding in water. Based on data from Loparo *et. al.*,[2] positive (red) and negative (blue) peaks represent $0 \rightarrow 1$ and $1 \rightarrow 2$ transitions, respectively. Lines 1 and 2 represent members of the ensemble with different local environment. Measurable differences in half-width indicate qualitatively different relaxation times due to differing hydrogen bonding strengths.

tionship between the inhomogeneous broadening and how it relates to the possible fluctuations in frequency. In the work of Loparo *et. al.*,[2] for example, a wedge shaped peak is found for the OH stretch in HOD:D_2O (Figure 1.10.) The interpretation of the wedge shape is related to the strength of hydrogen bonding as a function of the mean length of the hydrogen bond.[2] As the hydrogen bond is excited by higher frequencies (Figure 1.10 line 2), the average hydrogen bond distance is longer than those excited at lower frequencies (Figure 1.10 line 1). The interaction between the oxygen and hydrogen is weaker with the longer bond distance, allowing fluctuations due to other molecules a larger role. Increased solvent interaction then leads to a line shape broader for these higher frequencies.

Previous studies of the FFCF in metal carbonyl systems has revealed a novel understanding of the interaction between solute and solvent, including a test of Kramer's theory.[38]

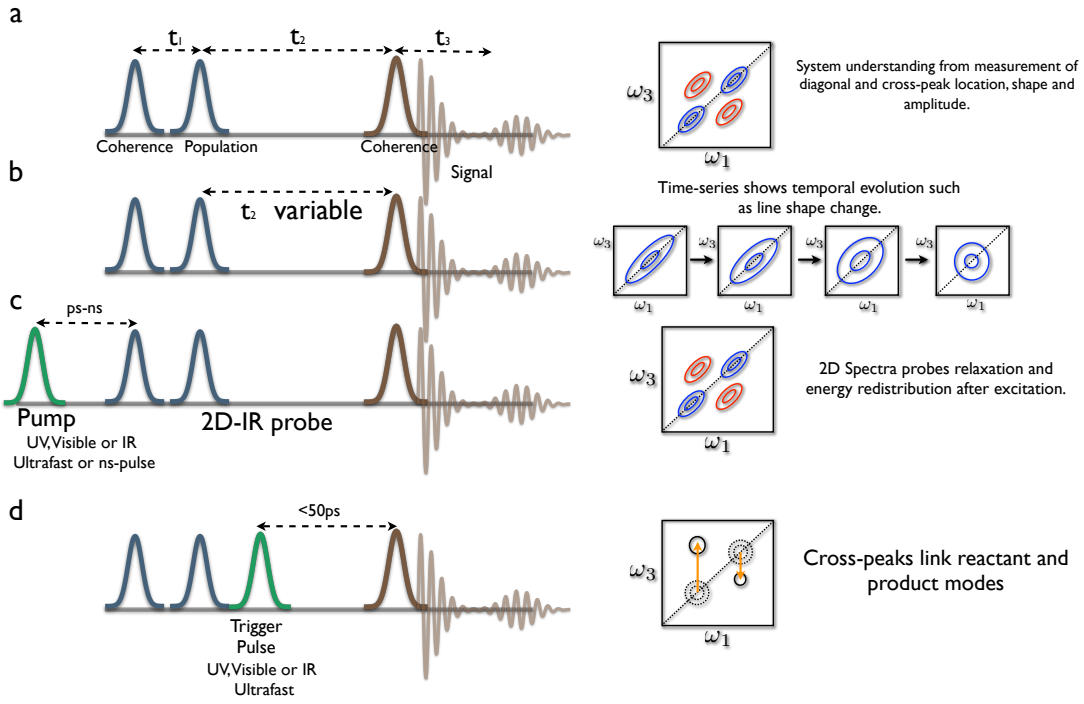

Figure 1.11: Several 2DIR experiments are possible. (a) The most common pulse train in Fourier Transform 2DIR (b) As above, but t_2 is varied and the resulting series of 2D spectra give dynamics of the system, such as relaxation. (c) Pump-Probe: The system in placed in a non-equilibrium state by a pump pulse and 2D spectra are taken, at a later time, probing the system. (d) Triggered Exchange: A pulse during t_2 manipulates the system and the final pulses allow measurement of the trigger's effect.

1.3.4 Non-equilibrium Spectroscopy

Figure 1.11b-d includes other types of 2DIR experiments. 1.11b is effectively the same experiment where t_2 is variable such that the line shapes, and other parameters, can be watched as the system relaxes from the first two excitation pulses. This is most useful in understanding the system-solution dynamics or energy re-distribution in the system.

A second class of 2DIR experiment is non-equilibrium experiments (Figure 1.11c,d). As opposed to the equilibrium experiments discussed in the last section, these

experiments involve a system intentionally out of equilibrium. In one variant (pump-2D-probe) a pump pulse excites the system followed by a 2D measurement (Figure 1.11c.) Pump-2D-probe studies the state of the system after the pulse is applied and would yield dynamical information on the relaxation to equilibrium, for example.[67] This experiment is mostly sensitive to the relaxation and vibrational states after the new, post-interaction state is established. This experiment is useful in studying the conformational change of a protein after interaction with an optical pulse that induces an electronic excitation, for example. In a second approach, triggered exchange, the pump pulse excites the system after the first two IR pulses, but before the final IR pulse and signal emission (Figure 1.11d.) Triggered exchange measures the changes in the system from initial to final states. Specifically, we are able to map initial vibrational states to final vibrational states, and study how energy leaves the system or is redistributed. Transient absorption experiments are also capable of quantifying energy transfer, but without as much detail as 2DIR can retrieve.

1.4 Pulse Shaping

The AOM pulse shaper operates using acoustic Bragg scattering. This name comes from the same condition as X-ray scattering off a regular atomic crystal. The regular "lattice" of acousto-optic scattering is the peaks and troughs of a longitudinal sound wave in the acoustooptic crystal. Following the prevention of acoustooptics presented in Boyd[28], let us first define the incoming optical wave as incident with some wave vector $\vec{k}_{in}$ and frequency ω_{in}

$$\vec{E}_{in} = A_{in} e^{i(\vec{k}_{in}\cdot\vec{r}-\omega_{in}t)} + c.c., \tag{1.16}$$

where the complex conjugate is often omitted and assumed present to get a real valued wave.

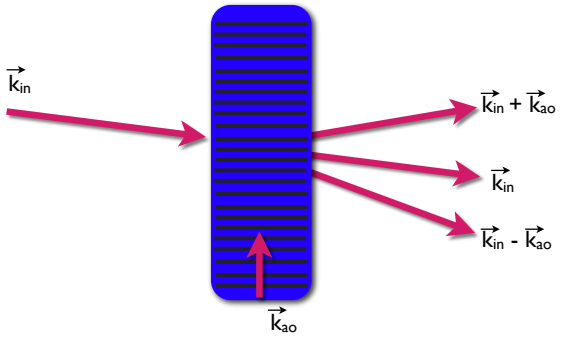

Figure 1.12: Perpendicular geometry acoustooptic deflection.

The wavelength of the acoustic wave, Λ_{ao}, is set to be

$$\Lambda_{ao} = \frac{2\pi v}{\Omega_{ao}}, \tag{1.17}$$

such that scattering is according to the Bragg-condition

$$\lambda = 2\Lambda \sin\theta, \tag{1.18}$$

where v is the speed of sound in the crystal and λ is the optical wavelength in the crystal. We then can consider the wavevectors

$$\vec{k}_{sh} = \vec{k}_{in} \pm \vec{k}_{ao} \tag{1.19}$$

for deflection in the ± 1 order as shown in Figure 1.12. Note that this not only means that the direction is changed, but also the frequency, $\omega_{sh} = \omega_{in} \pm \Omega_{ao}$. This may be a concern in some cases, but here, not only is the input optical pulse tunable over a large range, but the acoustic frequency, 80 MHz, is orders of magnitude smaller than the optical frequency, 60 THz, thus any shift is imperceptible.

A more detailed description of the acoustooptic deflection requires consideration of the changes in the dielectric constant as a result of the longitudinal acoustic pressure

wave. This is described in the isotropic case by γ_e, the electrostrictive constant, and in general as the strain-optic tensor, $\hat{P} = p_{ijkl}$. Consider the a small change in the inverse dielectric tensor as described by a small strain,

$$\Delta(\epsilon^{-1})_{ij} = \frac{1}{2}\sum_{kl} p_{ijkl}\left(\frac{\partial(\delta x)_k}{\partial x_l} + \frac{\partial(\delta x)_l}{\partial x_k}\right), \tag{1.20}$$

where $(\delta x)_n$ is the displacement of a particle in the nth direction and p_{ijkl} are components of the strain-optic tensor.[28] We can the define small changes in the material dielectric tensor as

$$(\Delta\epsilon)_{ij} = -\sum_{jk} \epsilon_{ij}\left[\Delta(\epsilon^{-1})\right]\epsilon_{kl}. \tag{1.21}$$

Since these changes are the result of a the wave field propagating in the crystal, we can use similar notation to equation (1.16) for the acoustic wave.

$$\vec{E}_{ao} = A_{ao}e^{i(\vec{k}_{ao}\cdot\vec{r}-\Omega_{ao}t)} + c.c., \tag{1.22}$$

where the use of $\vec{E}$ is not meant to imply this is an electric wave. Combining this with some small dielectric change as indicated by the tensor elements of equation (1.20),

$$\Delta\epsilon = (\Delta\epsilon)_{ij}e^{i(\vec{k}\cdot\vec{r}-\Omega_{ao}t} + c.c. \tag{1.23}$$

The tensor element from equation (1.21) reduces to $\Delta\epsilon = \gamma_e\delta\rho/\rho$ in the isotropic case. The periodic dielectric variations diffract the incoming $\vec{E}_{in}$ to the diffracted, and shaped, $\vec{E}_{sh}$

As with all electric fields propagating through a medium, the total electric field

$\vec{E} = \vec{E}_{in} + \vec{E}_{sh}$ must satisfy Maxwell's equation in a medium,

$$\nabla^2 \vec{E} - \frac{n^2 + \Delta\epsilon}{c^2} \frac{\partial^{2\vec{E}}}{\partial t^2} = 0. \tag{1.24}$$

By using the form of the electric fields given in (1.16), we can use this to derive a set of coupled equations for the transfer of amplitude to the shaped beam assuming travel in the $\hat{z}$ direction perpendicular to the acoustic wave.

$$\frac{dA_{in}}{d_z} = i\kappa A_{sh} e^{-i\Delta k z} \tag{1.25a}$$

$$\frac{dA_{sh}}{d_z} = i\kappa^* A_{in} e^{i\Delta k z} \tag{1.25b}$$

where we have introduced a constant

$$\kappa = \frac{\omega^2 \Delta\epsilon^*}{2k_z c^2}. \tag{1.26}$$

It should be clear that when the mismatch, Δk from the prefect Bragg condition is zero,n the transfer of amplitude is maximal. in our system this will be further refined by adding a spatial variation of the acoustic wave which will result in a spatial variation in $\Delta\epsilon^*$. As our shaper will map optical frequencies to location on our AOM crystal, we can use this to change the amplitude at different frequencies. We should also note that equations (1.25a) and (1.25b) assume that there is a long path length for optical - acoustic interactions, which is the case in our acoustooptic crystal.

Naturally, if we spatially separate different beams, or portions of beams we can apply different acoustooptic defecting fields. Of interest to ultrafast optics and femtochemistry studies is the application of phase and amplitude modifications as a function of optical wavelength, or by the Fourier transform, time. This is accomplished in an 4-f shaper geometry, first described by Froehly *et. al.*[8] for picosecond pulses, and later used in many variations.[10] The basic premise of this system is to

use a dispersive element, such as a grating or prism, to disperse light in a spacial dimension. Then a focusing element, such as a lens or curved mirror, is placed at one focal length away to collimate the dispersed light. A further focal length away is the shaping element. Finally, the process is reversed so that the spatially-dispersed frequencies are reformed into a beam. The details of the shaping process and the possible pulse shapes will be discussed in chapter II.

1.4.1 2D by Pulse Shaping

As discussed in section 1.3 2D experiments require three laser interactions in a specific timed order. In the case of 2D pulse sequences by shaping both $\vec{k}_1$ and $\vec{k}_2$ are copropagating after being generated from a single pulse sent into a pulse shaping setup. Thus the main requirement in shaping for 2D experiments is to take a single laser pulse and separate it into a pair of pulses with a known and variable delay. The details of this process will be discussed in chapter II.

As the $\vec{k}_1$ and $\vec{k}_2$ wavevectors in the 2D pulse sequence are in the same direction after leaving the pulse shaper, we only have one beam where we would have had two in the three-beam geometry. As a result, the experiment is done in the pump-probe geometry, as shown previously in figure 1.5b. This has the advantage of producing absorptive spectrum without additional effort and can be implemented with fewer optics.

1.4.2 Further Pulse Shaping Methods

With the pulse shaping system to be described in chapter II, we are able to produce more varieties of pulse sequences than the pulse pairs required for two-dimensional spectroscopy. Many other experimental methods currently used in the visible and near IR could be implemented in the mid-infrared and new methods are also possible. In the next few sections, I describe a few experiments a mid-IR shaper allows and what

purpose they could serve in chemical or optical measurements. To my knowledge these experiments have not been fully implemented in the mid-infrared.

1.4.2.1 Coherent Control

Coherent control of chemical species has long been a goal in photochemistry.[14] In this experiment, a sample is pumped with a shaped pulse and later probed at a later time. The experimenter systematically modifies the shaped pulse to promote the desired experimental outcome, or suppress unwanted outcomes. Most coherent control studies have involved the control of electronic excitations in the target species. However, in many physical models the nuclear positions in a molecule leads naturally to reaction coordinates. This would indicate that coherent control of a reaction would be more effective using vibrational excitations as opposed to electronic excitations, which only indirectly affect nuclear positions. In order to take advantage of the more direct connection between structure and vibrational modes, we will focus on vibrationally controlled chemical processes.

The coherent control experiments have significant potential, but results are often difficult to interpret on a molecular level. By using powerful multidimensional spectroscopic probes, one could better understand the interaction of a shaped pulse with a sample, thus improving the interpretation of the effect of the control pulse. By applying the shaped pulse in a triggered exchange experiment (Figure 1.11d) and observing the 2D spectrum, we can understand how the energy levels before and after are connected which may provide insight into the specific mechanism of the interaction. Even if a pulse is found not to control as well as expected, the 2DIR spectrum will still provide information about the interaction and may offer clues explaining the failure to control the system. For example, if a stimulated vibrational state is too short-lived to effect control, we will still be able to observe the mechanism of relaxation.

Previous experiments in mid-IR coherent control have shown promise when using pulse shapes motivated by knowledge of the system, but these experiments were limited by relatively crude pulse shaping methods. Some projects attempted to step up the energy levels of a CO-stretch mode in metal carbonyl[68;69] and protein[70] systems. The idea behind these experiments was that the anharmonicity of the vibrational potential would more favorably absorb lower frequency IR if the vibration was already in a higher state (See Figure 1.13). By chirping the pulse so that the later light has lower frequency, the conversion to higher levels was found to be enhanced. In the metal carbonyl case, dissociation of the carbonyl group as a result of climbing the CO-stretch energy levels was successful, illustrating control of one bond by excitation of another.[69] This was not, however, effective in the protein case.[70] The vibrational relaxation in the hemoglobin system is believed to be primarily to the heme-group with little energy transfer to Fe-C mode. Consequently, exciting the CO stretch had little effect on the Fe-C bond. These studies relied on creating a chirped pulse by simple propagation through material with normal or anomalous dispersion. Full phase and amplitude shaping, as our system allows, could provide the ability to find optimal control pulses where the experiments above were only able to show if a few pulses were better or worse with respect to each other.

1.4.2.2 Quantum Process Tomography

With increasing interest in information processing by quantum system, there is increasing interest in methods to interrogate the quantum processes to understand the states and dynamics of quantum systems. Moreover, the potential role quantum coherences could play in biological systems, with some claiming systems show electronic coherences,[6;71] while other systems show only vibrational effects is an important motivation for new tests of quantum systems.[16] Many potential methods have been proposed and some demonstrated.[17;18;72] The basic motivation, from the perspective

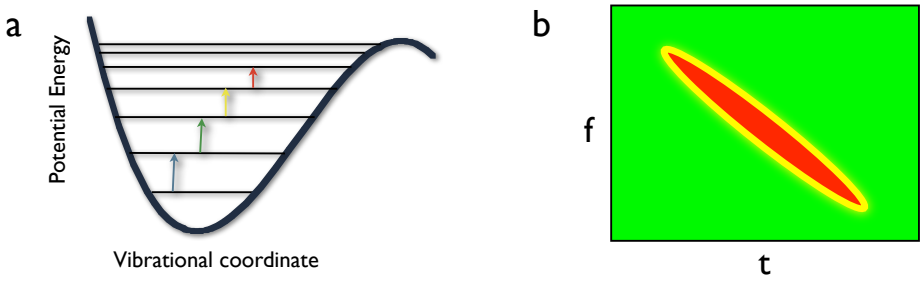

Figure 1.13: Coherent control of vibrational excitations. (a) As excitations approach bond dissociation the levels get closer together and (b) the general form of a Wigner plot that would promote stepping up such energy levels. That is higher frequencies at earlier times and lower frequencies at later times. (c) metal carbonyl (d) hemoglobin systems that have been studied with these types of chirped pulses

of quantum information, is to be able to retrieve as much information as possible about a system Hamlitonian so that the states or their evolution can be known and characterized. If a quantum computer is to be practical we must have ways of reading the state of the system, and methods for verification of quantum processes, such as Shor's algorithm,[73] Grovers search algorithm,[74] or any other proposed quantum algorithms.[75]

Multidimensional spectroscopy is one method we can learn about the states and dynamics of a system. For example, Golonzka, *et. al.*[76] were able to retrieve all relevant parameters of $\chi^{(3)}$ for the local carbonyl mode Hamlitonian of RDC by 2DIR spectroscopy with multiple polarizations. Quantum process tomography (QPT) is an additional class of experiments that could be implemented to map quantum processes. The basic idea behind QPT is to form a linearly independent basis of input states and then allow the system to evolve, after which the system is probed to understand the final states. Thus enabling a mapping of input to output states.

Through the use of amplitude shaping, a pump-probe experiment can be designed with the pump modified to preferentially excite states the researcher wants to initialize and preform a quantum process with. After the initial quantum state is prepared by

the pump, the system is allowed to evolve and then measured by the probe. In the chemical systems considered in our lab the quantum process we would measure is decoherence, coherence transfer, population transfer and population decay of a quantum system (solute) interacting with a bath (solvent).

The shaping software to run such an experiment has been written, but a full data set has not been taken.

1.5 Thesis Outline

The following chapters take the general discussion of 2D spectroscopy above and discuss a new optical system for the measurement of 2D spectra (Chapter II), the use of ultrafast chemical exchange spectroscopy and spectral diffusion to measure fast fluxtionality in iron pentacarbonyl, (Chapter III), and the used of 2DIR to understand dynamics and electrostatics of a model protein active site (Chapter IV.)

CHAPTER II

Acoustooptic Pulse Shaping in the Mid-Infrared

The acquisition of multidimensional spectra is not trivial. Starting from a commercial amplified Ti:Sapphire laser, our main 2D spectrometer system utilizes five nonlinear stages utilizing six non-linear crystals in addition to the actual sample interaction. Controlling this requires dozens of mirrors and a dozen time delay stages. This system, while compact by laser lab standards, fills most of a laser table and can take some time to align and optimize.

If multidimensional spectroscopy is to move from a niche experiment in advanced ultrafast optics labs to a mainstream technique like FTIR or multidimensional NMR, there is need to simplify the user experience. The development of a pulse-shaping based 2D spectrometer is one step toads this simplification by limiting the complexity of the optical path and reducing moving parts, which are more prone to malfunction. This system has other benefits as well. The NMR community is full of complicated pulse sequences for different experiments and optimization of signal levels. While the RF pulse sequences of NMR are easily produced in electronics, optical pulses and optical pulse sequences have much less developed methods for their production. Nonetheless, optical pulses can be modified, or shaped, through the use of pulse shaping optical components.

Pulse shaping in the mid-infrared is a new technique pioneered by the Zanni

group at the University of Wisconsin-Madison.[11–13;77] The development of a mid-infrared pulse shaping system at the University of Michigan progressed in several stages, including the development of a mid-infrared laser source, an acoustooptic pulse shaper, supporting electronics and software, and an optical setup for sample interaction followed by signal upconversion and detection. These systems will be covered in the following sections. Before discussing the details of the system, I will briefly discuss what is meant by pulse shaping, as well as the theoretical background of pulse shaping in optical frequencies.

2.1 Pulse Shaping

When discussing optical pulses it is first necessary to understand what is meant by an optical pulse. In general, we can describe a pulse by a time-domain function

$$\vec{E}_{in}(t) \;=\; real\left(e^{i\vec{k}t+i\phi(t)}\right), \tag{2.1}$$

where the *real* is often omitted and assumed.

In the case of optical pulses, we can further subdivide this function into a carrier wave $e^{i\omega_0 t}$ and an amplitude $A(t)$. The amplitude, $A(t)$, is assumed to be within the slowly varying envelope approximation. This approximation applies when the amplitude envelope does not vary significantly during a single optical period. Mathematically,

$$\left|\frac{\partial}{\partial t}A(t)\right| << \left|\frac{\partial}{\partial t}e^{i\omega_0 t}\right| \;\leq\; |\omega_0| \tag{2.2}$$

For our mid-infrared optical pulses near 5 μm wavelength, with approximately 12 fs periods, this inequality is easily satisfied due to our relatively long 150+ fs pulses. The carrier frequency is taken as the center frequency of the light pulse.

The grating in a 4-f shaper effectively takes the Fourier transform of the time-domain pulse and spreads the frequencies spatially. As these frequencies are now dispersed in space we can map position on our AOM to optical frequencies and produce a masking field $\vec{E}_{ao}(\omega_{opt} \propto t_{RF})$.

The diffraction of the acoustooptic modulator act to multiply terms

$$\vec{E}_{in}(\omega) \cdot \vec{E}_{ao}(\omega) \quad = \quad A_{in}(\omega) e^{i\vec{k}t} A_{ao}(\omega) e^{i\phi_{ao}(\omega)} \tag{2.3}$$

From the we see we get a new pulse amplitude $A_{in}(\omega) \cdot A_{ao}(\omega)$. It should be reasonable that the output pulse spectrum should both depend on the input (A_{in}) and the diffraction amplitude (A_{ao}). The phase also adds so that $\phi_{ao}(\omega)$ is added to the input pulse phase, allowing for phase control.

Considering the experiment as a pump-probe experiment (with a spectrally resolved probe), we have effectively arbitrary (1k-4k levels) of amplitude control at $\approx$800 points across the spectrum. Shot noise, carrier frequency generation, and beam diameters limit this to an effective control closer to 100 amplitude levels at each of 100 frequency bins.

Phase Control

The capability of adding arbitrary phases to optical pulses is of paramount importance to measuring a 2D spectrum because we require control of pulse phase to select both the sign and Feynman path for any given contribution to the 2D spectrum. Equation (1.13) gave us that the phase of the measured signal in a 2D pulse sequence is only dependent on the relative phases of the $\vec{k}_1$ and $\vec{k}_2$ pulses. Since these pulse are both produced by the shaper it is vital that we are able to control the retaliative phases of the pulses produced in the shaper. The details of this process

will be discussed in section 2.1.1.

In our optical setup, the phase control is primarily limited by the electronics producing the RF signal fed into the acoustic transducers. As the carrier RF period is 12.5 ns and our arbitrary waveform generator can only update every 3.5 ns, we are somewhat limited in how well we can set an arbitrary combination of phase and amplitude. An arbitrary waveform generator with higher frequency output would improve this. Another consideration for phase stability is trigger timing and stability of the electronics associated with the AOM system. Any jitter in the triggering system, or the arbitrary waveform generator system clock, will result in phase jitter between the shaped and unshaped optical pulses. This is not a concern for phase within the shaped pulse, only between shaped and unshaped pulses. A timing jitter as low as a few hundred picoseconds can easily be detected in the interference between pump and probe in our 2D measurement. To minimize this effect a field programmable gate array (FPGA), which is a programmable logic circuit, was programmed to synchronize the arbitrary waveform generator clock with the Ti:Sapphire laser oscillator. This provides a digital clock source which is vary stable and is locked to the laser pulse train, the ultimate source of all our optical beams.

Amplitude Control

For many pulse shaping systems amplitude control as a function of frequency is the simplest form of shaping. Amplitude shaping could be as easy as a razor blade that blocks half of the pulse producing a narrower frequency bandwidth. In our system, amplitude shaping is used for calibration and is utilized in the implemented Quantum Process Tomography pulse sequence where pump-probe experiments are preformed with variable levels of excitation for each mode. Other uses in 2DIR could include corrections to pulse amplitudes as a function of frequency, or to correct for variable diffraction efficiency across the pulse as the germanium crystal absorbs some of the

RF signal. An example of amplitude shaping will be given in section 2.6.

2.1.1 Shaping for 2D

The basic pulse sequences required for 2D spectroscopy were shown in figure 1.1, chapter I. In order to step the t_1 separation of pulses E_1 and E_2, the waveform generator must provide to the AOM crystal unique waveforms

$$M(\omega) = e^{i(-\omega t_1 + b_0 + b_2(\omega-\omega_0)^2 + M_\omega(\omega))} \tag{2.4}$$

$$* M_A(\omega), \tag{2.5}$$

where $-\omega t_1$ is a time translation of the first pulse a time t_1 in front of the second pulse. b_0 is an adjustable phase offset, b_2 adds quadratic phase (linear frequency chirp), and $M_\omega(\omega)$ is an additive phase for each point. $M_A(\omega)$ is a multiplicative amplitude for each of the ≈800 points in the electronic signal. This can be used to limit the pulse bandwidth, correct for reduced efficiency with acoustic absorption, or for additional amplitude shaping. In a typical experiment, we wish to measure chemical vibrations that are approximately 16 fs in period. For optimal spectral resolution using this system, we need to scan out up to 6 to 9 ps t_1 delay. Since our vibration will oscillate at this 16 fs period, we need to sample every 8 fs, or faster, to measure the sinusoidal signal. The highest frequency that one can reliably measure with with a sampling frequency f_S is $\frac{1}{2}f_S$, this is called the Nyquist rate limit. In order to sample more often than the Nyquist rate limit, we require several thousand unique t_1 times for a given 2D spectrum. Moreover, phase cycling which will be discussed later, requires approximately 4 times as many waveforms. Additional considerations affecting the number of unique waveforms required is measurement in a rotating frame, which will be discussed later.

2.1.1.1 Phase Cycling

Pulse shape two-dimensional experiments are performed in the pump-probe geometry rather than the traditional three-beam square geometry. The pump-probe geometry results in the signal being homodyned[1] with probe pulse. As in normal pump-probe experiments, one might expect that we must chop the pump beam and take differences of pump on and pump off spectra to obtain our signal. However, the nature of the 3rd order response signal of equation (1.8a)-(1.8h) offers an alternate method. Notice that the signal does not depend on the absolute phases ϕ_1 and ϕ_2, but the difference between ϕ_1 and ϕ_2,

$$\Delta\phi = \phi_1 - \phi_2. \tag{2.6}$$

AOM pulse shaping has the advantage of adding arbitrary phase to the entire pulse or portions thereof. Thus, if we manipulate the phases we can change the sign of the signal for different experimental conditions. If, for example, we know in advance that we are going to take spectra with and without pump pulses, as is customary in the pump-probe geometry, we can optimize our signal levels. Instead of totally blocking the pump pulse, we can add a *pi* offset to the phase of one pump pulse. Then the signal will have the opposite sign so that when we subtract two subsequent spectra, the portion that is the signal will add. This effectively increases our signal to noise by a factor of two without increasing the experimental time.

One common problem of pump-probe spectroscopy is scattering of the pump beam into the path of the probe beam. This results in interference pattern dependent on the time delay. Just as we enhanced the signal in the pump-probe subtraction, we

[1]Homodyned, as used in most of ultrafast optics, refers to the mixing of an optical signal with the same optical beam that produced that signal. This is much more restrictive than the more prevalent electronics usage of the term for signals mixed with the same source. The use of term Heterodyne is also different in that in most ultrafast optical systems a heterodyned detection is mixing of signals with the same oscillator originating both light beams. In electronics this term would be used for mixing of signals from completely separate sources.

can modulate the phase of the pump beam using the AOM shaper in such a way as to reduce, or completely eliminate, the interference from scattering. The scattering signal depends on the absolute phase of the pump beam compared to the probe beam. As previously established, our signal only depends on the relative phase of the pulses within the pump beam. Consequently, we can change the sign of this scattering while maintaining the sign of the signal by applying a phase shift to the entire pump beam while maintaining the same phase difference within the pump beam.

Spectroscopic experiments with more than two pulses can have superfluous signals due to fewer than the full number of pulses interacting with the sample. For example, our 2D pulse sequence requires three optical pulses, two pump pulses and a probe pulse. If only one of the pump pulses interacts with any given molecule in our sample, we can get a transient absorption signal in the probe beam which does not contribute to the 2D spectrum. To avoid this, we can also choose to select a pairs of pump pulses, differing in phase, such that the signals resulting transient absorption are eliminated.

Combining the cycling of phases for both pump transient absorption background and scattering reduction, we end up with a four pulse sequence for each given t_1 time, which can be combined as follows

$$S_{cyc} = R_{sig}(0,0) - R_{sig}(\pi,0) + R_{sig}(\pi,\pi) - R_{sig}(0,\pi), \tag{2.7}$$

with each $R_{sig}(\phi_1, \phi_2)$ contributing to the total signal while eliminating transient absorption background and scattering. Unfortunately, this phase cycling requires four times as many unique waveforms compared to simply stepping the t_1 time.

A quasi-phase cycling method has been developed for traditional delay-line based 2D utilizing an oscillating glass slide as a calibrated phase shift.[78] Though effective at signal enhancement and scatter removal, the method is limited to these benefits and not as flexible as the full phase control afforded by a phase-capable pulse shaper.

Phase cycling also allows the extraction of specific pathways from pump-probe geometry 2D spectra that would not otherwise be resolved, such as retrieving the rephasing and non-rephasing separately.[79]

2.1.1.2 Rotating Frame

A common technique in RF electronics is the use of heterodyning to take a high-frequency signal and mix it to a lower frequency where measurement is easier. It should be noted, heterodyning in electronics is taken to mean something slightly different than in ultrafast optics, where this refers to the interference of different optical pulses which may be derived from the same oscillator. For example, in a typical analog FM radio the deconvolution of audio from the FM signal is not done at the signal frequency, but rather the tuner is set to a particular frequency which mixes with the detected signal producing frequency modulations from 0 to about 50 kHz. These signals are much easier to process with electronic hardware.

In order to achieve the same affect in an optical experiment, we need to mix the the optical field at the vibrational frequency with an additional frequency. Fortunately, as discussed in the previous sections on phase cycling and 2D spectra in general, we can add arbitrary phases to our shaped optical pulses. To achieve measurement in a rotating frame, we simply add a known phase with the shaper that has the same effect of a frequency mixed at the sample. We can add a known phase between the first and second pulses of the 2D sequence and later remove that in analysis. Mathematically, we change the equation (2.4) to

$$M(\omega) = e^{i(-\omega t_1+\omega_{rot}t_1+b_0+b_2(\omega-\omega_0)^2+M_\omega(\omega))} \tag{2.8}$$

$$*M_A(\omega), \tag{2.9}$$

where ω_{rot} is the frequency we are mixing with. Now the oscillations due to the

vibration, on account of the added artificial phase, are oscillating at $\omega_{vib} - \omega rot$ which can be much slower. In a typical experiment, we will remove 1750 wave numbers from a 2000 wavenumber oscillation, resulting in an oscillation period 4 times longer. Having an oscillation 4 times longer results in a Nyquist limit 4 times less for stepping of t_1 while still maintaining the same number of samples per signal cycle. Ergo, we can reduce the number of unique waveforms required for a measurement by a factor of 4. Moreover, the spectral resolution of the resulting 2D spectrum is not dependent upon the sampling frequency but rather the maximum delay. Thus, we are still able to maintain good spectral resolution with fewer total points sampled.

2.1.2 Implementation

The control of phase and amplitude of laser pulses is well established for near IR and in the visible but relatively new to the mid-infrared. Ti:Sapphire lasers are used as light sources for many such experiments on account of their large spectral bandwidth. Near IR experiments are typically preformed directly with amplified TI:Sapphire beams. Visible experiments are typically preformed with second harmonic generation stages near 400 nm, or using a non-collinear optical parametric amplifier throughout the visible. The typical methods for pulse shaping include acoustooptic, electrooptic, liquid crystal modulator, and deformable mirrors. However, many of these methods are not easily applicable to the mid-infrared due to limitations of the materials used or the lack of sufficient modulation capabilities. Most techniques are limited by material absorption at mid-infrared frequencies. Deformable mirrors do not have this problem, however, since mid-infrared light has 10 times, or more, the wavelength compared to visible light, the depth of modulation a deformable mirror must deform is much larger and not feasible with current technology.

Only recently has an acoustooptic system been developed by Isomet Inc. and The Zanni group from the University of Wisconson-Madison.[11] A sufficiently large germa-

nium crystal is used with several acoustic transducers. Unlike most AOM materials, germanium is transparent throughout most of the mid-infrared. Germanium is not a perfect solution, as it does absorb acoustic energy and can be over-heated.

An additional approach, known as indirect pulse shaping, has been proposed,[80–82], but has not yet implemented to the knowledge of the author. Indirect pulse shaping is when pulses are shaped by first shaping in the near-IR and transferring this shape to the mid-infrared by nonlinear optical processes. The expectation is the shape applied to the pump laser pulse will be transferred through the nonlinear process to the final frequency range. This could have significant disadvantages, however. Non-linear conversion efficiencies are typically highest for transform-limited pulses. By having shaped, non-transform limited pulses nonlinear conversion could be compromised and will certainly change the pulse shapes applied.

2.2 Optical System

Our optical system is diagramed in figure 2.1. At the basic level the system consists of a source laser, an optical parametric amplifier (OPA), a difference frequency generation (DFG) stage, a pulse shaping stage, a sample cell, sum frequency generation (SFG) (which we call upconvertion,) and finally a spectrometer. Each of these stages will be discussed below.

2.2.1 Mid-Infrared Source

Naturally, our optical system requires a source of mid-infrared laser pulses. Our lab has several mid-infrared sources based on the the source described by Kaindl *et. al.*[83] That is, we use a standard two-stage optical parametric amplifier followed by a difference frequency stage to produce mid-infrared light pulses near 5μ. For the system used in our AOM shaping setup, the total input power to the system is about ≈ 600 mW from a Ti:Sapphire amplifier (100fs centered at 800nm with a 1kHz

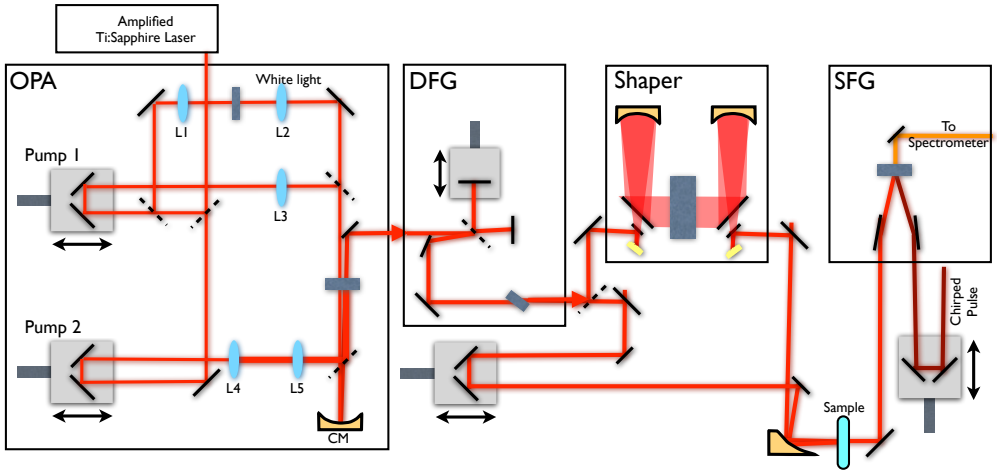

Figure 2.1: Layout of the mid-infrared pulse shaping system. Starting from an amplified Ti:Sapphire laser a two-pass white-light-seeded, OPA is driven. The signal and idler of the OPA is recombined in a DFG stage producing 5 μm light which is split between pump and probe paths. The pump path is shaped by an AOM-based 4-f shaper then recompiled with the time-delayed probe at the sample cell. Finally the probe is unconverted by SFG with 800nm Ti:Sapphire light and detected in a spectrometer.

repetition rate).

The optical parametric amplifier (OPA) is a standard design.[84] The OPA process is seeded by a white light continuum generated by focusing a 4% reflection of the first stage pump beam off of a window into a 1 mm sapphire window. This seeds a Type II OPA process tunable near 800 nm(e) $\rightarrow$ 1400 nm(o) + 1900 nm(e) in β-barium borate (BBO). This process is phase matched in a $5 \times 5 \times 4$ mm BBO crystal cut for $\theta = 27^{\circ}$ phase matching and this gives $d_{eff} = 1.55$. In our case, this first OPA stage give about 2 mW combines signal and idler power. For such a second order process, the typically calculated amplitudes of infinite plane waves as a function of linear propagation z though the crystal are

$$A_i(z,\omega) \;=\; i\gamma_i \int_{-\infty}^{\infty} A_p(0,\omega_p) A_s^*(0,\omega_s) e^{-i\tau\omega_s} d\omega_s \tag{2.10}$$

where $A_p(z,\omega), A_s(z,\omega), A_i(z,\omega)$ represent pump, signal, and idler amplitude respec-

tively.

The signal from the first OPA stage ($\approx$ 1400nm) is passed unfocused to a second amplification stage. The second stage OPA is pumped with a $\approx$ 520 mW Ti:Sapphire power. This typically yields a signal and idler power of 80-120mW combined. The signal and Idler are split into separate paths to compensate for the relative time delay from travel through the previous amplification stage. After recombining, the two beams are sent nearly colinearly into a 1-mm GaSe crystal for difference frequency generation (DFG) to produce 2μJ mid-infrared light pulses at or near 5000nm, or 2000 cm^{-1}. Typical bandwidths are typically 100-125 cm^{-1} in the mid-infrared.

After being filtered to remove remaining higher frequency beams, the mid-infrared is split with a 2° wedged window to produce a weak probe beam and stronger pump beam. The probe is directed towards a standard optical delay line and then onto the sample. The pump beam continues to our mid-infrared shaper.

2.3 Acoustooptic Modulation

The acoustooptic modulator (AOM) works by the linear optical process of adding an acoustic wave to an optical wave propagating through a crystal. If we consider a crystal atom subject to an acoustic wave, $\vec{P}_{ao} = A_{ao}e^{-\vec{k}_{ao}t}$ at the same time as an optical wave $\vec{E}_o = A_{in}e^{-\vec{k}_{in}t}$. The acoustic wave will result in a slight modulation of the nuclear center, while the optical wave results in an optical polarization of the electron orbitals. The result is an effective grating in the material which multiplies the two fields. In the following, we shall refer to the input optical beam as the undeflected beam and the acoustooptic sum wave and the deflected beam.

$$E_{out} = A_{ao}e^{-\vec{k}_{ao}t}A_{in}e^{-\vec{k}_{in}t} \tag{2.11}$$

$$= A_{ao}A_{in}e^{-(\vec{k}_{in}+\vec{k}_{ao})t}. \tag{2.12}$$

We observe that the the amplitudes multiply and the wavevectors add. From this we can modulate the amplitude and add a nearly arbitrary phase to the optical pulse.

2.3.0.1 AOM Geometry

Two common choices of geometries are to take the optical waves parallel or perpendicular to the acoustic wave. As discussed in the previous sections, the pulse shaping with effectively arbitrary control of the phase and amplitude of the deflected optical beam results in the most utility. This is best achieved when $\vec{k}_{in}$ and $\vec{k}_{ao}$ are nearly perpendicular. This allows for a spatial separation of deflected and undeflected waves as well. Consider the case where $k_o = (0, 0, \omega_{opt})$ and $k_a = (\omega_{ao}, 0, 0)$ where $\hat{x}$ and $\hat{y}$ define the width and hight of an AOM crystal which is perpendicular to $\hat{z}$, the direction of the input optical beam.

From equation (2.12), the deflected field would then have wavevector $k_{out} = (\omega_a, 0, \omega_{opt})$. This results in a wave that has a slightly higher frequency and is deflected slightly in the $\hat{x}$-direction compared to the input optical wave. Because AOMs usually operate in the regime $\omega_a \ll \omega_{opt}$, the change in optical frequency is negligible. However, the spatial change from pure $\hat{z}$ propagation to include a small component in the $\hat{x}$-direction is important. In the case of our system, this accounts for an approximate 2° divergence in propagation direction, allowing for complete spacial separation of the deflected and undeflected beams after only a short propagation distance. The geometry with parallel acoustic and optical propagation has the disadvantage that without very high power one cannot achieve as high a dynamic range of amplitudes because any optical beam that does not interact remains as background. The beam that is not diffracted in the perpendicular geometry is quickly lost due to a different wavevector direction. However, the parallel geometry has the advantage of a much simpler optical geometry and simple alignment.

A second advantage of the perpendicular geometry is that it allows for a simple

mapping of the wave amplitude to a frequency dependent wave amplitude via a 4-f shaping geometry. The details of this optical setup will be covered later, but for now, the important aspect is that it allows us to disperse the spectral components of the input optical wave along the spacial x-dimension of the AOM crystal. This allows us to control the amplitude and phase as above, but with the added degree of control with respect to the optical frequency.

2.3.1 Pump-probe Delays

In our current layout, we have a minimum step of ≈50fs, which has a known accuracy of less than 5 fs out to a maximum of 200ps for the t_2 waiting time delay. That is, our motors don't always end up at the position we tell them to go to, but we know where they are to better than 5 fs. We can improve this by about 5 times (1 fs resolution with minimum steps of ≈ 10 fs minimum steps out to 100 ps) if using alternate motors in our lab. While these motors are course compared to many high-end motors used in ultrafast optical delays, they have a higher maximum velocity, which is beneficial for some of our lab's measurements. Moreover, for the systems we most often consider we do not require time steps smaller than 50 fs for the t_2 waiting time.

2.3.2 Sample Cell

Our group uses a simple sample cell for most spectra. The cell is a cylinder of aluminum, tapped with threads to secure 1", 32 thread per inch threaded brass rings, which hold calcium fluoride windows in place. These windows are 1 inch in diameter and typically 3mm thick. Windows are separated by 100 to 200 μ Teflon spacers. Additional thicker Teflon spacers are used to prevent cracking of the calcium fluoride windows as they are secured. Our retaining rings are generally made from brass to prevent binding with the aluminum cell bodies.

I also built a temperature-controlled cell, which has the same geometry embedded in an aluminum block with a thermo-electric based cooling element. This cell is used for temperature dependent data both with 2DIR and FTIR. Studies within the group on small molecule metal carbonyls in various solvents[58], small molecule metal carbonyls in glass forming liquids[3], and peptides[85] have all benefited from the ability to control temperature at sample cell.

The temperature source capable of maintaining stable temperatures within better than half a degree Celsius, over a range of -10 to 80C. The system operates using a thermoelectric cooler (TEC) which is capable of actively maintaining or changing temperatures using a an electric current to pump heat. Any given temperature is maintained using real-time measurements by a terminator circuit and control voltages are maintained by a custom circuit driven by a proportional integral derivative (PID) control loop implemented in LabVIEW. The system can use a relatively large amount of current, in excess of 5A, when heating or cooling. However, when maintaining a temperature, the current draw is much less.

2.3.3 Upconversion

One novel aspect of mid-infrared spectroscopy in the Kubaych lab is the use of upconversion.[30;86;87] In this process, mid-infrared light from the system under study is sent into a sum frequency generation crystal with 800 nm light. After sum frequency generation, the output light is visible and detectable by a standard visible spectrometer and camera system. This process offers several advantages. Visible spectrometers and cameras offer better spectral resolution that is less expensive compared with mid-infrared spectrometer and detectors and have fewer complications due to overlapping diffraction orders. Additionally, the use of well-developed spectrometer cameras allows us to detect the full spectrum at the laser repetition rate of 1 kHz. These advances have allowed our lab to have unprecedented speed in the collection

of multidimensional spectra. Use of pulse shaping can extend this to new samples that are not under the previous boxcar geometry. Most notably, pulse shaping allows for phase cycling. This allows the removal of background scattering from many types of samples. Samples such as glasses, proteins, and those samples with dissolved particles, can be studied without excessive scattering with the shaper system.

2.4 Electronic Hardware

The basic control of output hardware is accomplished via custom Matlab code and vendor-supplied drivers. The Compugen 4300 generation board has 4 semi-independent output channels. We choose to use two channels for the direct generation of RF waveforms for our RF amplifier. One channel provides a customizable trigger, and the last channel is used to output a copy of the main RF waveforms for viewing on an oscilloscope and general diagnostics. There is an additional digital marker output intended as a trigger output. However, most of our equipment cannot recognize this signal as it is very short.

Generated RF waveforms are amplified from ≈ 1 mW to ≈ 40 W by an RF amplifier(RFA-1160/4-1ZP from Isomet Corp). RF is then sent to 4 transducers on a 10 by 55mm germanium acousto-optic crystal(LS600-1109-10 From Isomet Corp), AR coated for $4.7 - 6.7\mu$m. The transducers setup a traveling sound wave in the germanium crystal off which the optical waves the diffract. It is important to note that the sound waves are effectively stationary during the ultrafast pulse in the crystal.

2.4.1 Triggering Systems

Since the optical pulse must arrive at a very specific time relative to the acoustic wave, triggering quality is paramount. The RF wave generation is triggered by the previous optical pulse so that the RF can be generated and feed onto the crystal before the current optical pulse arrives. Long, low jitter trigger delays are set using

a Stanford Research Systems delay box.

Relative jitter between the optical pulse and the acoustic wave of only 1 ns is sufficient to undermine the experiment. Moreover, jitter as short as 200 ps is easily measurable due to our phase sensitive optical methods. In order to ensure the best possible phase stability, we used a 40 MHz reference signal from our laser oscillator. A field programmable gate array (FPGA) is then custom programmed to generate a 280 MHz clock signal for our RF arbitrary waveform generator. If this external clock is not used, a 0-4 ns jitter is present on the RF output. This is due the hardware waiting to update output until the non-locked internal clock is updated. This jitter causes an optical phase jitter of $\approx \frac{\pi}{3}$. the FPGA synchronizes the AWG external clock with locked to laser oscillator. This reduces problematic timing jitter by about an order of magnitude.

Since the shaper experiments typically involve many unique optical waveforms in a very specific order, we must keep track of the spectrum for each waveform. This is achieved by triggering the spectrometer using a channel of the arbitrary waveform generator so that triggers only occur when a waveform is generated.

2.4.1.1 FPGA

FPGAs are frequently used in applications requiring high rate parallel data, and as such typically have high-quality, dedicated clocking circuitry. Our FPGA, a development board containing a Spartan-6 FPGA (Nexys 3 system board from Digilent), is capable of reliable clocks up to 1080 MHz. The internal phase-locked loop (PLL) and delay locked loop (DLL) sub-systems are setup to take the 40 MHz oscillator signal from our laser. The output of the PLL, which is stabilized, is then feed into the DLL with a clock multiplication circuit where a 7/1 multiplicative factor generates the 280MHz used for our external clock. The FPGA is also programmed to generate a stable 1kHz which can be used to trigger our amplification laser, as well as sev-

eral other 1kHz triggers at set delays and advances relative to the main trigger. The FPGA can also be programmed to serve as a logic box for our lab's box-cars geometry 2D experiment, which uses AND logic to control triggers for synchronization.

2.4.2 Spectrometer

A 0.55m grating spectrometer (TRIAX 500 from Horiba) with a Princeton Instruments PIXIS 100 camera is used for detection. The spectrometer is set so that the spectrum is centered on the camera and remain unchanged over the course of many experiments. The camera is controlled by Winspec software by Roper Scientific via TCP/IP messages sent from LabView. The camera is triggered by a custom triggering box which amplifies the trigger channel generated in the Gage board discussed above.

2.4.3 AOM Software and Control

AOM requires acoustic signals in the crystal. Due to the high speed of sound transmission in germanium, these sound waves are in the tens of MHz. This requires radio frequency (RF) electronics to drive so that our acoustic waves can be computer controlled. The software to accomplish this is written in Matlab to tack advantage of the high speed manipulation of large data sets and simplified complex number representation, without requiring extensive programming in C or Fortran.

Presented in figure 2.2 is an overview of the software controlling pulse shaping hardware and data acquisition. Details on the software is beyond the scope of this document. Due to hardware limitations, the software runs on 2 separate computers. One computer is dedicated to shaping and RF signal output, while the other computer is dedicated to data acquisition and spectrometer control. In order to synchronize the experiment, standard transmission control protocol and internet protocol (TCP/IP) communications are established between the 2 computers. The general flow of the

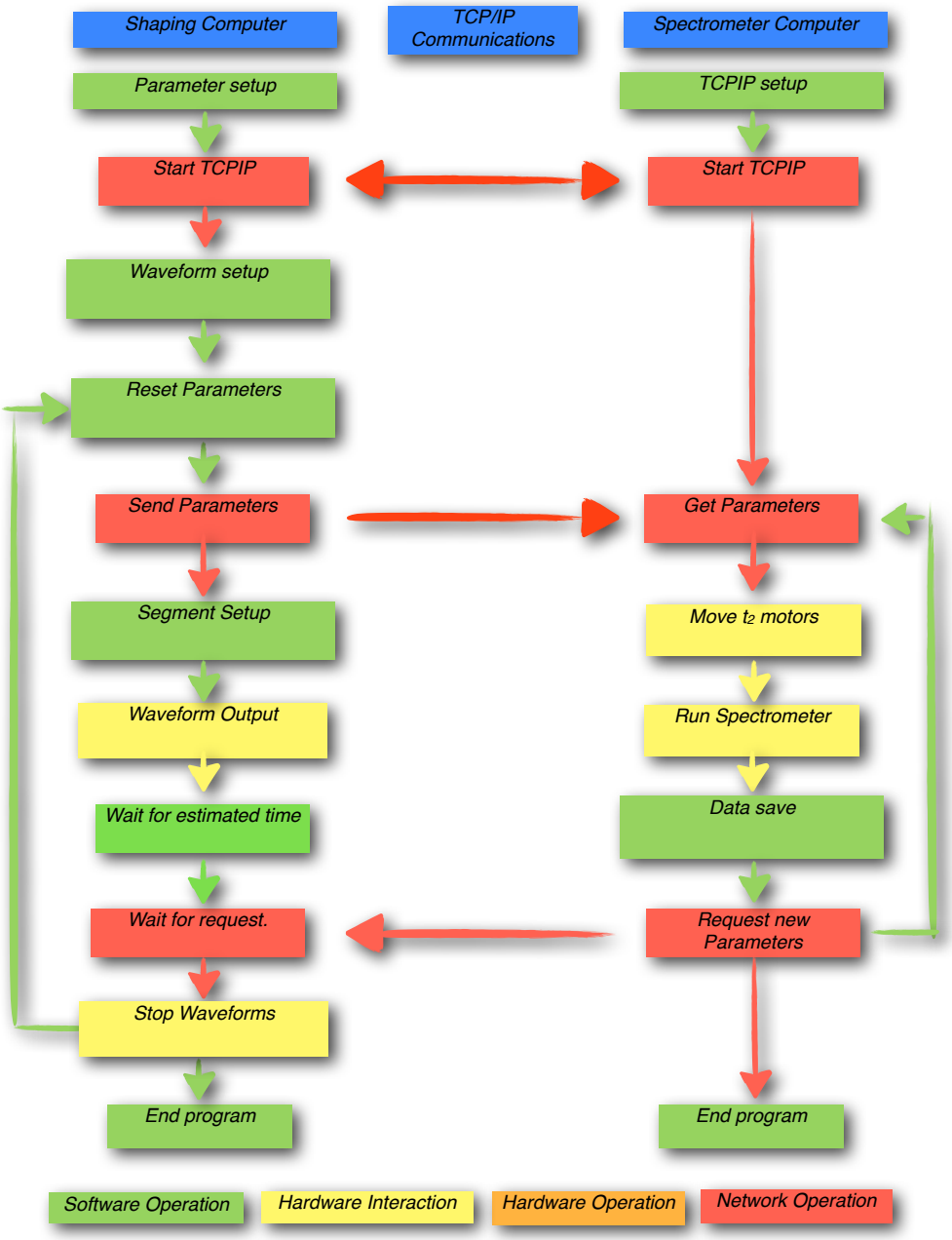

Figure 2.2: Flow chart of the control software for 2DIR.

Component	*Supplier*	*Part Number*	*Cost*
Mid-IR pulsed source	custom built	*NA*	high
Acoustooptic crystal	Isomet	LS600-1109-10	$ 25k
RF amplifier	Isomet	RFA1106/4-ZP	-
Arbitrary waveform generator	Gage	Compugen 4300	$ 6k
Digital delay generator	Stanford Research Systems	DG535	$ 6k
Water chiller and circulator	Neslab	RTE-220	$ 2.5k
FPGA demo board	Digilent	Nexys 3	$ 150

Table 2.1: Summary of major pulse shaping components. Note that all Isomet products were combined in one quotation.

software is first comprised of experimental parameter set-up and then TCP/IP set-up. Then TCP/IP communications are established, followed by waveform set up and then a loop to acquire the required spectral data. All of the shaping software is done in Matlab, whereas all of the control data acquisition software is done in LabVIEW.

In figure 2.2, green represents processes that occur in software on a particular computer. Red boxes represent communications between the two computers, and yellow boxes represent interaction with hardware. During a typical run, the segment setup can be the longest step in a typical loop. As discussed in section 2.1.1, quite a few this unique waveforms must be output. Memory limitations in the RF generation board limit the number of unique waveforms that can be loaded into memory at any given time. Unfortunately, the arbitrary waveform generator board, though on the computer's internal PCI bus, has a very slow memory upload rate. It is not uncommon for a complete load of the memory to take as much as 1 min. In order to minimize this, the data acquisition software is set to move t_2 motors through a sequence of the required t_2 steps before moving on to new t_1 times as determined in the waveforms of the arbitrary waveform generator.

Table 2.1 summarizes some of the major components of the shaper-based 2DIR spectrometer system.

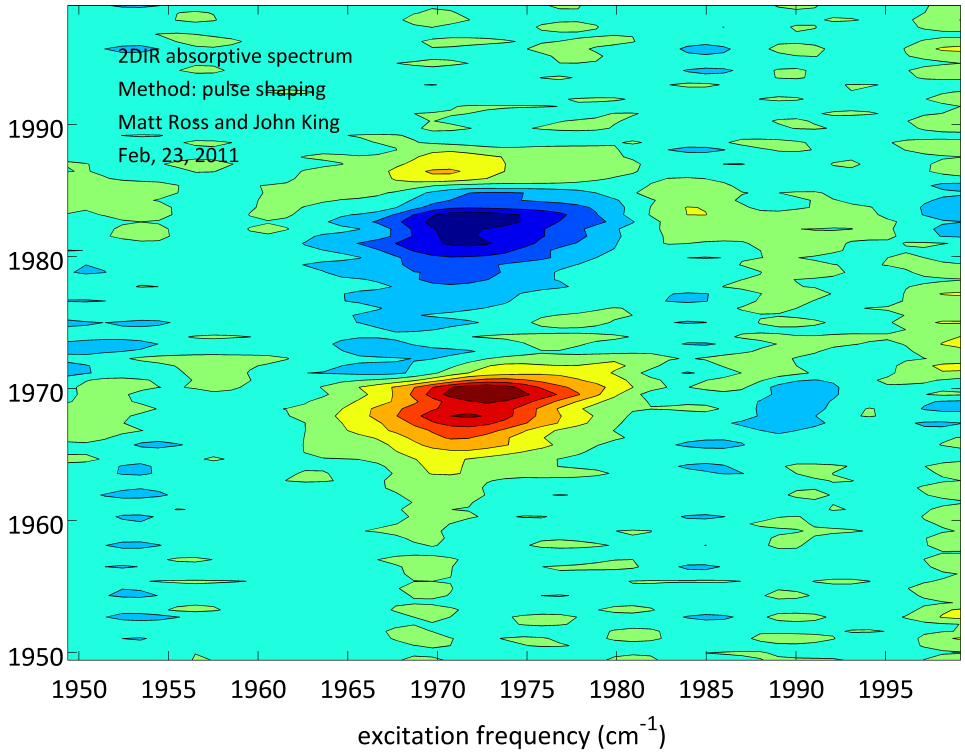

Figure 2.3: Our first 2DIR spectrum obtained by pulse shaping in the mid-infrared. This is an absorptive spectrum of $W(CO)_8$. Note that the excitation frequency calibration is off by about 10 cm^{-1}.

2.5 2DIR Spectra by Shaping

Several early 2DIR spectra acquired by pulse shaping methods are shown in figures 2.3, 2.4, and 2.5. Figure 2.3 is the 1st reliable 2-D spectra obtained with our system. This system is tungsten octacarbonyl, chosen as it has a single strong frequency within the range of our system. While somewhat noisy, this spectrum shows all of the expected features. The upper blue region representing a ground state bleach and the lower red region representing the anharmonically shifted excited state absorption. Note that due to an early miss calibration, the horizontal axis is shifted by 10 wave numbers. Figure 2.4 is a 2DIR spectrum of dicarbonylacetylacetonato rhodium(I) (RDC) in hexane. In comparison to the previous spectrum this spectrum has better

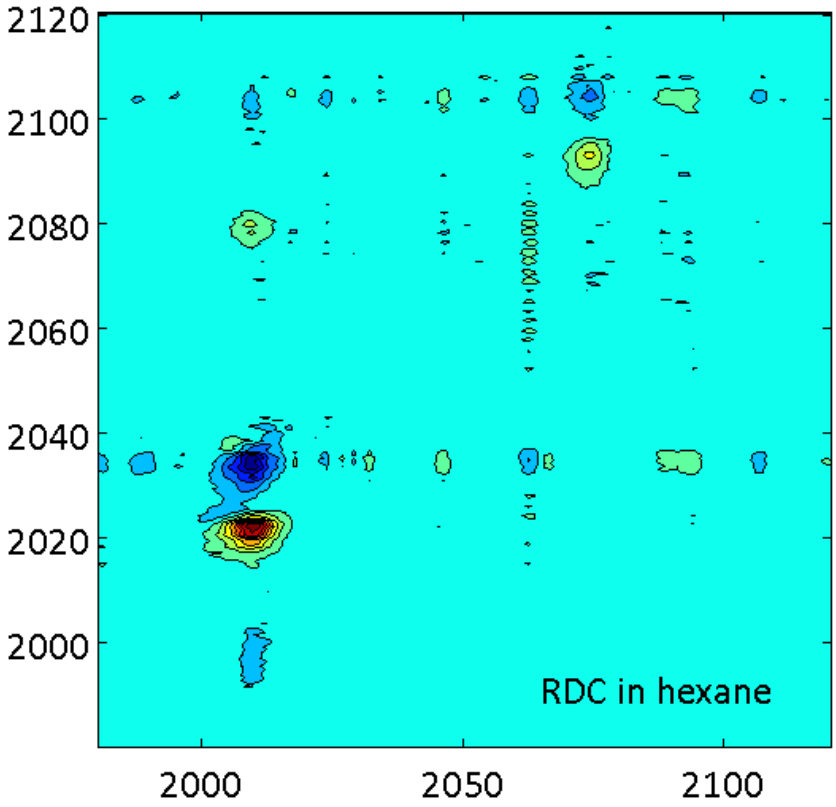

Figure 2.4: An early 2DIR spectrum of RDC in hexane.

spectral resolution along the ω_1 excitation axis as it included a longer scan of t_1 times. Figure 2.5 is a later spectrum of dimanganese decacarbonyl (DMDC) in hexane. This spectrum also has a long t_1 scan, in this case taken by combining multiple scans of fine t_1 time steps.

2.6 Shaper Diagnostics

Many diagnostics were required during the construction and use of this system. Fortunately, most calibrations were found to be stable within the system and do not need regular updating. Optical frequency to crystal position, trigger timing, and RF

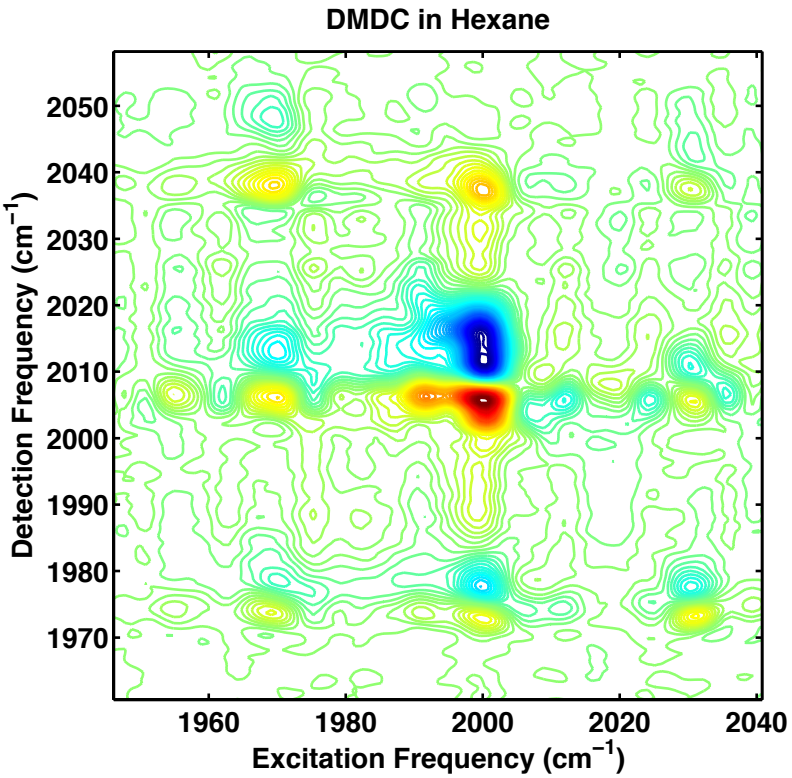

Figure 2.5: Absorptive 2D spectrum of DMDC acquired by pulse shaping.

power are the most important calibrations preformed. Additional tests preformed include tests of phase stability and repeatability, test of proper pulse sequences, RF power dependance of deflection efficiency, pulse chirp calibrations, and a test for the analysis including the effects of signal averaging and dropped spectra removal.

Optical Frequency

The mapping of optical frequency to crystal position is particularly crucial to effective pulse shaping in an AOM system. In order to correctly modulate phase and amplitude as a function of optical frequency, we must have a mapping of the optical frequency to spatial location on the crystal. The spatial position is then related to specific waveform points on our arbitrary waveform generator (AWG) signal. The primary frequency calibration was accomplished by matching notches applied in a shaped spectrum and known absorption references. A calibration with multiple absorption peaks was required to establish both absolute positioning on the AOM crystal and the linearity of signals on the crystal. The linearity procedure was only needed once because the calibration was found to be very repeatable as the sourced for our AWG clock signal, the 80MHz of the laser oscillator, is very stable.

Small changes in optical path length, mostly due to optical realignment, result in slight changes in the relative arrival time of the optical and RF signals. Because of this the RF trigger delay is regularly checked, typically each week and after any significant realignment, the overall offset in the absolute position on the crystal is adjusted by changing the system's trigger delay, which is set using an SRS delay generator (model DG535). The procedure is simple. Our reference standard, DMDC, is placed in a sample cell and mounted in the sample cell holder. Next, magnetic mounted mirrors are added which steer the pump beam along the probe beam path through the sample and onto the upconversion crystal. A dedicated "Frequency Calibration" script is run on the shaper control computer. The waveforms sent to the acoustic-optic crystal are

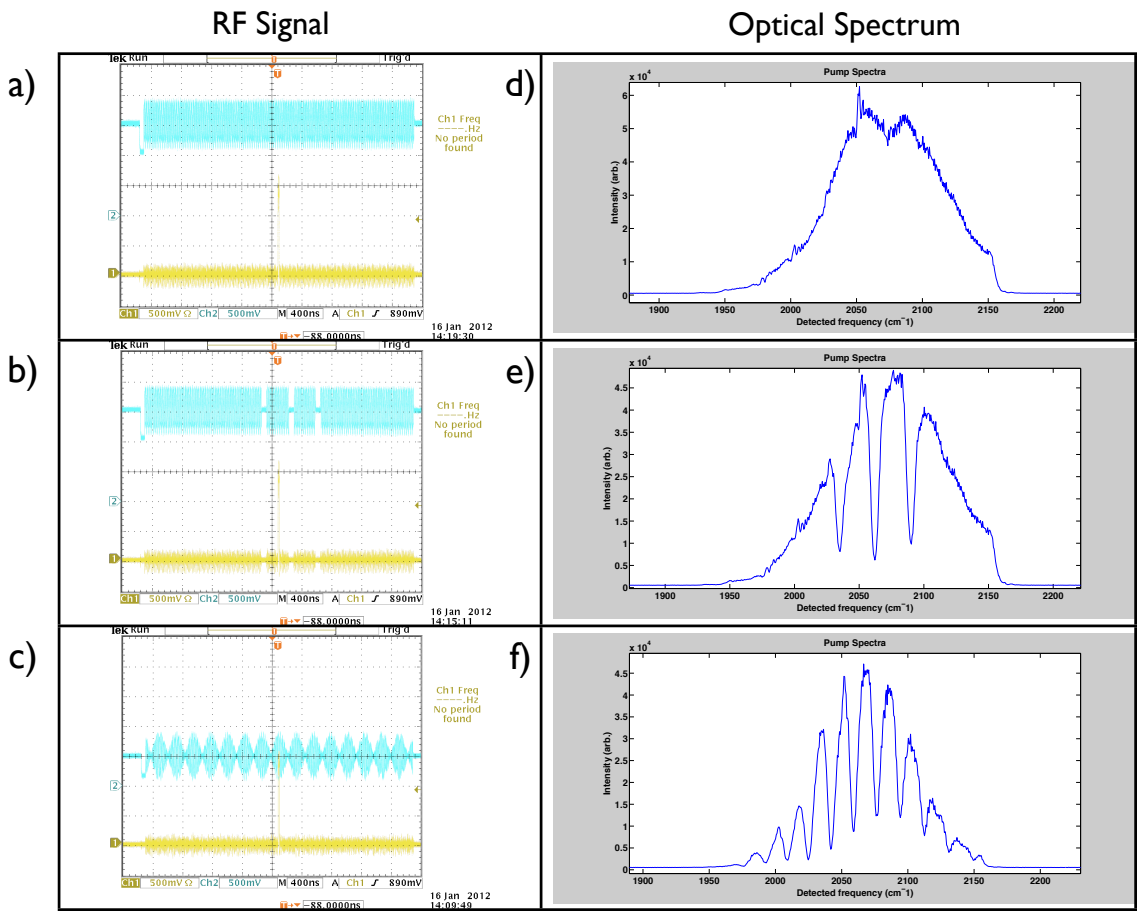

Figure 2.6: Sample RF signals for AOM and resulting optical spectrum. (a)-(c) are oscilloscope traces of the RF signals used to generate acoustic signals in the AOM crystal. (d)-(f) are the resulting diffracted optical pulse spectra.

set so that most frequencies are passed to the sample and frequencies corresponding to the DMDC spectrum are blocked. The timing is then adjusted so that the real DMDC transitions overlap with the "fake" absorptions of the shaped pulse. The process is monitored real-time on the spectrometer after upconversion. A sample frequency calibration waveform and the corresponding shaped pulse spectrum is shown in figure 2.6b and 2.6e, respectively.

Figure 2.6a is a full carrier signal with no modulation for transmission of the full pulse without amplitude or phase shaping. Figure 2.6d is the optical pulse spectrum

diffracted from the RF signal in 2.6a. For calibrating the waveforms, we match three "knock-outs" in the RF carrier of 2.6a to make 2.6b. By adjusting the three frequencies not deflected by the frequency calibration waveform (figure 2.6b) to match this absorption spectrum of dimangonese decacarbonyl (DMDC), we are able to set mapping of frequency to relative position on the AOM crystal. The deflected spectrum from the RF of figure 2.6b is shown in figure 2.6e. Finally figure 2.6c shows the RF signal applied to the AOM crystal for producing a pulse pair, in this case separated by 1.8 ps. Again, the resulting deflected spectrum is shown in 2.6f.

Pump-probe Spectra

While the shaper system is certainly capable of a great deal more, the AOM can simply turn the pump beam on and off by sending waveforms of "all on" and "no waveform" and act as a rather expensive and complicated beam chopper. This turns out to be valuable to aid alignment of the pump and probe overlap in the sample cell. As such, there is a dedicated program to chop the pump on and off.

Figure 2.7 shows the absorption of DMDC as reported by the probe spectrum, (a) and a typical pump probe take during alignment of DMDC in hexane with about 4k laser shots (4sec), (b). The ground state bleaches on each of the three separable peaks and the excited state absorptions are visible for two of the peaks on the pump-probe spectrum. The third ESA may be present, but it is not clear with this level of signal to noise.

Shaped Pulse Phase Stability

While the calibrations of RF frequency and proper programming ensure that programed time delays in software are properly converted to pulse delays between portions of the shaped pulse, some confirmation was necessary. Spectral interferometry measurements of shaped pulses and the shaped pulse with the unshaped pulse, pro-

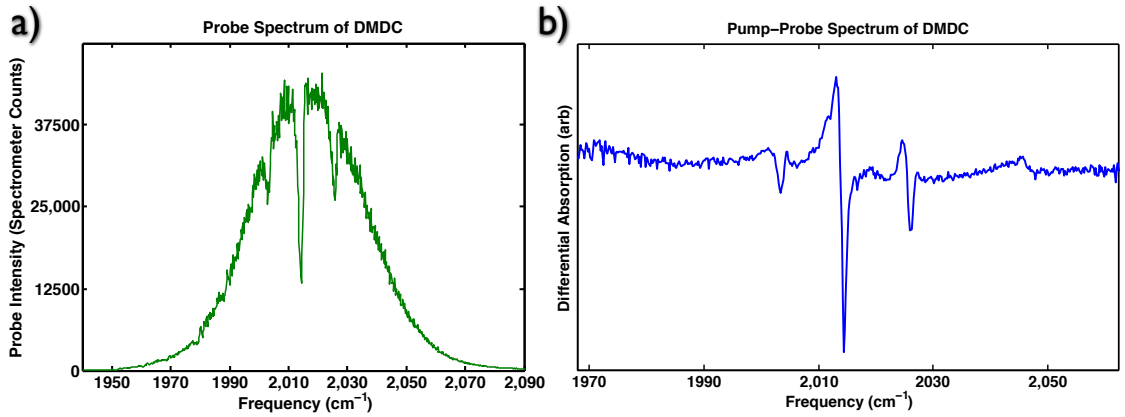

Figure 2.7: Pump-probe diagnostic spectra. The absorption of DMDC as reported by the probe spectrum, (a) and a typical pump probe take during alignment of DMDC in hexane with about 4k laser shots (4sec), (b).

vide this confirmation. Figure 2.8 shows 32 spectra of a shaped pulse pair. Each spectrum is a single laser shot during a multiple waveform experiment. In this particular case, the experimental run was approximately 30 seconds. Accordingly, each of the 32 spectra in figure 2.8 was taken approximately one second apart. The time in between these spectra the system was outputting other spectra for other pulse delays. Figure 2.8 is intended to show the repeatability of the same pulse pair, as programmed by the RF generator, over the course of an experiment. With the exception of two spectra, each of the spectra shown in the figure overlap the others within laser power stability. The two exceptions will be discussed later.

Phase Cycling Tests

By enabling the phase cycling algorithm in the software, we are also able to confirm that the phases of the pulses change as expected. This is evidence for proper application of the phase to the shaped pulse, proper shot-to-shot changes in the shaping acoustic field, and the reliability of system timing and triggering. Figure 2.9 shows several shaped pump spectra with relative phase shifts to active phase cycling.

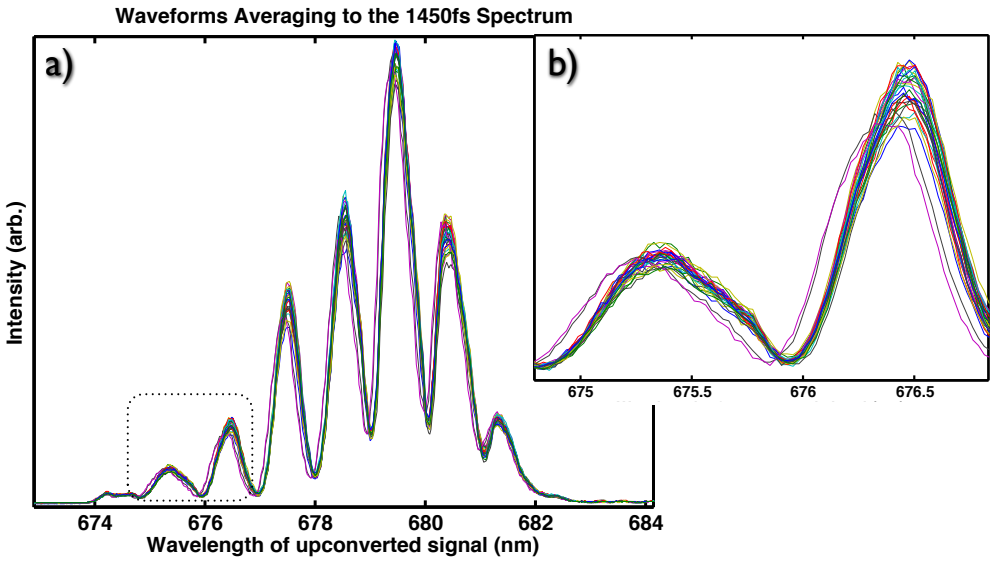

Figure 2.8: Waveforms averaging to a single time-step waveform. Here, 32 single-shot spectra of two shaped pulses with a 1450 fs separation added are shown which all have the same shaper waveform. Subfigure (a) is the entire unconverted spectrum, whereas (b) is zoomed in on the dotted box.

In this case, a single t_1 delay of 1448 fs is shown. The four waveforms differ by cycling differences of π in the phase relative to the input optical pulse and the phase of the two shaped pulses relative too one another. In the notation of section 2.1.1, the four plotted waveforms are for signals $R_{sig}(0,0)$, $R_{sig}(\pi,0)$, $R_{sig}(\pi,\pi)$, and $R_{sig}(0,\pi)$. Continuing on, we can plot the signal after adding and subtracting these terms as in equation (2.7).

Figure 2.10 shows to the results of addition and subtraction of the respective phase cycled spectra. The blue spectrum in figure reference is for the phase cycling shown in figure 2.9, and the green spectrum is for a set of phase cycled spectra delayed 2 fs. longer than those in blue, that is $t_1 = 1450$ fs.

2.6.1 Spectral Resolution

In our system, the detection axis spectral resolution is set by our spectrometer. The spectral resolution of the excitation axis is set by the maximum time delay in

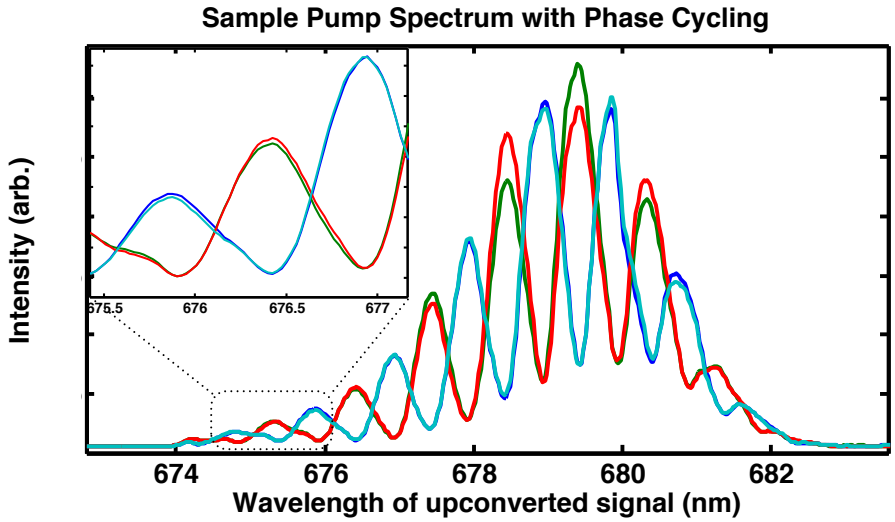

Figure 2.9: Four phase-cycled spectra for a single time delay. The insert is zoomed in on the dotted box.

the t_1 time sequence. Then the spectral resolution is set by the Fourier transform.

Due to memory limitations on the Compugen 4300 card, we are limited to about 900 unique RF waveforms without a time-consuming memory reload. Since we also use 4 waveforms for each time step to achieve necessary phase cycling, we are limited to about 225 t_1 time points per memory load.

If high resolution on the excitation axis is needed, one can simply wait the extra time needed. However, there are several methods that could be implemented in the future to expand the capabilities of the shaper system. First, and most expensive, newer arbitrary waveform generators now exist that possess larger memory capacity and faster load times, thus allowing for more waveforms in a reasonable time. An additional option could be to use methods common in NMR processing, such as analytic continuation or exponential time spacing. Since long-delay times usually contain small signals relative to the noise, NMR studies sometimes utilize an analytic fit to data that can be used to extend the long-time delays without additional noise.

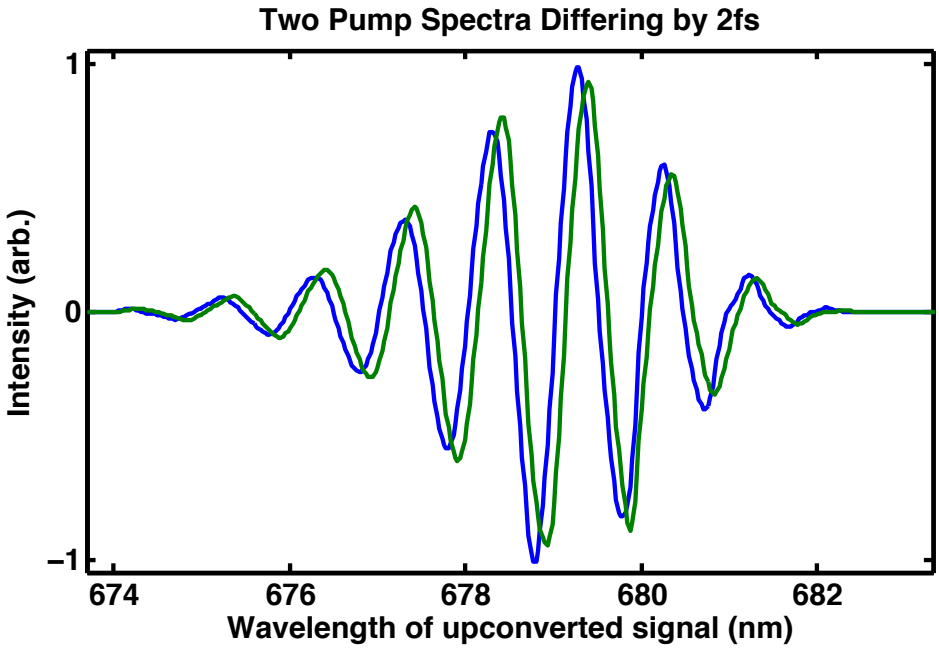

Figure 2.10: Resulting signal after phase cycling for t_1 time steps. The blue spectrum is the result of the phase cycled spectra in figure 2.9. The green is the same process for a 2 fs longer pulse separation of 1450 fs. Note that the two are clearly different, demonstrating that 2 fs time delays are reliably distinct.

Since the free induction decay is much more intense at short times, the long-time delays typically contain only a small portion of the signal, but contribute equally to the spectral resolution. An even more extreme method from NMR measurements could be the implementation of exponential sampling. This method would require significantly more work, however, since it would require a non-uniformly spaced FFT algorithm, which tend to be difficult to implement efficiently.

Quadratic Chirp

The pulse shaper introduces chirp to the shaped laser pulse due to its relatively thick germanium crystal, through which the mid-infrared pulse must propagate. Fortunately, the shaper can correct for this by adding a linear chip in the opposite direction. Recall that a linear chirp is a quadratic phase term. While we currently do not have a careful pulse characterization setup for the mid-infrared pulses, we can compare the shaped mid-infrared with the unshaped mid-infrared probe as a first order correction. This is accomplished by comparing the two beams scattered off the same pinhole and detected in a spectrometer. The relative changes in the resulting interference fringes allows for basic matching of chirp. A more detailed measurements, such as using Spectral Phase Interferometry for Direct Electric-field Reconstruction (SPIDER) setup could be done for a more careful calibrated correction.[88;89] However, it is worth noting that intentionally changing the correction within a reasonable range has no discernible effect on pump-probe signal from the shaper and little effect on any given 2D spectrum.

It is also worth noting that the use of non-collinear second harmonic generation with the 5μm beams, which is an alignment method in the Zanni group, would also allow for better chirp correction calibrations, as one could maximize the SHG signal, a reliable method to find a pulse's transform limit.

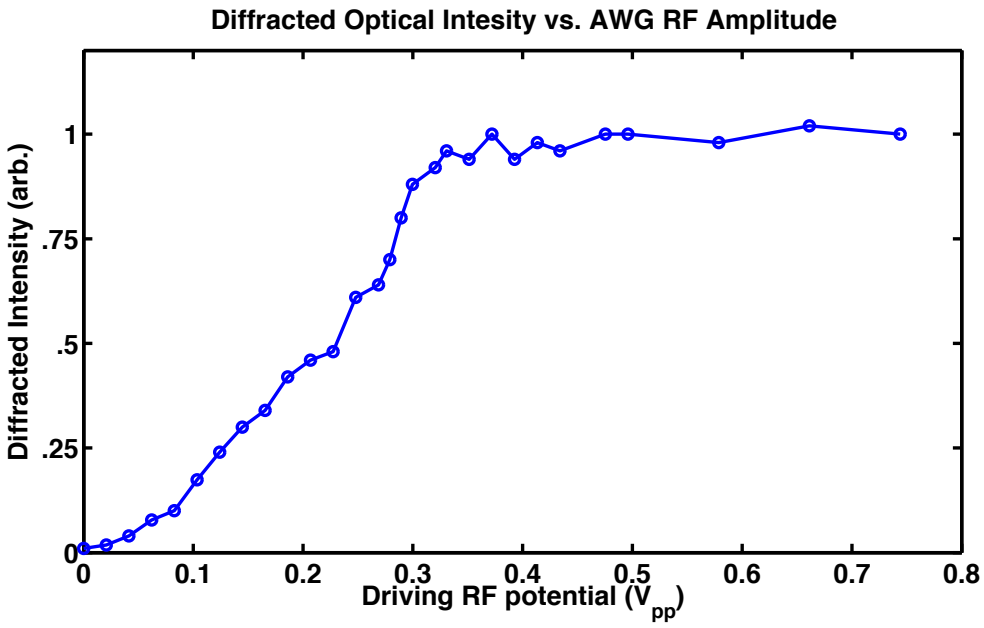

Figure 2.11: Saturation of AOM efficiency with increasing RF input power.

RF Power

The RF amplifier and acousto-optic crystal combination has a power dependent efficiency which saturates at approximately 0.3 V_{pp}, which is 1.0 mW (0.0 dB) input power. Over-driving the AOM crystal is to be avoided, as there is a non-negligible absorption of the acoustic waves at 80 MHz, which could heat the crystal to the point of damage. This was calibrated by systematically adjusting the input power to the RF amplifier. Input power was adjusted by changing the arbitrary waveform generation amplitude. Total power was measured integration of the observed signal on our spectrometer after upconversion.

Figure 2.11 shows the deflection efficiency, in arbitrary units, as a function of the peak-to-peak voltage of the RF field before the RF amplifier and AOM crystal. The system is typically operated just where the efficiency saturates, about 0.3 V_{pp}. This allows nearly the full diffraction efficiency without overheating the AOM crystal.

Trigger and Clock Jitter

A significant problem discovered during system setup was the effect of trigger and clock jitter on the optical phase of the generated pulses. As indicated in equation 2.11, the shaped optical pulse has a phase that is both the phase of the incoming pulse added to the acoustic phase. If there is any uncertainty in the relative arrival time of the acoustic signal and the optical pulse, the phase of the shaped optical pulse will pick-up that uncertainty. Moreover, what may be low jitter timing by electronics standards ($\pm$ ns over a 1ms period, or 2ppm), will give a $\pi/3$ phase jitter in the optical. Such a large jitter would undermine any phase-sensitive experiment.

Figure 2.8 shows many repeated spectra with the same shaped phase applied. 2.8a represents the entire frequency trace, whereas 2.8b is a zoom in on a single interference fringe with controls applied. On 2.8b, one can see that two of the 32 traces do not lie in the same group. These two spectra are the result of triggering misfires that are off by one clock cycle of the arbitrary waveform board. This equates to an approximately 4 ns mismatch in timing of the optical pulse relative to the acoustic wave within the AOM modulator. Without a full cycle missed, the accuracy of timing is in on the order of several hundred picoseconds. This improves the phase stability by about a factor of 10 come paired to the uncorrected timing. However, occasional glitches still can occur, as seen in figure 2.8. The timing controls are implemented on an FPGA and were discussed in more detail in section 2.4.1.1.

alcanesSqualene

CHAPTER III

Solvation of Iron Pentacarbonyl

A fundamental objective of my dissertation is the understanding of solvent dynamics as they effect solvated molecules such as solute dynamics that are modulated by solvent properties or protein dynamics modulated by solvent interactions. To this end, the interactions of iron(II) pentacarbonyl, $Fe(CO)_5$, with various solvents were studied. Of particular interest is the ability of $Fe(CO)_5$ to undergo Berry pseudorotation, a form of fluxtionality.

3.1 Background

This work investigates chemical reactions with low barriers. By low barriers, I am simply referring to barriers comparable to, or less than, k_BT. Such reactions are are easily driven by thermal fluctuations. Figure 3.1a is a cartoon of a low barrier reaction in which the barrier is not much higher than thermal fluctuations, represented by the red double-ended arrows. The dashed green arrow represents some form of catalysis, which brings the barrier even lower, possibly changing the reaction from having a barrier much higher than k_bT to a sufficiently low barrier to allow efficient conversion under reasonable conditions, such as those easily obtained in a laboratory or biological setting.

Lowering reaction barriers to the point where reactions will occur at a reasonable

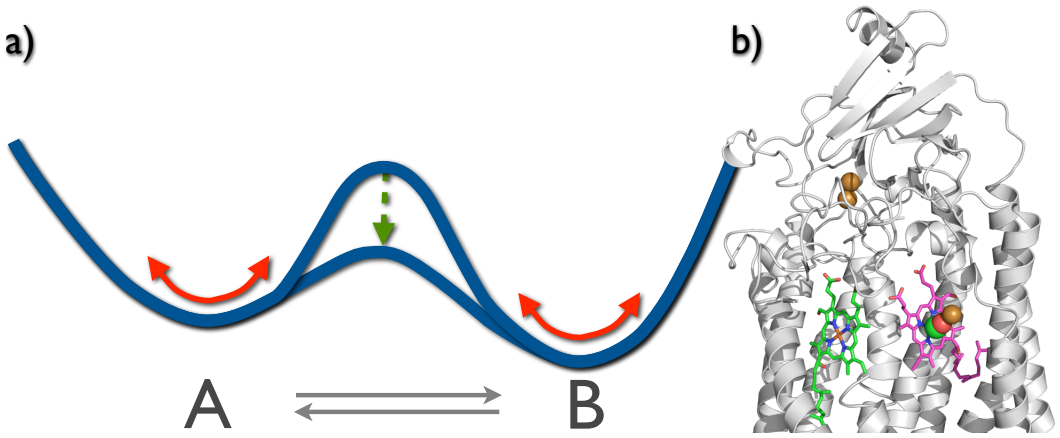

Figure 3.1: Low barrier reactions. Subfigure (a) is a cartoon of a low barrier reaction where the barrier is not much higher than thermal fluctuations, represented by the red double-ended arrows. The dashed green arrow represents some form of catalysis, which brings the barrier even lower. (b) Cytochrome C oxydase active sites from PDB file 1OCO. Cytochrome C oxydase is one of many proteins which catalyses a reaction which would not occur otherwise. The PDB structure is by Yoshikawa *et. al.*[90]

rates, catalysis, is an important topic chemistry. Beyond active work by chemists, the evolved complexity of proteins for lowering the barriers of chemical reaction speaks to the importance of lowering reaction barriers allowing for production of compounds that otherwise would not occur naturally. Figure 3.1b shows the Cytochrome C oxydase active sites from protein data bank (PDB) file 1OCO. This is one of many proteins which catalyze a reaction which is too slow to effectively occur otherwise.

The focus of this work is to examine the solvent environment of a specific simple reaction with a low barrier. Iron pentacarbonyl can undergo fluxtionality, a process by which an isomerization occurs resulting in the same compound you started with. In this case, iron pentacarbonyl exchanges ligands in different positions. This reaction is particularly suitable for looking at solvent environment effects in the liquid phase, as there is a significant simplification and the reactants are the products.

Energy, entropy, and concentrations can't change in this reaction. Moreover, the

equilibrium constant is always one. This removes the effect concentration changes have on reaction rates that must be accounted for in other systems. The equal concentrations of reactant ant product also aids the spectroscopic experiment in that the optical density of the reactants and products are the same. If a reaction were highly reactant or product-favored it could be difficult to match optical densities of both reactant and product modes to maximize signal to noise. Iron pentacarbony is also good for our experiments as it has a clean, well understood spectrum in the wavelength range of our 2DIR system. Uses of iron pentacarbonyl include as a precursor to any of a multitude of iron containing compounds[91–96], nanoparticle production[97;98], and as a source for very high purity solid iron.[99] Iron pentacarbonyl is also of interest to the time-resolved x-ray community, as evidenced by several $Fe(CO)_5$ x-ray experiments at the Stanford Linear Accelerator Complex's free electron laser, the Linear Coherent Light Source, and at Argonne National Laboratory's Advanced Photon Source.[100] Most relevant to this work are those considering the fluxtionality, such as a study by Charles Harris, *et. al.* investigating the transition state and fluxtionality in iron pentacarbonyl using multidimensional methods.[57] Additional studies by the Rose-Petruck group, including studying FTIR and computational structure of iron pentacarbonyl in alcohols,[101] are also very relevant. We seek to expand the number and types of solvents in which these transition rates have been have been studied. In the previous FTIR and computational study of iron pentacarbonyl with various alcohols, the Rose-Petruck group was not sensitive to the fluxtionality rate. By extending their work to 2DIR, We are able to measure fluxtionality rates and other measurements, such as spectral diffusion, from our 2DIR spectra.

3.1.1 Kramers' Theory

Modeling reaction rates based on crossing a barrier started in the mid to late 1880s with the publication of what came to be known as the Arrhenius equation in

1884 by Van't Hoff[102] and 1889 by Arrhenius.[103]

Traditional Transition State Theory of chemical reactions relies on predicting reaction rates based on an energetic barrier to reactions. In a gas phase or non-interacting solvent, this barrier must be overcome by kinetic energy of the reactants, typically provided by thermal energy. However, if there is a high degree of solvent interaction, the rates may be slowed by an effective friction, limiting motion on the reaction potential.

It was recognized early on that rare events, such as crossing a reaction barrier, amidst long periods of relatively stable conditions, such as fluctuations around the reactant states, is the dominant consideration in chemical reactions. In chemical reactions with a barrier, we often speak of a transition state where the chemical system is at the top of a reaction barrier and has a stochastic choice about forming reactant or products. It is the properties of these rare transition states that determine the kinetics of the reaction. The modeling of rare events still is an area of active research in many fields, especially in cases where computational simulations of rare events holds potential to drastically reduce computational time by de-emphasizing simulation time away from critical rare events.[104–107]

Kramers' theory is an attempt to better refine the prediction of chemical reaction rates. The prediction of rates in cases where there is a solvent "driving" atomic motions Kramers' theory is most applicable. Hendrik Kamers, in 1940, suggested the application of brownian motion on a potential surface to explain chemical reaction rates.[108;109] Since then, there have been many advances and interpretations.[110;111] Kramers' theory is this applicable to isomerization[37], tunneling[112], reactions involving charge transfer[113], and other phenomena. It is generally held that the folding of proteins falls within the high friction case of Kramers' theory.[114]

Following the derivations of H aggi[110] and Tucker[115], we first note that the basic

form of skin friction, or drag, for an object in motion through a fluid is

$$\vec{F} = -\eta m \vec{v}$$

, which we will call the dynamic friction on our potential. This is an effective non-conservative force that accounts for all mechanisms for energy dissipation away from the reacting molecule. However, for a particle in thermal equilibrium, any energy lost due to a particle - solvent interaction will eventually be regained as the particle's kinetic energy fluctuates. If we were to add this force to a simple equation of motion for classical motion on the potential energy surface $G(q)$ we get the Langevin equation

$$m\ \ddot{q} = \frac{\partial G(q)}{\partial q} + F + R(t) \tag{3.1}$$

$$= \frac{\partial G(q)}{\partial q} - \eta m \dot{q} + R(t) \tag{3.2}$$

where q is some position coordinate (later a reaction coordinate) and $R(t)$ is a random force acting at any given time. $R(t)$ will come to describe random "knocks" the system receives from the solvent.

Basic rate predictions are, first for TST, the rate is

$$k_{TST} = \frac{\omega_R}{2\pi} e^{\frac{-\Delta G}{k_B T}}. \tag{3.3}$$

Then for Kramers' theoryin the stron damping limit,[115]

$$k_K = \frac{1}{2\pi\tau_0}\frac{\omega_R}{\omega_T}e^{\frac{-\Delta G}{k_B T}}, \tag{3.4}$$

$$= \frac{\omega_R}{2\pi\omega_T}\left[\sqrt{\frac{\eta^2}{4}+\omega_T^2}-\frac{\eta}{2}\right]e^{\frac{-\Delta G}{k_B T}}, \tag{3.5}$$

$$= \frac{1}{\omega_T}\left[\sqrt{\frac{\eta^2}{4}+\omega_T^2}-\frac{\eta}{2}\right]k_{TST}, \tag{3.6}$$

where $\omega_R = \sqrt{\frac{\ddot{G}(q)}{m}}$ is the harmonic angular frequency of the meta-stable potential. $\omega_T = \sqrt{\frac{\ddot{G}(q)}{m}}$ is the"frequency" at the transition state, or the top of the barrier. Compare this to

We note that the pre-factor in equation (3.6) is always less than 1, thus the Kramers' rate should always be slower than the TST rate. This is reasonable as TST does not allow for the solvent to "get in the way" and knock the system back towards the reactant side and does not allow for re-crossing after passing the transition state.

In the limit of very little interaction, the friction in Kramers' theory is low and $\eta \to 0$. In this case we expect the momentum of reactant molecules to dominate near the transition state so that the likelihood of passing the transition state is primarily based on the kinetic energy of the reactant molecules. Figure 3.2 shows two limits of Kramers' theory, the low friction limit (subfigure 3.2a) and the high friction limit (subfigure 3.2b). In the low friction limit, the reaction outcome is dominated by the momentum of the system when approaching the top of the reaction barrier. In the high friction limit, the same system momentum may or may not result in a barrier crossing because the crossing is mostly driven by solvent driving the system. In the figure 3.2, this is represented by the system randomly push towards over, away from, over, and back over the bare. Note that classically in TST the path of figure 3.2b as this path passes the transition state and then re-crosses back to the reactants.

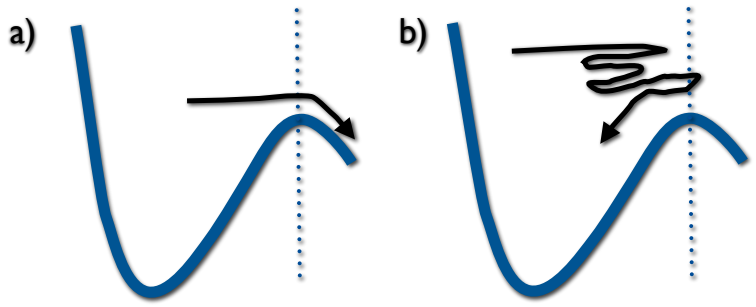

Figure 3.2: Model reaction dynamics ion the low and high friction limits.

3.1.2 Models of Microscopic Friction

There are many models for getting the microscopic friction parameter, η, used above. I will discuss the Smoluchowski limit of very high friction and the Stoke-Einstein limit where friction can be connected with bulk viscosity.

3.1.2.1 Smoluchowski Limit

If we are fully in the diffusive limit, that is the friction is so high that the reaction is entirely driven from solvent motion, we have the Smoluchowski limit.[116] Another way of stating this is that the magnitude of the acceleration term is much smaller than the friction force.

$$|m\ddot{q}| \ll |\eta m\dot{q}| \tag{3.7}$$

Then we can approximate $m\ddot{q} \approx 0$ and simplify (3.2) to

$$0 = \frac{\partial G(q)}{\partial q} - \eta m\dot{q} + R(t) \tag{3.8}$$

$$\eta m\dot{q} = \frac{\partial G(q)}{\partial q} + R(t) \tag{3.9}$$

If we were to then continue the detailed derivation, we would get the rate for barrier crossing to be the Smoluchowski rate expression

$$k_{SM} = 4Da \tag{3.10}$$

for the diffusion-controlled reaction rate is accurate only if D, is measured empirically, rather than predicted from solvent viscosity data as the microscopic environment is more complex than the macroscopic viscosity.[109] That is, as we are in the high viscosity, high drag limit, it is more likely that the molecular structure of the solvent is important, which may be less of a concern for macroscopic objects moving in the liquid.

3.1.2.2 Stoke-Einstein Diffusion

For a small spherical particle in a viscous fluid with low Reynolds number, we can predict the friction based on bulk viscosity. We expect the fiction to be proportional to the dynamic viscosity η_d.

In this form we can make a simple Kramers' theory expected rate based on the solvent viscosity.

$$k_{SE} = \frac{A}{\eta_d} e^{\frac{-\Delta G}{k_B T}}. \tag{3.11}$$

This form of Kramers' theory is most relevant for much of liquid phase chemistry as most solvents crowd around reacting species and prove a physical impediment to the reaction. Moreover, solvent molecules can push the reactant over the barrier they may not approach otherwise.

Kramers' theory and associated friction models are known to break down under some conditions. For example, *Anna et. al.* showed evidence that cyclohexane deviates from the viscosity-based friction.[37] The deviation was accounted for by noting

that simulations showed the cyclohexane formed a cage around the solvent molecules. Cadging in viscous solvents has been discussed before.[117] By forming a stabilized, structured solvent layer, or cage, the cyclohexane near the solvent molecule was unlike the bulk cyclohexane and thus did not behave as expected based on the bulk viscosity.

3.1.3 Grote-Hynes theory

If the solvent considered above were slow, that is to say it did not respond quickly to solute motions, there can be a memory effect in the friction. This is referred to as a memory friction and can be added as an additional level of complexity to the Kramers' theory picture of reaction rates. Grote-Hynes theory is this extension to the more general case of memory friction.[118][119]

$$\eta \rightarrow \int_0^t \gamma(t-\tau)d\tau \tag{3.12}$$

If we have some memory in or friction the random force term is not fully random and we can use this to get the memory kernel $\gamma(t)$. We can use the autocorrilation of the random force term,

$$\langle R(t)R(0)\rangle = mk_bT\gamma(t) \tag{3.13}$$

Using this form of a memory kernel, and following the derivation of Grote and Hynes[118] use a revised generalized Langevin equation

$$m\ddot{q} = F(t) - \int_0^t \gamma(\tau)\dot{q}(t-\tau)d\tau + R(t). \tag{3.14}$$

Then, their derivation continues by considering a conditional probability, $p(q, \dot{q}, t|q_0, \dot{q}_0)$. That is the probability of some position, q, and velacity, $\dot{q}$ at a time t given that we

know q_0 and $\dot{q}_0$ at $t = 0$. The next step is to calculate a flux of particles from one side of the barrier to the other. This turns out to be related to the velocity-velocity correlation function,

$$C_\nu(t) \;=\; \langle \dot{q}(0)\dot{q}(t)\rangle\,, \tag{3.15}$$

as the velocity is linked to how near the barrier you are. Using this they get

$$k_{GH} \;=\; \frac{1}{\omega_T}\lim_{t\to\infty}\frac{C_\nu(t)}{\int_0^t C_\nu(\tau)d\tau}. \tag{3.16}$$

If we take $G(q)$ to be harmonic, we can get an expansion of $C_\nu(t)$ as

$$C_\nu(t) \;=\; \frac{1}{\omega_T^2}\left(-\sum_n c_n\lambda_r e^{\lambda_n t} + c_r\lambda_r e^{\lambda_r t}\right) \tag{3.17}$$

Since we are only interested in the long-time limit for t, all the terms with negative exponentials decay away and we get $k_s \to \frac{\lambda_r}{\omega_T}$ where we get λ_r by considering the Laplace transform of C_ν,

$$\hat{C}_\nu(\lambda) \;=\; \frac{\lambda}{\lambda^2 + \hat{\gamma}(\lambda)\lambda - \omega_T^2} \tag{3.18}$$

which implies that

$$\lambda_r \;=\; \frac{\omega_T^2}{\lambda_r = \hat{\gamma}(\lambda_r)} \tag{3.19}$$

It's worth noting that if the correlation function (3.14) decays quickly, meaning there is no long-term correlation, this result reduces to the normal Kramers' case. However, that is effectively saying that there is no memory in the system. If there is some memory the configuration at one time is affected by the past configurations, hence they are correlated. We could take from this that it is the high frequency

motion components near the reaction barrier are what gives this result a better rate. For example, if there are many attempted crossings sent back due to the solvent, or re-crossings, these will show up as high frequency components in the motion. That is the motion going back and forth vs. straight through the barrier region in the low friction case.

3.1.4 Tests of Stokes' Theory

While general use of Kramers' theory has proved valuable, direct and detailed tests of this theory have thus proved difficult before 2D spectroscopy. This is due to the many factors, such as enthalpic and energetic changes, that can effect reaction rates.[58] Because of the chemical exchange measurements available in 2D spectroscopy, our group was able to directly test Kramers' theory for a system, dicobalt octacarbonyl in linear alkanes, which follows the rates predicted by Kramers' theory.[37]

$Fe(CO)_5$ removes many of the concerns of Kramers' theory tests and measurements in spectroscopy due to the numerous simplifications of having identical reactants and products. There can be no entropic or entholpic effects as the reactants and products are in the same state. There is no concern about concentration changes as the reaction occurs. Moreover the equilibrium constant is always unity, regardless of temperature.

3.2 Chemical Exchange

As discussed in section 1.3.2, ultrafast chemical exchange spectroscopy is capable of determining the rate of interconversion between species within the solution by monitoring the off-axis peak heights in a 2D spectrum. We expect these off-axis peaks to grow in as the axial and equatorial carbonyls swap roles and we transfer vibration excitation from axial modes to equatorial modes by physically exchanging the excited ligands.

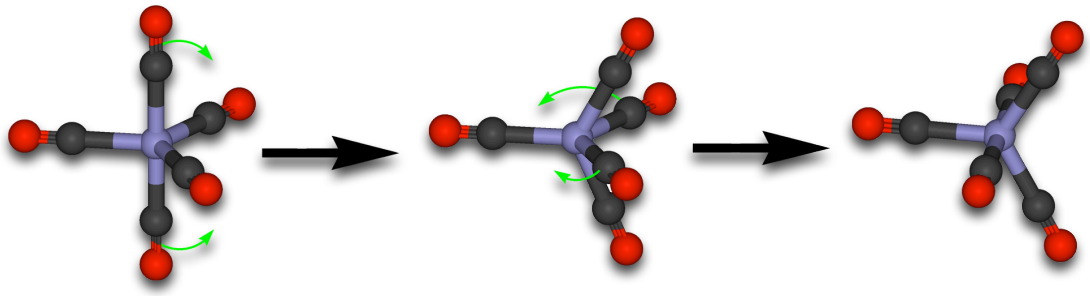

Figure 3.3: Berry pseudorotation of a trigonal bipyramidal molecule.

3.2.1 Fluxtionality

Extending our previous discussion of functionality, we consider the Berry psuedoratation mechanism in $Fe(CO)_5$.[120] This is a general feature of trigonal bipyramidal compounds which have all ligands the same. As shown in figure 3.3, 2 ligands carbonyls bend towards one another while simultaneously 2 equatorial ligands also bend towards one another, eventually switching roles of each pair within the molecule.

In many systems, 2DIR cross peak growth reports on intramolecular vibrational redistribution (IVR). Here we expect minimal IVR, as there should be minimal coupling between axial and equatorial modes. Consider the local mode Hamiltonian below.

$$\hat{H}_{CO} = \left(\begin{array}{cc|ccc} S_{ax} & J_{ax} & K & K & K \\ J_{ax} & S_{ax} & K & K & K \\ \hline K & K & S_{eq} & J_{eq} & J_{eq} \\ K & K & J_{eq} & S_{eq} & J_{eq} \\ K & K & J_{eq} & J_{eq} & S_{eq} \end{array}\right) \tag{3.20}$$

Symmetry arguments give only five unique elements, mostly in axial or equatorial blocks of the Hamiltonian in the local mode basis. In equation 3.20, the coupling

between axial and equatorial modes, K, is small compared to coupling within axial modes or within equatorial modes, J_{ax} and J_{eq} respectively. The coupling between these blocks are sufficiently small both from geometrical arrangement, minimal spectral overlap between axial equatorial modes, and a small anharmonic coupling typical of multiple coupled morse oscillators.[121]

3.2.2 Viscous, Noninteracting Solvents

In the first set of solvents, we consider varying the viscosity while maintaing relatively inert non-polar solvents. This should affect the rate of the reaction. Taking a Kramers' theory view of the reaction, basically Brownian motion on a potential, we expect solvents to have a significant effect on the rates as we are near the high friction limit. Here, we take viscosity as a proxy for the friction coefficient, as we expect to be within the high friction limit discussed in section 3.1.1.

We used a series of linear alcoves and squalene (2,6,10,15,19,23-Hexamethyltetracosa-2,6,10,14,18,22-hexaene) as our non-polar solvents. The structure of these is shown in figure 3.4.

3.2.3 Polar Solvents

The case of interacting solvents could follow different trends. Our interacting solvents are a series of alcohols, which interact through dipoles with the CO groups. Previous work showed that complexes can form between the alcohols and the iron pentacarbonyl stabilized by up to 5 kJ per mole. This should also break molecular symmetry, possibly increasing IR oscillator strength of previously Raman-only modes. Alcohols provide an OH group, which can result in hydrogen-bonding to the oxygens in carbonyls. Rose-Petruck's group previously reported on the FTIR spectra and computational results for iron pentacarbonyl in alcohols.[101] Figure 3.5 shows experimental spectra from their study. Note that the FTIR spectrum broadened with

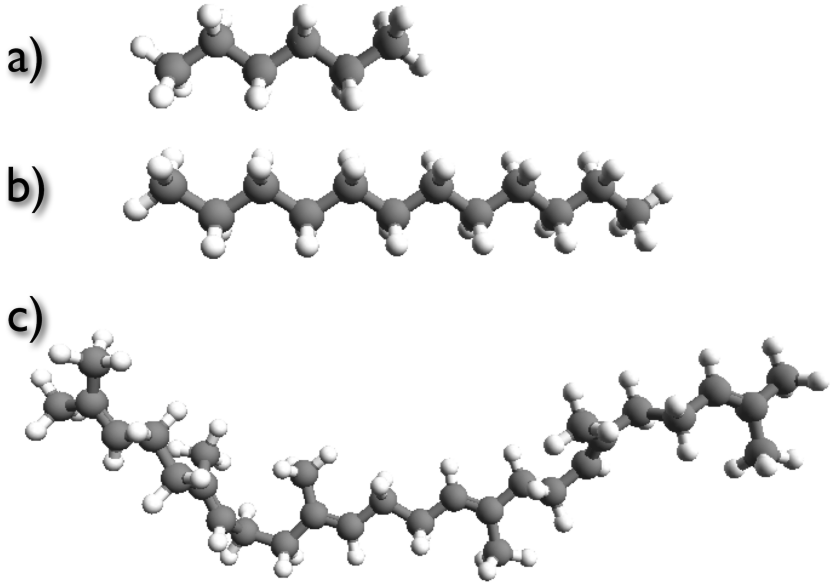

Figure 3.4: Non-polar solvents used in $Fe(CO)_5$ studies. (a) is hexane, (b) is dodecane and (c) is squalene.

shorter alcohols.

3.3 Experiments

Iron pentacarbonyl was dissolved in various solvents to get an approximate optical density in our sample cell of 0.6 OD, which provides for good 2D signal levels. Samples were then placed in a 100 μ thick sample cell and probed by 2DIR spectroscopy. Figure 3.6 shows 2DIR spectra of $Fe(CO)_5$ in two solvents, 3-octanol and dodecane. Each sample has a spectrum shown for two t_2 waiting times, 0.5 ps and 6ps. These two time delays represent an early time, before fluxtionality is expected to be important, and a later time, 6 ps, when we expect some fluxtionality to have occurred. Note the growth of cross peaks in the dotted boxes.

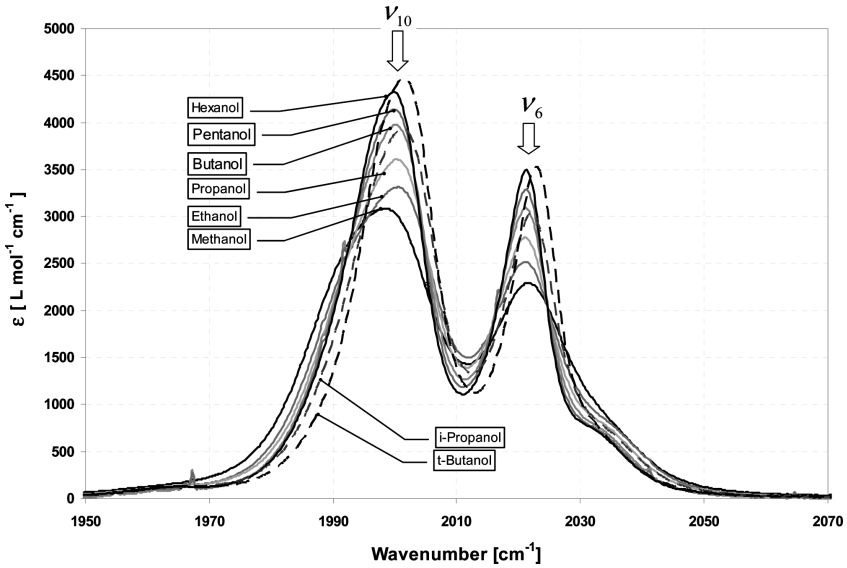

Figure 3.5: FTIR of $Fe(CO)_5$ in alcohols.[101]

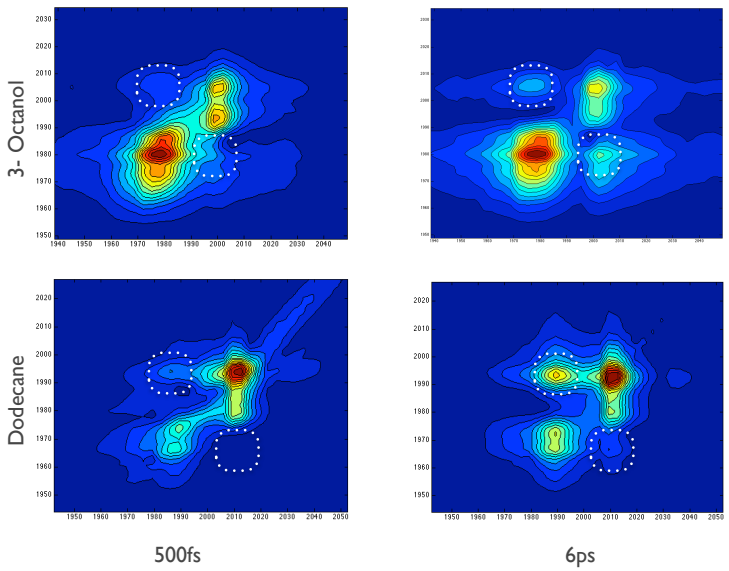

Figure 3.6: 2D spectra of Two solvents at 0.5 ps and 6ps. Cross-peak locations are emphasized with dotted boxes.

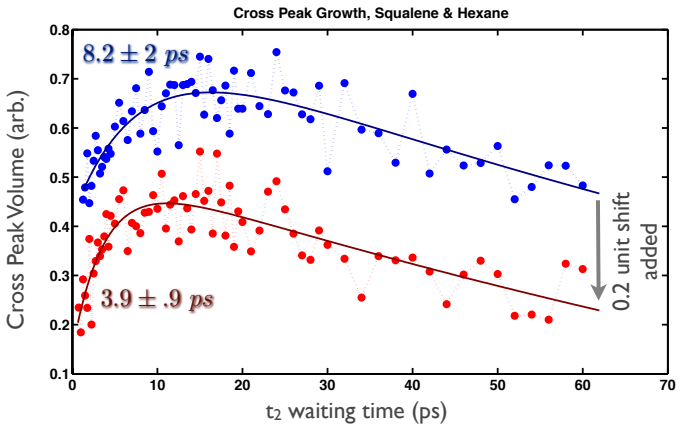

Figure 3.7: $Fe(CO)_5$ cross-peak rise-time in viscous non-polar solvents. Lower (red) points and fit are in hexane and upper (blue) points and fit are in squalene.

3.3.1 Fluxtionality Rates, Non-polar Solvents

Figure 3.7 is a comparison between hexane (red) with low viscosity (0.3 cP), and squalene (blue, 12 cP). These traces represent the integrated volume of absolute value rephasing spectra for the low to high frequency cross peak. This turns out to be the least noisy of the two cross-peaks to measure. We see a factor of two change in the growth rate; for hexane, we get 3.9 ± 0.9 ps, whereas the more viscous squalene gives 8.2 ± 2 ps. The slow vibrational decay is basically unchanged between the two solvents. Note that the lower line is offset intentionally to make the traces easier to compare. The details of the fit will be discussed in a later section.

3.3.2 Fluxtionality Rates, Alcohols

In figure 3.8, we see two cross peak growth traces for iron pentacarbonyl in ethanol and propanol. Propanol is about twice the viscosity of ethanol and should slow the functionality. It slows by about a factor of three, more than we might expect from the viscosity data earlier. Despite having higher OH density, which could stabilize a geometric configuration, ethanol allows for faster growth than the hexane by a factor of two. Based on the FTIR, ethanol broadens the iron pentacarbonyl spectrum. It's

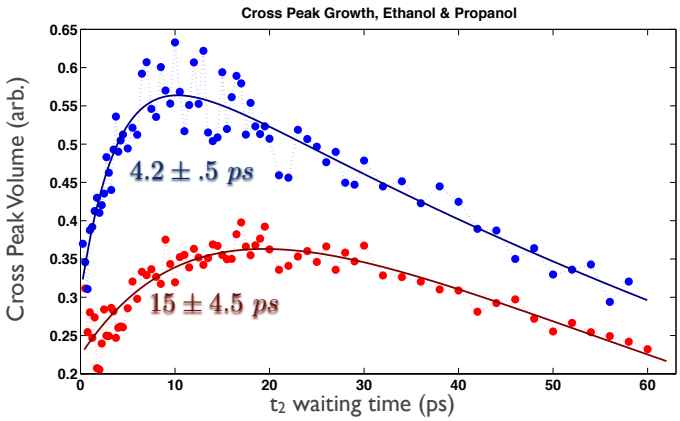

Figure 3.8: $Fe(CO)_5$ cross-peak rise-time in alcohols. Lower (red) points and fit are $Fe(CO)_5$ in Propanol and upper (blue) points and fit are in Ethanol.

possible increased IVR may occur due to the increased spectral overlap and reduced symmetry of the system, with this effect dominating any viscosity effects.

3.3.3 Data Analysis

Fitting of non-rephasing peak volume is chosen as fitting rephasing peak volume would be more complicated because the rephasing cross peaks contain oscillations due to coherence transfer.[122;123]

$$g(t) \quad = \quad e^{\frac{-t}{n}} \cdot \left(1 - ae^{\frac{-t}{m}}\right) + b, \tag{3.21}$$

where t is the time in picoseconds, a is a relative magnitude, b is an offset and m and n are time constants for rise and decay respectively.

3.4 Conclusion

In conclusion, we are able to use ultrafast chemical exchange spectroscopy, a specific application of the multidimensional spectroscopy ultrafast optics has enabled,

to monitor fluxtionality. In this case, chemical exchange reports on solvent effects in low barrier reactions. We see effects of viscosity slowing rates and possibly more complicated dynamics in interacting solvents.

CHAPTER IV

Nonequilibrium dynamics within a *de novo* Metallopeptide

Many enzymes contain metal sites that are critical to their catalytic function. Better understanding of these metal sites, such as the metal's role, the nearby structural dynamics[124], and the electrostatic environment[125–127], is of significant interest in current protein research. Moreover, work is in progress to synthesize model metal sites based on natural protein metal sites with the intention of better understanding biological mechanisms and also taking the protein's functionality and making it available to chemists in a synthetically produced, and easily modified system.[128–133] This could even allow for improvements to maximize the utility of catalytic systems inspired by enzymatic activity. From a physical chemistry perspective, these systems offer a unique opportunity to decouple and assess the relative contributions of dynamics and energetics to overall chemical activity.

Yet another application of site-specific measurements of short-times spectroscopic measurements at an active site is to inform the discussion of dynamics and electrostatics in protein function. There is an active scientific debate on the relative importance of dynamics and fluctuations[124;134;135] vs. potential energy[136;137] in protein activity.

4.1 Synthetic Metallopeptides

The Pecoraro group is interested in the production of small, ≈29 amino acid α-helical peptides that trimerize, forming a stable structure upon which functional amino acids can be added creating model motifs from natural proteins, such as those represented in figure 4.1.[129;138] These peptides are based on repetitions of the 4 amino acid sequence leucine, glutamic acid, glutamic acid, lysine (LEEK in the common amino acid alphabet.) In this sequence,leucine is a neutral and hydrophobic amino acid whereas leucine, glutamic acid and lysine are charged and hydrophilic amino acids. Since a typical α-helix is 3.6 amino acids per turn, the LEEK-based peptide has most sides hydrophilic and one stripe hydrophobic along the length of the α-helix. The N-termini of the peptides are acetylated, and the C-terminal amide upon cleavage with trifluoroacetic acid results in a terminal NH_2 group.[138] In aqueous solution the hydrophobic strips come together while the larger hydrophilic regions remain solvated. This is what allows them to form a stable trimer of parallel helices, which is not often present in natural systems which often have anti-parallel α-helices. Anti-parallel α-helices are particularly common in trans-membrane proteins, such as G protein coupled receptors.

4.1.1 Mutants

As these peptide chains are synthesized in the lab, it is simple to alter the peptide sequence. One particular series of peptide trimers, which contains a histidine substitution at the 23rd site of a 29 amino acid chain are the system for this study. Due to the trimerization, these histidines result in a 3-nitrogen binding site for copper-I, zinc-II, and other metals. For this paper the abbreviation *TRI* will represent the amino acid chain

Ac – G – WKALEEKG LKALEEK LKALEEK LKALEEK – NH2

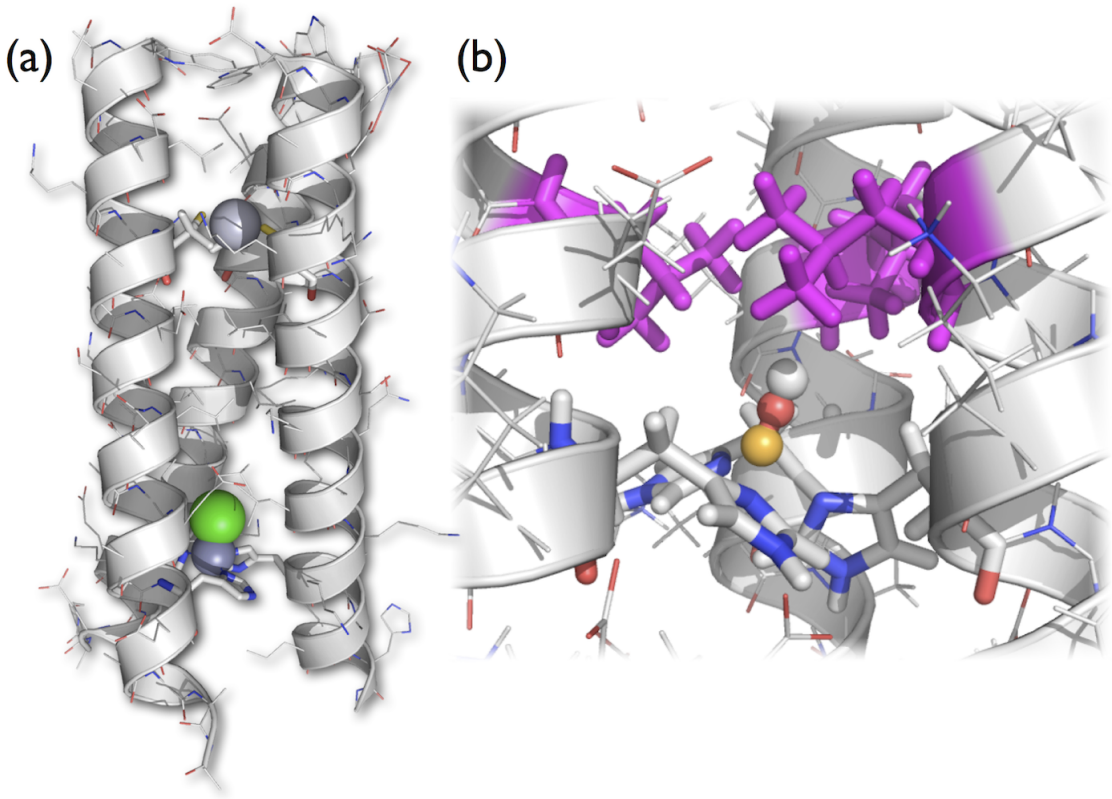

Figure 4.1: Geometry of a typical metalopeptide trimer. In this case, the two metal site $[\mathrm{Hg(II)}]_S$ $[\mathrm{Zn(II)(H_2O/OH^-)}]_N$ $(\mathrm{CSL9PenL23H})_3^{n+}$, left, based on x-ray diffraction measurements (not studied spectroscopicaly).[129] and a cartoon view of the model TRIL23H active site with Cu, C, and O added by hand, right.

which is the basis of one monomer of the peptide trimer and will be mutated with several substitutions. Most notably the 23rd site, the leucine underlined above, will be substituted with a histidine to create the metal binding site for all of our samples. A short description of the synthesis of these systems will be covered in section 4.1.2

A Cu(I) atom is ligated to the nitrogens on each of the histidines in the trimer and to a single carbonyl. The vibration of this carbonyl is the primary spectroscopic label of this work. Vibrational spectroscopy of the metal carbonyl vibration has the advantage of utilizing a relatively strong oscillator strength in an uncluttered spectral region. Moreover, in systems such as this, there is only one carbonyl ligated to a metal, so any solvation environment or dynamic information derived from spectroscopic measurements is site-specific. In contrast, vibrational spectroscopy of backbone carbonyls in peptides and proteins requires expensive isotope substitution to be site specific.[24;139]

The copper binding site of this peptide was modeled after the common motif of a metal binding site of three histidines, such as that of the Carbonic Anhydrase (CA) enzymes. Understanding the dynamics near the metal-ion containing reaction center not only aids in the understanding of this biologically important mechanism, but may improve understanding of general metal binding sites. CAs are also thought to play a significant role in a number of diseases and the study of CA inhibitors is an active area of research.[140] The active site of CA enzymes is a triple histidine site coordinating a Zn(II) ion and a water molecule. Figure 4.2 overlays the crystal structure of human CAII (hCAII) and one of the Pecoraro groups' metaloenzymes. While there is no site for water to hydrogen bond as in hCAII, the metal binding site is comparable. In our metalloprotein Zn(II) can be coordinated to the histidines, but for our spectroscopic our studies a Cu(I) ion is more convenient.

The triple histidine site with copper-I is most similar to an active site in the cytochrome C oxidase proteins. These proteins are responsible for pumping protons

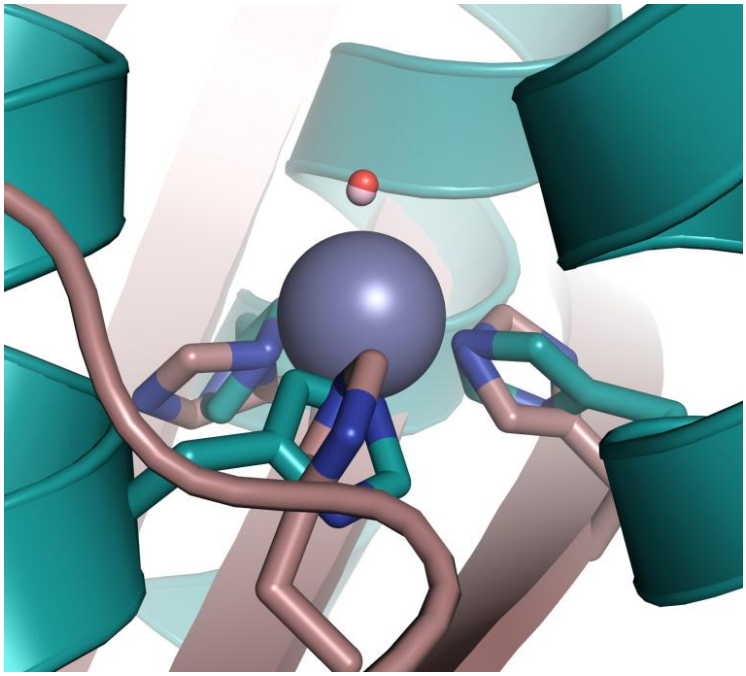

Figure 4.2: Comparison of a *de novo* metalloprotein with human CAII. Human CAII is shown in tan, where as $[\mathrm{Hg(II)}]_S[\mathrm{Zn(II)(H_2O/OH^-)}]_N(\mathrm{CSL9PenL23H})_3{}^{n+}$ is shown in cyan. From Zastrow *et. al.*[129]

across mitochondrial membranes while reducing oxygen to form water and are essential to aerobic respiration. While this protein has been extensively studied, the details of active site dynamics and energetics are not fully understood. Electron transfer paths within the protein are well established, but the mechanism of proton transfer is not fully understood.[141] Ligand exchange between sites within cytochrome c oxidase has been measured previously with pump-probe mid-infrared,[142] and a goal of ongoing work in the Kubarych group is to use multidimensional methods to look at both vibrational modes in this protein. However, the focus of this work is better understanding of the simpler model active site in the synthetic TRI peptide trimers.

In this study we look at four different peptide sequences listed in table 4.1. The sequences vary both the side-chains adjacent to the internal hydrophobic reaction cavity and the external hydrophilic side-chain groups near the binding site. This allows us to probe both for steric and electrostatic effects near the active site.

Abreviation	*Amino Acid Sequence*	*CO bound*
$TRIL23H$	$Ac{-}G{-}WKALEEKG\ LKALEEK\ LKALEEK\ \underline{\mathbf{H}}KALEEK{-}NH2$	*Yes.*
$TRIL19AL23H$	$Ac{-}G{-}WKALEEKG\ LKALEEK\ LKA\underline{\mathbf{A}}EEK\ \underline{\mathbf{H}}KALEEK{-}NH2$	*Yes*
$TRIK22QL23HK24Q$	$Ac{-}G{-}WKALEEKG\ LKALEEK\ LKALEE\underline{\mathbf{Q}}\ \underline{\mathbf{HQ}}ALEEK{-}NH2$	*Yes.*
$TRIL19IL23H$	$Ac{-}G{-}WKALEEKG\ LKALEEK\ LKA\underline{\mathbf{I}}EEK\ \underline{\mathbf{H}}KALEEK{-}NH2$	*No.*

Table 4.1: TRI-based peptides studied. Along with the sequence, we note if CO was found to bind Cu(I) in the given mutant. All mutants with a bond CO were studied by 2DIR

While this work only looks at trimers made of identical peptide sequences, heterogeneous trimers are also possible, as well as many more potential substitutions within the peptide sequence. These and other modifications will be the topic of future work in the Kubarych group.

4.1.2 Sample Preparation

Sample preparation was preformed by the Pecoraro group and involved peptide synthesis, followed by isolation, and finally dilution in a D_2O based 4-(2-hydroxyethyl)-1-piperazineethanesulfonic acid buffer (also known as HEPES) at pH 7.5. Concentrations are kept high enough to get maximal 2DIR signal without the peptides forming larger aggregations, typically about 3.3 mM of peptide trimers. a Tetrakis(acetonitrile)copper(I) tetrafluoroborate salt was then added to provide Cu^+ ions which would then bind with the histidine trimers in the peptides. Finally CO was bubbled through the samples to form the Cu-CO spectroscopic labels within the peptides.

Air sensitivity limited useful sample life to 4-8 hours. Such a short sample lifetime, would be potentially limiting to many 2DIR groups, but allowed for ample time for our data collection due to the speed advantages of continuous motor scanning and chirped pulse upconversion methods used in our lab.[86]

4.2 2DIR

A typical 2DIR spectrum of the base TRIL23H system is shown in figure 4.3. The 2D plot correlates absorption frequency (horizontal) with emission frequency (vertical) of the system at a given waiting time between absorption and emission. The sample 2D spectrum is at .25 ps waiting time delay, but the typical range in our experiments is up to 200 ps of delay. In the 2D spectra of figure 4.3, we are looking at the vibration of the carbon-oxygen bond of the CO coordinated to a copper(I) ion at the histidine binding site of our model peptide trimer. As there is a single carbonyl that has vibrations in the 1900 - 2100 cm^{-1} region, we are only sensitive to the carbonyl near the active site. This CO absorbs at a frequency of 2063 cm^{-1}, which causes a Ground State Bleach (GSB) peak at (2063 cm^{-1}, 2063 cm^{-1}) in the 2D plot. This corresponds to optical labeling of the first vibrational transition and then detecting the first vibrational transition again at a later time.

The elongation along the diagonal is due to vibrational oscillators in slightly varied environments absorbing and emitting at slightly different frequencies, the inhomogeneous broadening. Inhomogenious broadening, a portion of which is static on the timescale of these experiments, is common in proteins and represents a measure of the number of different microstates the protein can exist in. Because proteins typically require a relatively long time to interconvert between structures, the time scale for complete spectral diffusion is often longer than can easily be probed by our system.

The peak at (2063 cm^{-1}, 2038 cm^{-1}) represents an Excited State Absorption (ESA) with a 25 cm^{-1} anharmonicity in the CO oscillator potential. This system demonstrates a large anharmonicity compared to many vibrational states, but in-line with previous measurements of single metal carbonyls in proteins, such as the 21 cm^{-1} anharmonicity reported for iron carbonyl on the heme of myoglobin and hemoglobin.[70;143]

2D spectra are often taken at many waiting times to provide additional time-

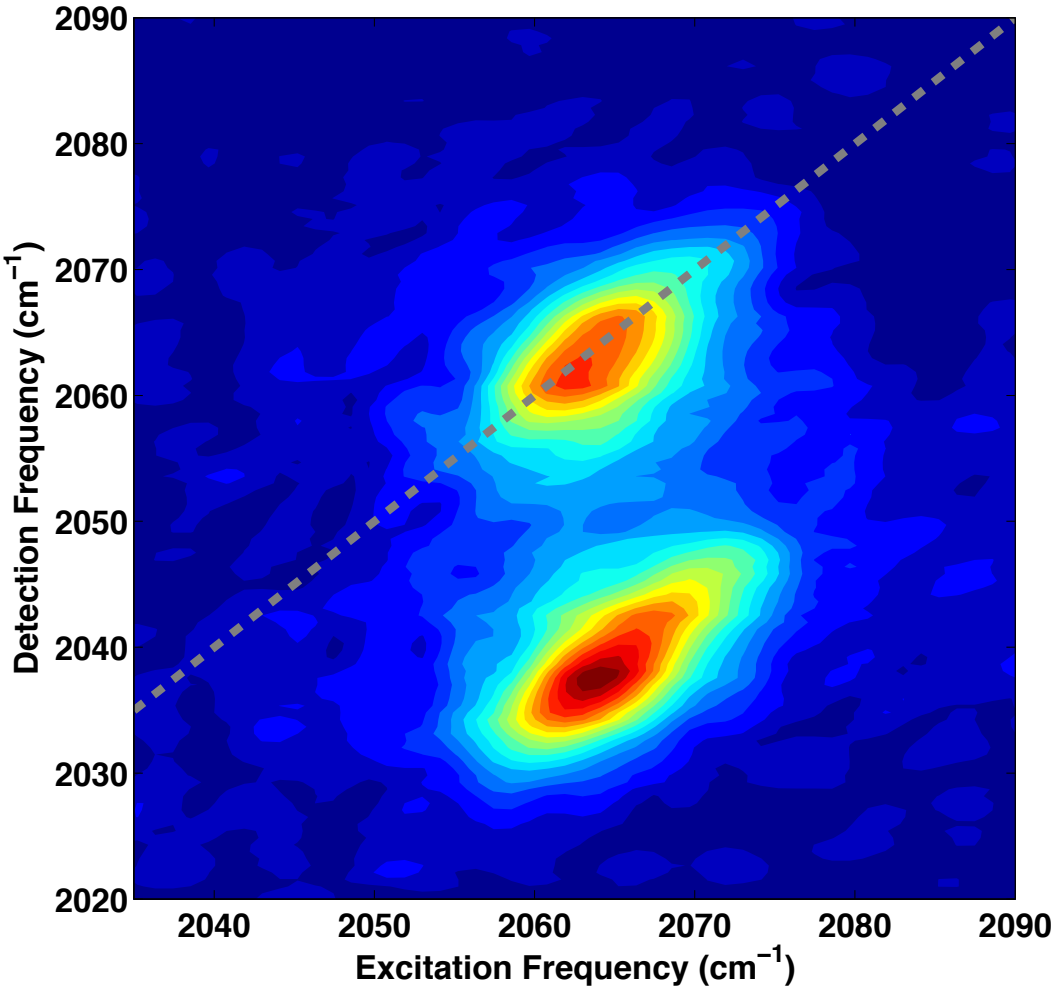

Figure 4.3: A typical 2DIR spectrum of the peptide - Cu - CO complex. In this case, TRIL23H taken at $t_2 = 0.25$ ps.

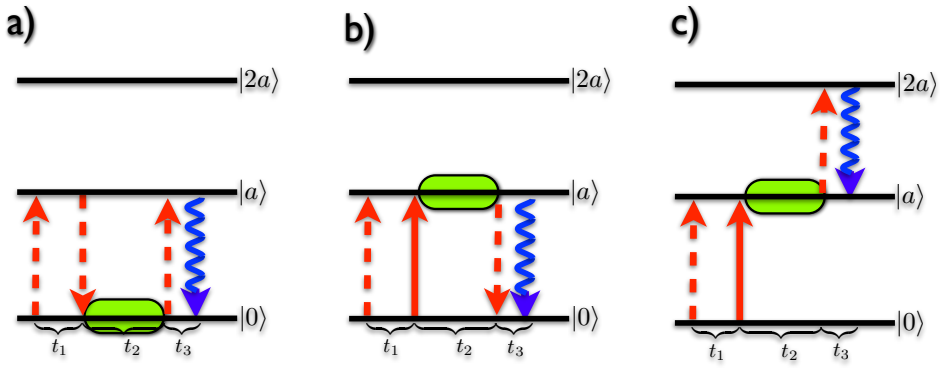

Figure 4.4: Feynman diagrams for the TRI-peptide 2DIR. The state where the system spends the t_2 waiting time is indicated with the green oval. (a) and (b) are contributions to the ground state bleach peak and (c) contributes to the excited state absorption.

dependent information that helps to track the dynamical evolution of the system within its surroundings. Figure 4.5 shows 2DIR spectra after waiting times varying from 0.25 ps to 1.75 ps. The intensity of these peaks represents the decay due to vibrational relaxation during these 2.25 ps of system evolution. The peak shape relates to spectral diffusion of the vibrational mode. Note that the anti-diagonal lines apparent in the 1.25 ps and 1.75 ps spectra is due to interference of scattered beams in the signal direction and is a systematic noise.

4.2.1 Vibrational Population Decay

The vibrational decay of TRIL23H in D_2O is shown in figure 4.6. We observe a biexponential vibrational decay with a time constants of 2.3 $\pm$ 1 ps and 24 $\pm$ 2 ps. The observed vibrational decays are comparable to previously reported decays in heme proteins.[143;144] A relatively long vibrational lifetime is consistent with the relatively sparse bath modes available to absorb energy from the vibration as it decays. Moreover, there are no other internal modes for Intramolecular Vibrational Redistribution (IVR).

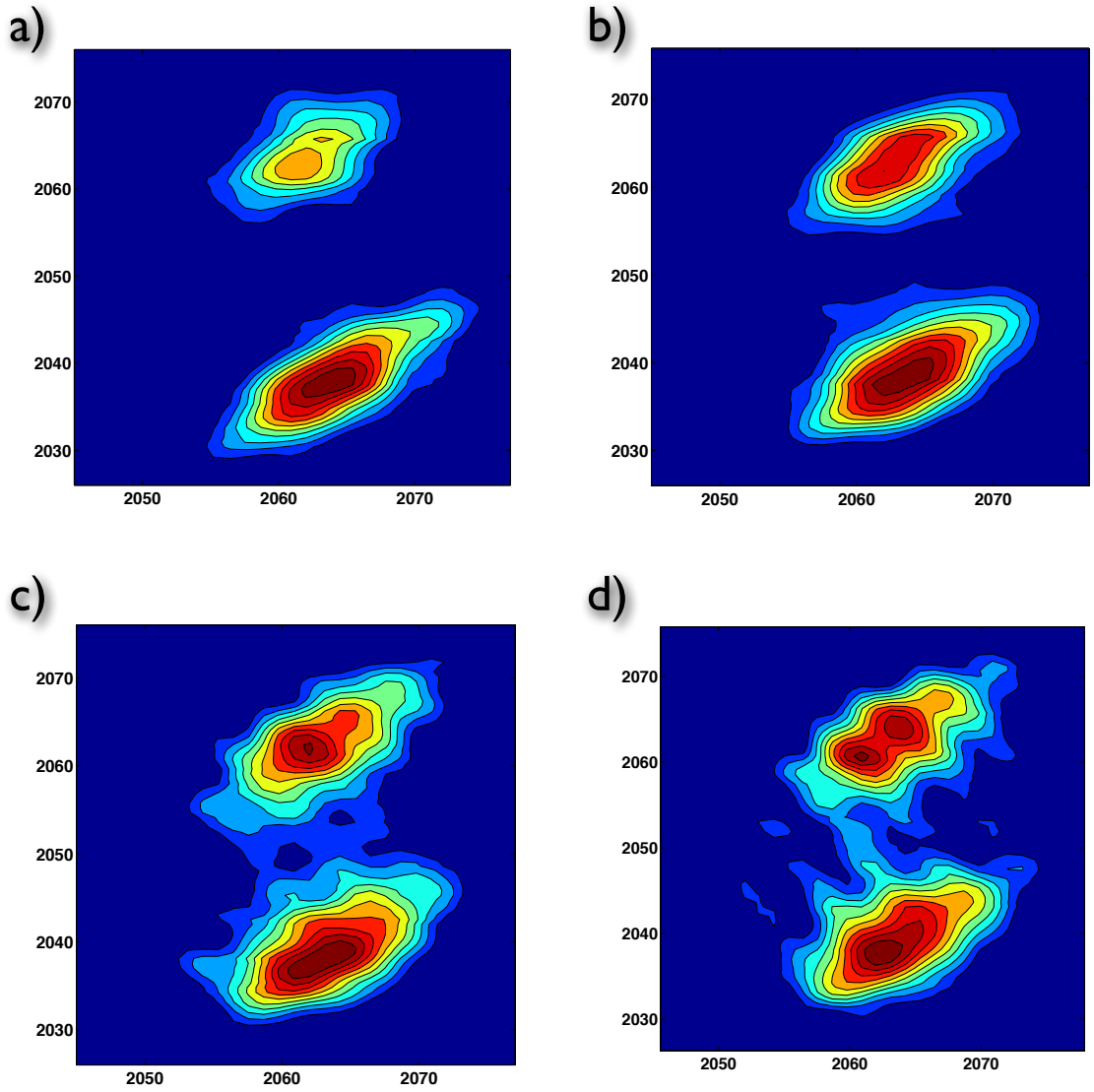

Figure 4.5: 2DIR of TRIL23H at several t_2 waiting times. Times are (a) 0.25ps, (b) 0.75ps (c) 1.25 ps (d) 1.75 ps. Note that the anti-diagonal lines showing up in the 1.25 ps and 1.75 ps spectra is due to scattering, a systematic source of noise.

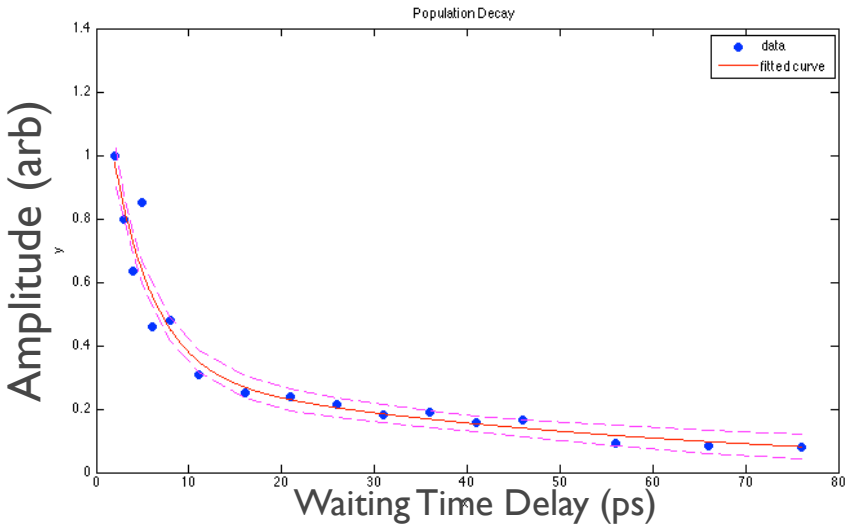

Figure 4.6: Typical vibrational population decay of the carbonyl vibration in a trimeric peptide - Cu - CO complex. In this case the TRIL23H peptide. All axes have units of cm^{-1}

4.2.2 Spectral Diffusion

The line shape in multidimensional spectra are essential for isolating homogenous and inhomogeneous broadening contributions to the overall spectral band. For details on this measurement see section 1.3.3. The shape changes of the ESA peak are cleaner in this data due to lower anti-diagonal scattering interference. The section on spectral diffusion shows data that is analyzed using a quantitative measure of shape effects, the inhomogeneous index.[36;64] For this work the inhomogeneous index will be used for determining the FFCF.[61;63;65]

In figures 4.3 and 4.5a to 4.5c, we see an anharmonic peak elongated parallel to the diagonal. This is reasonable due to the same argument for the main peak portion of the system that is in the $\nu_{CO} = 1$ excited state during the waiting time is anharmonically shifted may not able to sample all possible system microstates before being detected.

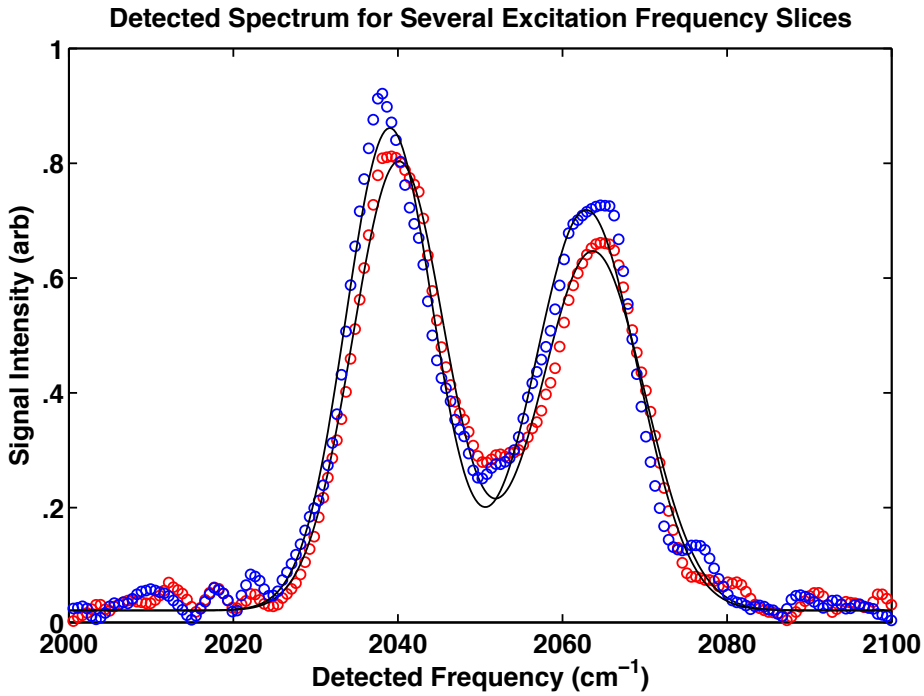

Figure 4.7: Dipole vs. carbon-oxygen separation.

4.2.3 Anharmonicity

2DIR readily reports the anharmonic shifts in vibrational excitations. Even when shifts are too small to be easily resolved in a pump-probe spectrum, the extra spectral separation of 2D helps to resolve anharmonicly shifted peaks. This is because the short-waiting time 2D peaks are narrowed along the anti-diagonal at, or near, the homogenous line width. In pump-probe an anharmonic peak still has the full in homogenous line width, which may impede observation of a small anharmonicty. As discussed above, figure 4.3 shows a typical 2D spectrum of the carbonyl vibration in our TRIL23H Cu-CO system. While this spectrum does not have the maximum spectral resolution possible in our experimental setup as it is the absolute value of a rephasing spectrum, the separation of the anharmonicly shifted ESA peak is clearly visible below the GSB peak.

The typical anharmonicity, after the observed relaxation, is in the range of 19 cm^{-1} to 22cm^{-1} for these peptide mutants. This value is comparable for anharmonicities reported previously for CO ligated to a heme iron in myoglobin[143]. However, we find, unexpectedly, this anharmonicity is *time dependent*. Figure 4.8 shows a typical time dependance of the anharmonicity in the L23H mutant. We observe a relaxation timescale of 2.0±.2 ps. We attribute this to a shift in the geometry of the ground electronic state due to vibrational excitation, to be discussed in a moment.

In order to extract anharmoicities systematically, a two-gaussian model

$$g(\omega) \quad = \quad ae^{-\frac{(\omega-\omega_0)^2}{\sigma_0}} + be^{-\frac{(\omega-\omega_{an})^2}{\sigma_{an}}} \tag{4.1}$$

was fit to $\omega_1 = const.$ slices from the 2DIR data. ω_0, ω_{an}, σ_0, σ_{an}, a, and b are all left as parameters for the nonlinear search to fit. A sample set of slices and the resulting fits is shown in figure 4.7. These fits are used with the model in equation (4.1) with parameters determined by the nonlinear fit function in Matlab. When this procedure is repeated for many slices and waiting times, we are able to obtain statistics and time dependance of the carbonyl stretch anharmonicity. This is shown in figure 4.8 for TRIL23H. This trace shows the anharmonicity shifting from near 25 cm^{-1} down to 21 cm^{-1} over the course of about 4 ps. A fit of this decay to an exponential gives a time constant of about 2 ps for the decay, depending on mutant. For most mutants we see very little change in the timescale for this shift in anharmonicity or spectral diffusion. Notably, the TRIK22QL23HK24Q mutant, did not show any appreciable difference in spectral diffusion, lifetime, anharmonicity, or excitation frequency. This is all despite a change of six charged residues to neutral residues. CO is well known to shift vibrational frequencies in an electric field, so any change should have been detected.[145] This would suggest that any electrostatic change is either shielded by counter-ions and polarization of the nearby peptide backbone and solvent.

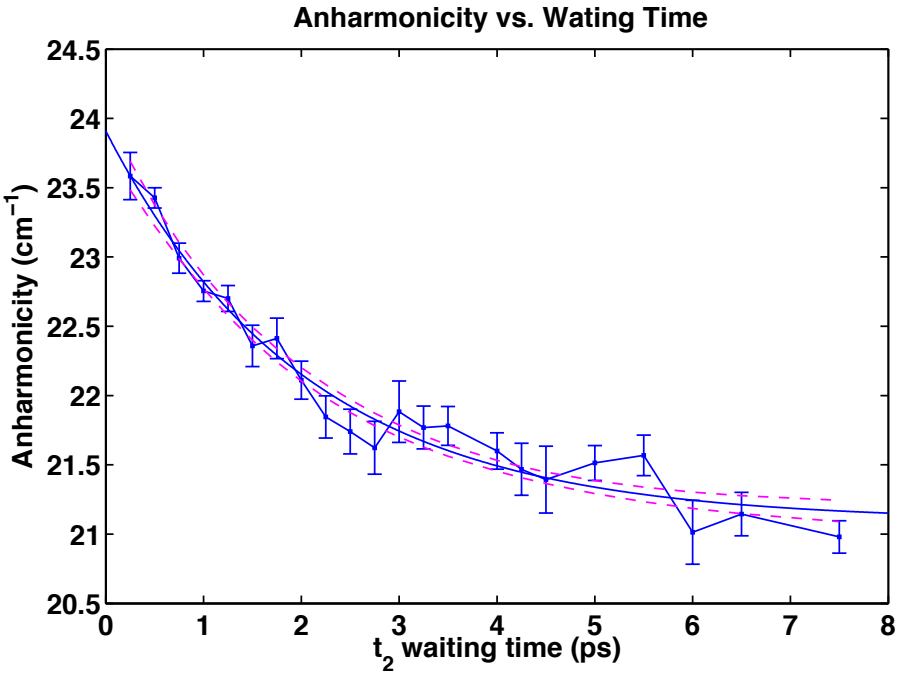

Figure 4.8: Time-dependent anharmonicity shift of the CO vibration in a trimeric peptide - Cu - CO complex. Plotted here is data for the TRIL23H version of the peptide and an exponential fit to the data. The dashed lines represent a standard deviation of uncertainty in the fit.

The TRIL19IL23H mutant changed the leucine at the 19 site, just above the Cu-CO binding site to an isoleucine. This change resulted in a mutant which did not bind CO. As such we were not able to study this mutant with the carbonyl vibration. However, it is useful to know this relatively minor modification was sufficient to exclude the CO, thus giving us some information on the active site cavity.

4.3 Excited State Vibrational Shifts

A previously reported property of carbonyl groups serves as an impetus to investigate electronic structure effects dependent on vibrational state in carbonyl.[146;147] The carbonyl average nuclear separation, determined by the vibrational state, is found to have a large effect on the geometry of the metal carbon bond.That is, the electronic structure and bonding of the system is dependent on the vibrational state. The short bond length of the CO triple bond in the vibrational ground state reverses the simple expectation for the CO dipole. A simple prediction based on electronegativity would predict the oxygen to have a partial negative charge whereas the Carbon atom has the partial negative charge in the vibrational ground state of the real molecule. Once excited to a higher vibrational state, the electronic distribution returns to the elementary physical chemistry prediction of a partial negative charge on the oxygen. Figure 4.9 gives the expected dipole for a lone CO at various bond lengths. Note the excited states are both the opposite sign and larger in magnitude than the ground state dipole.

An additional consideration may be the electrostatic environment of the CO dipole in the peptide trimer. In these α-helical bundles, there is a significant permanent dipole which is oriented with respect to the peptide and thus the carbonyl site. The aligned peptide bonds of the α-helix backbone add to produce an ≈ 300 Debye dipole for the trimer. Symmetry arguments imply the dipole field is oriented parallel to the central axis of the trimer resulting in an electric field that remains in the same direc-

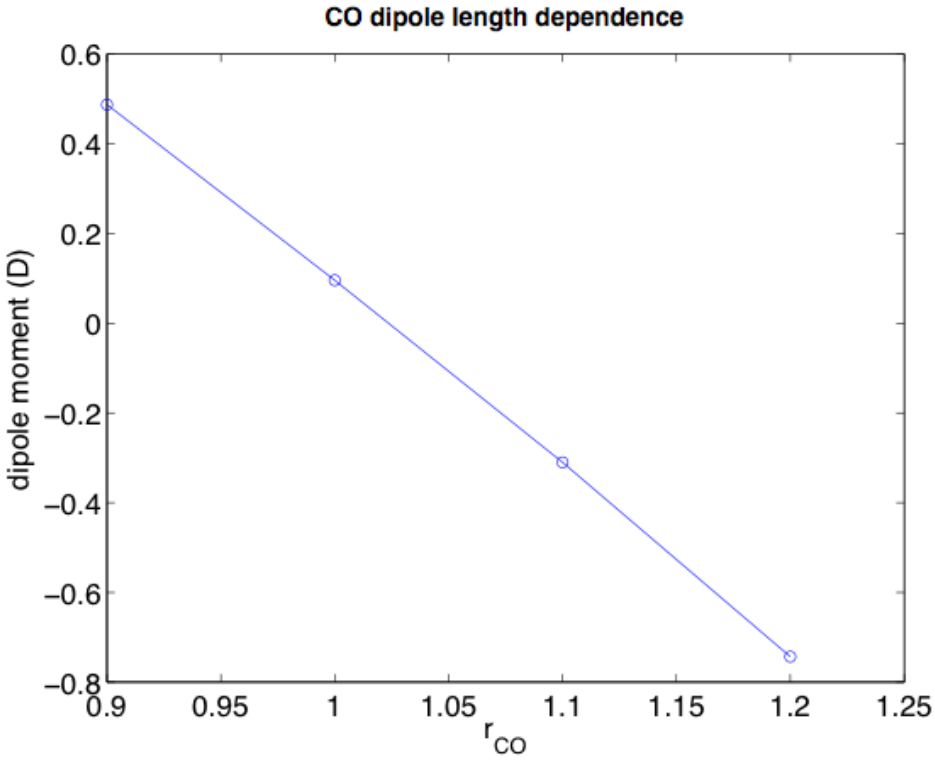

Figure 4.9: Dipole vs carbon-oxygen separation. The relatively large anharmonicity of this system results in an approximate 10% lengthening of the CO bond due to vibrational excitation. This lengthening changes the sign and amplitude of the dipole as shown here.

tion after the CO dipole flips due to the bond elongation associated with vibrational excitation. It remains to be calculated how much of an electric field would be present at the CO binding site and if this electric field, combined with the CO dipole could further influence the CO dynamics.

While it is not new to observe a time-dependent anharmonicity in vibrational modes as a molecule and nearby solvent molecules rearrange as the result of an electronic excitation,[148–150] this observation is novel in that all the observed dynamics are on the electronic ground state with a timescale an order of magnitude faster than the decay of the excited state. It should be noted that previous studies of similar shifts in vibrational states have typically involved electrostatic redistribution due to an excited electronic state, whereas our system stays in the electronic ground state throughout the measurement. Previous studies of vibrational Stark effects in water, while on the ground state, have been published, however, in these studies the shifts were on a timescale comparable to the vibrational relaxation or were not due to an actual shift of the dipole but rather evolution on the same potential energy surface.[151]

4.3.0.1 Spectral Diffusion

Spectral diffusion is one of the measurements unique to multidimensional spectroscopy. Recall that by comparing the elliptically of a peak in the 2D spectra or equivalently relative intensities of rephasing and non-rephasing spectra,[63] we can measure the rates at which any given oscillator samples accessible microstates of the system. For details on this measurements, see section 1.3.3. For the peptide, this should report on the timescales for dynamics within the active site as well as timescales for rearrangement of the side chains and protein backbone near the active site.

Figure 4.10 shows a decay of the frequency-frequency correlation function as measured in our time-stepped 2D spectra. In this case, a biexponential fit shows decays

of $1.18 \pm .5$ ps and 37.8 ± 1.4 ps. The fast decay likely represents redistribution of vibrational energy due to the motion of the atoms and side-chains nearest the CO oscillator. The slow decay is a timescale that could be side-chain motions in the peptide, but comparison to simulation must be done to make definitive conclusions.

In the case of TRIL23H, we see the decay most of the way back to zero, indicating that there is little spectral diffusion on longer timescales. This can be interpreted as the oscillator sampling most available microstates during the time scale of the measurement with few remaining conformations. If there was reorganization of the tertiary structure, spectral diffusion would include a longer timescale contribution as this motion would not occur on the timescale available to our measurements. Thus this measurement also supports the idea that there are relatively few deep local minima in the global potential energy space of the peptide. If multiple deep minima did occur, the systems would not have time to interconvert between them during our measurement and we would see a static offset representing frequency correlation due to dynamics restricted to any given local potential well. Stated another way,we would expect the spectral diffusion to not fully decay as carbonyls limited to sampling microstates near one deep local minimal would not be able to sample microstates near a different deep minima as was discussed in section 1.3.3 and shown in figure 1.9.

Spectral diffusion on the GSB and the ESA are not the same. Figure 4.4 showed the three pathways for this measurement. Figures 4.4a and 4.4b contribute to the GSB but only 4.4c contributes to the ESA. Equations (4.2) to (4.4) show the frequency frequency correlation functions for these paths.

$$C_{00}(\tau) = \langle \delta\omega_{01}(0)\delta\omega_{01}(\tau)\rangle \tag{4.2}$$

$$C_{00'}(\tau) = \langle \delta\omega_{01}(0)\delta\omega'_{10}(\tau)\rangle \tag{4.3}$$

$$C_{01'}(\tau) = \langle \delta\omega_{01}(0)\delta\omega'_{12}(\tau)\rangle \tag{4.4}$$

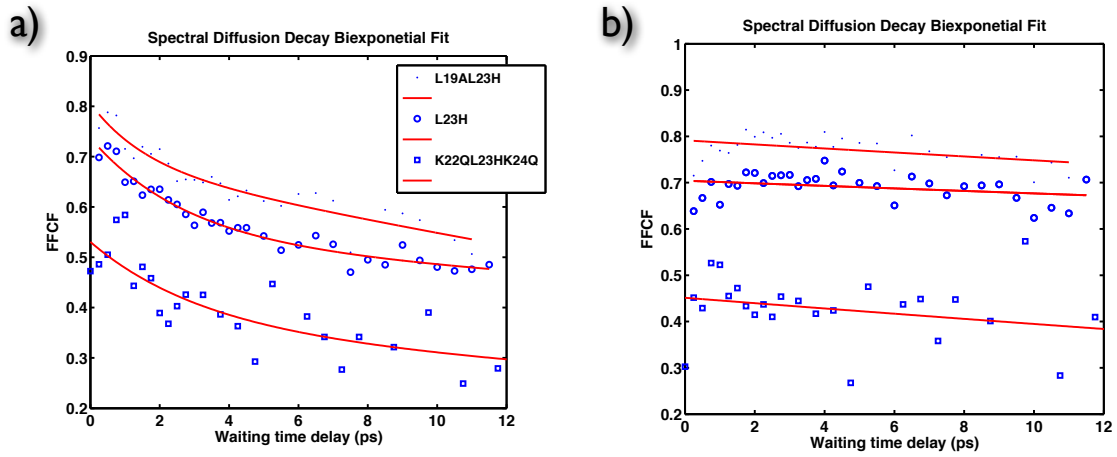

Figure 4.10: Spectral diffusion of the CO vibration in several trimeric peptide - Cu - CO complexes. Note the ESA spectral diffusions (a) shows both a fast and slow component whereas the GSB spectral diffusion (b) shows only a single slow component.

$\delta\omega_{ab}$ represents the fluctuation in the frequency of the transition from a to b. Primed frequencies are taken to be from the first excited state. Equation (4.2) represents the frequency frequency correlation function connecting ground state frequencies at the initial time with later times. This correlation function should provide relatively long timescale spectral diffusion typical of a protein environment. Equation (4.3) represents the FFCF connecting ground state frequencies at the initial time with later frequencies from the initial state back down to the ground state. As we expect geometric reorganization in the excited vibrational state, spectral diffusion could be much faster. Moreover, calculations to be discussed later indicate a significant shift in the frequencies of oscillation after such a geometrical reorganization has occurred. Equation (4.4) represents the cross correlation function of the frequency at the initial time and then the anharmonically shifted frequency from the first to second excited state at a later time.

Figure 4.10 shows the spectral diffusion for the carbonyl vibration in the TRIL23H

mutant. Note that the GSB trace shows only one long timescale decay. This is likely peptide fluctuations around carbonyl. Equation (4.3) indicates that there should be a biexponential decay of the GSB trace. It is our belief that the component related to equation (4.3) is too fast to observe on account of the geometrical rearrangement and related spectral changes as predicted by the Gaussian calculations. The biexponential distribution of the ESA spectral diffusion, related to equations (4.4), could represent both the geometrical redistribution and protein fluctuations.

4.4 Temperature Dependent FTIR

As an initial survey of temperature dependent dynamics, FTIR spectra of the TRIL23H mutant were taken over the range of -2C to 78C, see figure 4.11. While there are spectral changes, there is little evidence of the peptide losing it's structure, based on the amide bands. The Cu-CO mode at 2063 cm^{-1} shows no major shift, so it was decided that temperature dependent 2D was unlikely to show significant changes in the time available for measurements before the sample degrades. the very broad background from 1800 cm^{-1} to 2100 cm^{-1} is a water combination band which increases in intensity at higher temperatures.

4.5 Simulations

Previously papers have reported on the expected dipole moment of CO in protein environments.[147] In order to understand the anharmonicity relaxation electronic structure calculations of CO on a Cu(I) - imidizole electronic structure was studied using Gaussian[152] and the resulting potential surfaces were used to help understand excited vibrational state dynamics.

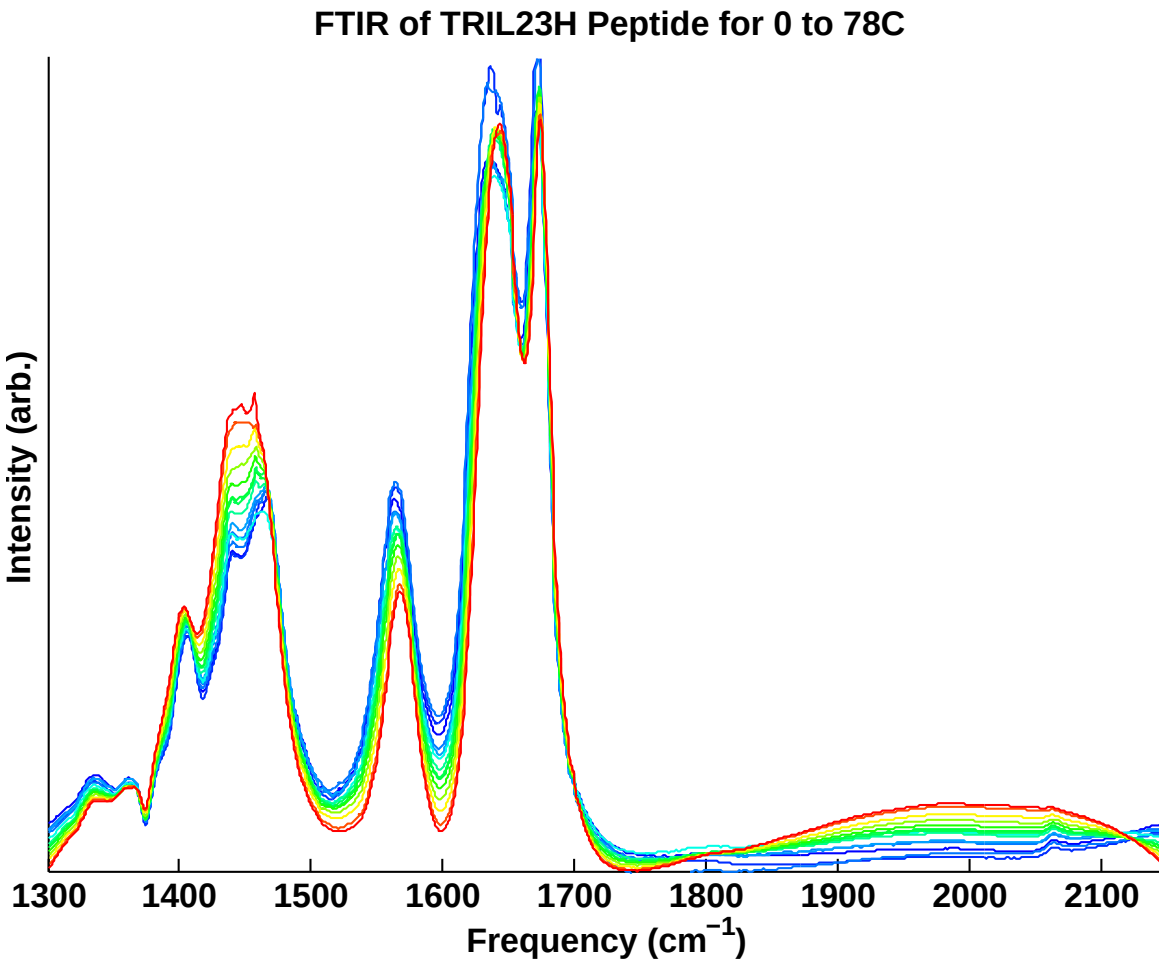

Figure 4.11: Temperature-dependent FTIR spectra of TRIL23H. Considering the large range of -2C to 78C, the peptide shows only minor changes in the spectra.

4.6 Experiments for Comparison

In order to better understand the behavior of single metal carbonyls, we considered a control experiment using a new iron carbonyl compound in D_2O produced by the Kodanko group at Wayne State University.[153] This compound is $[Fe^{(II)}(CO)(N4Py)](ClO_4)_2$ which we have been abbreviating CORM-4 internally. While it would be preferred to study a copper-I compound with similar bonding geometries, there are relatively few metal carbonyls that are water soluble.

Figure 4.12 shows a comparison of the 2D spectrum and anharmonic time dependance for TRIL23H (4.12a-c) and then CORM-4 small molecule (4.12d-f) Figure 4.12a is the structure of the TRIL23H peptide and figure 4.12b is the 2D spectra previously shown. Figure 4.12c is the decay of the anharmonicity previously shown. Figures 4.12d - 4.12f are the same for the CORM-4 molecule. CORM-4 has more inhomogenious broadening in water than CuCO in TRI, so the spectra are very different at t_0. One should expect that there is little space for the carbonyl to reorient in this system as the other organic ligands crowd the iron site. That could limit inhomogenious broadening, but the exposure to the solvent is a much larger effect. Figure 4.12f is the same double gaussian fit applied to get the anharmonicity of the TRI systems, but here the trend shows no significant time-dependance. This could mean that the time-dependance is a function of the peptide around the Cu-CO or unique to the Cu-CO system. This warrants further investigation.

4.6.1 Electronic Structure

Figure 4.13 shows the optimized system that was used in the Gaussian 09 simulations. These simulations were run with B3LYP level of theory and LANL2DZ basis set for copper. Other atoms had the 6-31+G(d) basis set. We found that, even without an external field, the CO was likely to change geometry upon lengthening of the CO bond by the amount expected to correspond to the first vibrational excited state.

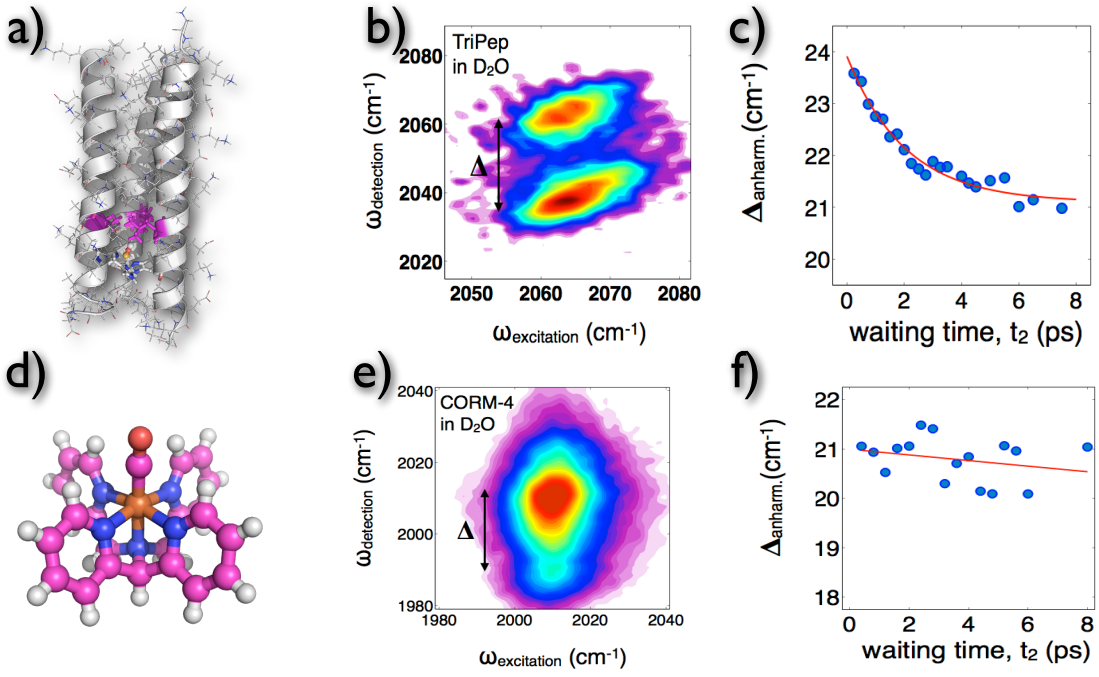

Figure 4.12: Comparison between TRIL23H and CORM-4.

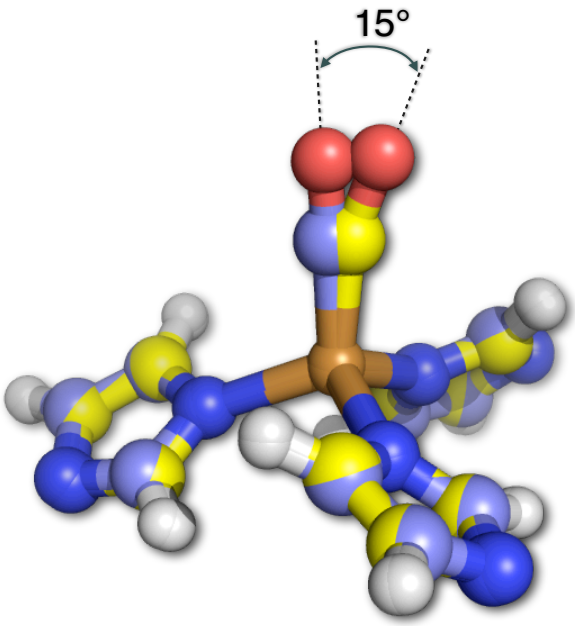

Figure 4.13: Calculated geometries of Cu-Co on three imidizoles. Blue carbon atoms represent the optimized geometry for the CO bond length of the ground vibrational state. Yellow carbon atoms represent the optimized geometry for the CO with a bond distance of the first excited vibrational state. Note the 17° shift in the CO bond angle.

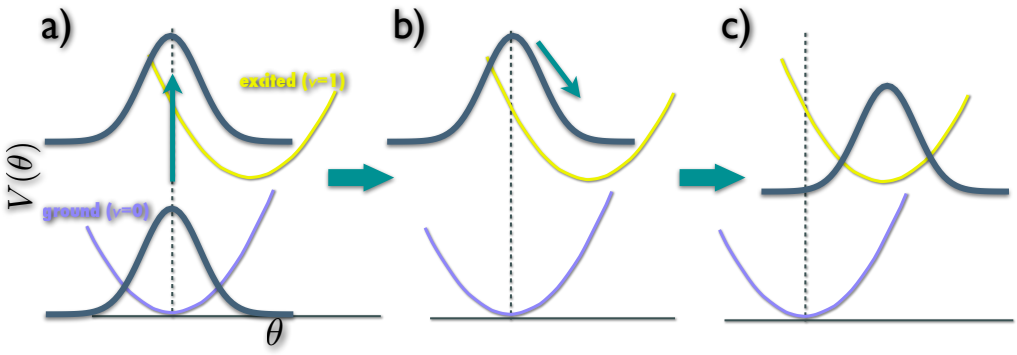

Figure 4.14: Cartoon of angular rearrangement upon vibrational excitation.(a) Represents the excitation of the ground vibrational state angular distribution onto the excited vibrational state potential energy surface. (b) represents the relaxation of the distribution while on the excited state angular potential. (c) is the relaxed excited state angular distribution.

Calculations suggest that the carbonyl its ground state aligns approximately parallel to the TRI peptide axis. However, in the $\nu = 1$ excited vibrational state the carbonyl changes its orientation by approximately 15° off of the central axis. Figure 4.14 shows a cartoon the this process of geometrical change upon vibrational excitation. Figure 4.14a shows the excitation from an equilibrium distribution of angles on the ground vibrational state to that same angular distribution on the excited vibrational state potential. Figure 4.14b indicates that, upon excitation to the excited state, the distribution of angles is no longer the expected equilibrium distribution. Taking simple classical mechanics Langevin equation approach, we can predict how the distribution of angles on this new potential will change as a function of time, and eventually reach the expected equilibrium state as shown in figure 4.14c.

Figure 4.15 shows the evolution of the angular probability distribution as calculated by numerical propagation of the Langevin differential equation in Matlab. This is equivalent to equation (3.2) generalized to spherical coordinates. The ground state equilibrium distribution, a Boltzmann distribution for 300K, is placed on the

excited state potential. The evolution of the distribution is calculated based on 2000 trajectories with random initial conditions from the ground state distribution. The potentials used in this simulation are from Gaussian calculations of the potential energy dependance as a function of polar angle θ and azimuthal angle ϕ, shown in figure 4.16. Notably we see a fast highly damped evolution of the distribution from the ground state angular distribution to the excited state distribution. A Gaussian white noise random force was added as the random driving force, $R(t)$ in equation (3.2). It should be noted that these simulations use a friction model for η based on a bulk friction and slip-stick conditions. These parameters were manually selected to give a decay comparable to that in figure 4.8. It is a short-term goal to run additional simulations to better understand this parameter and inform the selection of it. The possible like of a friction term, η, is not trivial, however. There is a community of researchers working to better understand "internal friction" in proteins.

4.7 Conclusions

By the use of two-dimensional spectroscopy of a single carbonyl bound to a copper at a model active metalloenzye active site we have measured markedly different dynamics on ground and excited vibrational states. While theoretically, most systems should show some difference in ground and excited states, we find that this system has particularly distinct dynamics in ground and excites states for reasons that we are still working to understand. Previously reported time dependance of anharmonicity is most often due to solvation rearrangement after an electronic excitation whereas this system rearrangement is due to vibrational excitation. Of note, we also find a lack of dependance of nearby charges, suggesting the active site cavity is not strongly affected by electrostatics.

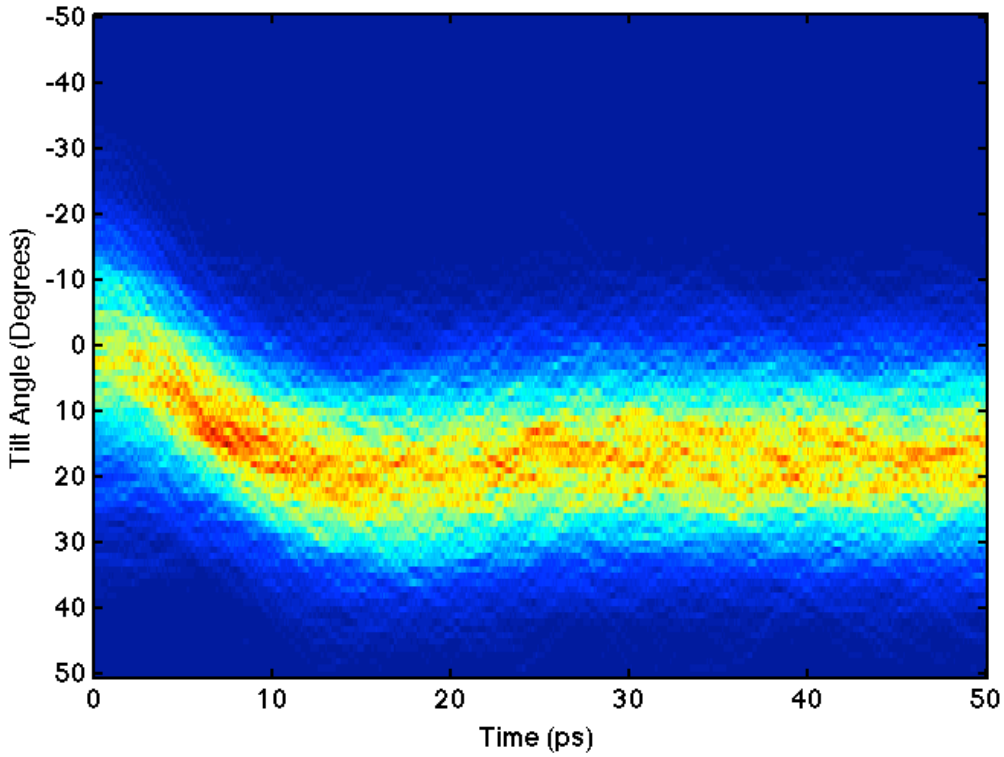

Figure 4.15: Angular probability distribution evolution on excited vibrational state.

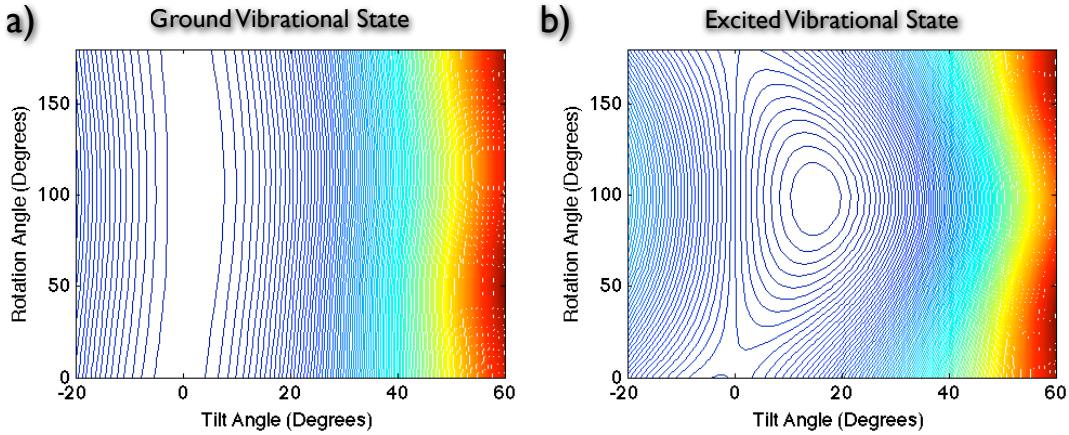

Figure 4.16: Angular potential on vibrational ground and excited states.

4.8 Acknowledgments

The author would like to thank collaborators on this project. Vince Pecoraro and Fangting Yu were critical in providing samples of the peptide systems studied. Aaron White preformed most of the numerical simulations, both Gaussian calculations and numerical simulations on the resulting potential energy surfaces. Evan Arthur was responsible for molecular dynamics simulations. John King assisted in 2D spectrum acquisition of the TRI-peptide systems and recorded 2D spectra of the CORM-4 as part of his projects. I would also like to thank the Kodanko group at Wayne State University for the samples of [$Fe^{(II)}$(CO)(N4Py)]- $(ClO_4)_2$, which we have been calling CORM-4.

CHAPTER V

Concluding Remarks and Future Work

5.1 Acoustooptic Pulse Shaping in the Mid-Infrared

Chapter 2 discussed the building, testing, and initial 2DIR spectra obtained with a mid-infrared pulse shaping system based on an acoustooptic modulator capable of measuring 2DIR absorptive spectra of several metal carbonyls in various solvents. The flexibility of outputting a unique pulse shape for each laser shot at a 1-kHz repetition rate allows us to take full advantage of our laser repetition rate, reducing low-frequency drift, while enabling measurements of thousands of unique pump conditions in only seconds. This apparatus, though still clearly technically demanding to implement, provides a powerful tool for 2DIR, coherent control, or other experiments requiring many pump pulse configurations.

There are numerous potential uses for this system. First and foremost, the shaper system will be used for 2DIR spectroscopy where it offers several key advantages over the background-free approach, such as in the detection of absorptive 2DIR spectra or in dealing with samples with high levels of scattering. The phase matching of the pump-probe geometry naturally yields absorptive 2D spectra, which can be separated into rephasing and non-rephasing, if desired, using a phase cycling scheme originally developed in the visible.[79] Absorptive spectra have the highest spectral resolution but their measurement requires additional phasing steps when implemented with

in the background-free geometry, including a pump-probe spectrum.[29;30] The phase cycling used for transient absorption and background removal also removes the sample scattering that is a significant source of noise in 2D spectra of weak absorptions.

Because the shaper system relies on software to produce the pulse sequence or pulse properties in the pump beam, it is relatively easy to implement many forms of alternative pulse sequences programmatically. For example, quantum process tomography previously discussed in Chapter 1 has been implemented by modulating the pump amplitude as a function of frequency, preferentially exciting a particular mode followed by a broad-band probe of all other vibrational modes. The use of an active pulse shaping system for QPT measurements enables rapid and straightforward variation of the pump beam spectrum compared with a passive optical approach. Unfortunately, clean data has not yet been taken with the QPT sequence, but this should work be accomplished with some additional experimental effort.

An additional area in which pulse shaping has traditionally been used in ultrafast optics is coherent control, where a pump-probe experiment is done in with a pump shape that is varied so as to optimize some experimental outcome. It has long been a dream of optical physics to selectively break molecular bonds using laser light in order to prepare reacting species that are improbable under purely thermal conditions. Since IR spectroscopy is limited to making optical transitions from the ground state to excited system eigenstates, which often resemble the normal mode vibrations, it is rarely the case than IR excitation can selectively elongate a single chemical bond without also exciting other neighboring bonds. By exciting carefully prepared coherent superpositions of system eigenstates, for example by using a genetic algorithm, it should be possible to effectively transform, albeit transiently, the normal mode basis to the local mode basis and drive energy into a specific molecular bond. That is one may find a combination of frequencies and phases that excite modes adding to a specific local mode evolution. Coherent control can also be used to preferentially

select one of two products in a photo-triggered reaction.[14;16] Naturally a pulse shaper is central to this type of experiment because the variety of pulse shapes that can be produced by exclusively passive pulse shaping methods is very limited and these experiments are most powerful when a great variety of pulse shapes are possible.

A potential new type of spectroscopy that could be attempted in the mid-infrared with this system is a semi-classical approximation to the newly developed quantum-optical spectroscopy.[19;154] This form of spectroscopy includes consideration of the quantum nature of the light source. Unfortunately, very few optical sources are available that produce the squeezed and stretched quantum-optical states which are required for these measurements.[154] The most recent implementation relies on a classical pump-probe experiment combined with theoretical modeling of the sample to provide the quantum-optical response.[19] By making a measurement with a known fluctuation to the optical pump pulse, a semi-classical approximation to the stretched and/or squeezed optical state may be possible, which should, in principle, provide a better approximation to the quantum-optical response than a simple transform-limited pump pulse and thus require less modeling to retrieve the quantum-optical response. This is a new idea and I am not aware of any attempts to do this type of measurement with an actively modulated pump pulse.

5.2 Solvation of Iron Pentacarbonyl

Chapter 3 described studies of the iron pentacarbonyl fluxtionality by the Berry psuedorotaton mechanism in liquid solution. In particular, we found that high viscosity solvents slow the kinetics of fluxtionality, as one would expect based on Kramers Theory. The iron pentacarbonyl response to a series of alcohols is somewhat more complicated and may require additional molecular dynamics simulations to fully understand. Some cases of the iron pentacarbonyl system may have solvent structures that may cause deviations from the standard Kramers Theory response. Just as in the

work by Anna *et. al.*, showed that cyclohexane can form a preferential solvent structure around dicobalt octacarbonyl,[37] there may be a solvent cage changing the solvent solute interactions for iron pentacarbonyl in some cases. There is clear evidence from our own work on $Mn_2(CO)_{10}$ in the linear alcohol series[38] that the solvents do not act like a continuum, causing marked variations in IVR dynamics that correlate with the average number of hydrogen bonds formed with the solvent. A similar effect is likely at play in the IPC reaction system, and future work to characterize solvation shell structure will help to elucidate the molecularity of the solvent. It is also known that polar solvents generally reduce the symmetry of small molecule complexes, which lends IR transition strength to otherwise exclusively Raman active transitions. Accompanying this lowering in symmetry should also be some degree of loosening of the rigid segregation of axial and equatorial modes, a key requirement for cross-peak growth to correspond directly to chemical exchange. Hence, it is likely that IVR will also contribute to the observed cross-peak evolution, a contribution that can be isolated using temperature dependent measurements. That is, the activated barrier crossing is dramatically more temperature sensitive than is IVR, a phenomenon that was leveraged in earlier work on $Co_2(CO)_8$ to assess the contribution of IVR to cross peak evolution[37]. Chemical exchange offers a novel and powerful probe of ground electronic state chemical reactions, and this work is only the second study to explicitly examine the solvent dependence of activated barrier crossings, a topic that has long been fundamental to our understanding of condensed phase reaction dynamics.

5.3 Nonequilibrium dynamics within a *de novo* Metallopeptide

Chapter 4 discussed the dynamics of a model active site in a synthetic peptide. By measuring 2DIR spectroscopy of a carbonyl bound within this active site, we

were able to show that the anharmonicity is, unexpectedly, time-dependent. This observation could be compared to a dynamic Stark effect in experiments measuring vibrational changes on an excited electronic state. However, this has not been seen for a molecule on its electronic ground state when the vibrational lifetime is long compared to the timescale of this shift. We attribute this shift to a geometrical rearrangement which changes the energy levels of the carbonyl within the model active site. Or, expressed differently, the CO evolves on a multidimensional potential surface, where excitation of the CO stretch launches bending motion of the Cu-C-O bond angle. Hence, this system exhibits the vibrational analogue of impulsive vibrational motion induced by vertical electronic excitation of Franck-Condon active vibrations. A key difference is that in the present case due to the very low frequency of the bending mode ($<$60 cm^{-1}), and its overdamped relaxation due to the tightly pack protein interior, there are no observable coherent oscillations. Experiments were preformed on several mutants and, for those mutants that bind CO, no significant change was observed for the timescale of this anharmonicity shift. This observation suggests that the local bonding of the Cu site dominates the dynamics relative to non-bonding interactions with the internal side chains.

Because these peptide trimers are synthetic, it is very easy to change the amino acid sequence used, providing access to many different active site conditions. In this report, the only modifications studied were to the relative size and density of the active site via the packing of hydrophobic residues just above the active site, and electrostatic effects by modifying the charged, hydrophilic residues on the protein exterior. The relative insensitivity of the measured timescales to these changes may indicate that more significant changes may be needed in order to see an effect, or that the metal binding site is overwhelmingly responsible for the ligand dynamics. Future work on the system will include denaturation by changing pH and additional mutations such as changes to the electrostatics near the active site, moving the active

site to different locations within the peptide trimer, or using hetero-trimers where not all of the α-helices are the same. Also, further numerical simulations are required to fully understand the active site dynamics with a vibrationally excited CO. Due to a low signal-to-noise ratio, the above experiments may also benefit from additional averaging of 2D spectra which has not been done.

Additional, more dramatic changes that can be made to the peptide system include the movement of the active site to the alternate end of the peptide where rather than being contained within a region closer to the central core of the peptide, the active site would actually be positioned in the more flexible terminal region. This could test for the degree to which the rigidity of the active site plays a role in the observed non-equilibrium dynamics by moving the active site closer to the end of the peptide where the local structure is presumably more flexible. More importantly, however, this modification would presumably be able to alter the accessibility of actual substrate molecules that are catalyzed by the de novo enzyme.

Moreover, an additional experiment which could help identify the geometrical re-arrangement we expect is anisotropy measurements. These measurements would be able to show if there is in fact an angular change in the carbonyl orientation after excitation. Moreover, this measurement could be made more sensitive by aligning the large dipole moment of the peptide trimer along the laser polarization with an electric field, thus enhancing the sensitivity of an anisotropy experiment by increasing the effective absorption of the pump pulse and narrowing the initial angular distribution giving a cleaner signal. Ultimately we hope to be able to correlate the measured ultrafast dynamics with biochemical assays of the engineered enzymes catalytic activity, and to possibly assess the relative importance of static energetics and dynamical fluctuations in the function of the enzyme. The dynamics versus energetics debate is a long one in the biophysics and enzymology communities, and this work offers a new window that promises to combine dynamical experiments, atomistic simulations

and classical enzymology to address catalysis using a systematic, physical approach. Both systems studied and described in this dissertation are essentially used to address the same key challenge: How can we experimentally deduce the dynamical influence of a condensed phase environment on the fate of a chemical reaction? In both cases two-dimensional infrared spectroscopy is able to provide essential data, either through equilibrium chemical exchange or via nonequilibrium anharmonicity and inhomogeneity dynamics. These data alone represent a significant contribution to our appreciation for the subtle role played by the environment, and they will inspire further experimental, synthetic, and theoretical efforts to extract all of the dynamical secrets that, without 2DIR spectroscopy, are fundamentally hidden beneath the linear, 1D absorption spectrum.

BIBLIOGRAPHY

BIBLIOGRAPHY

[1] J. Kubelka, J. Hofrichter, and W. Eaton, "The protein folding 'speed limit'," *Current opinion in structural biology*, vol. 14, no. 1, pp. 76–88, 2004.

[2] J. Loparo, S. Roberts, and A. Tokmakoff, "Multidimensional infrared spectroscopy of water. II. Hydrogen bond switching dynamics," *The Journal of chemical physics*, vol. 125, p. 194522, 2006.

[3] J. T. King, M. R. Ross, and K. J. Kubarych, "Ultrafast α-Like Relaxation of a Fragile Glass-Forming Liquid Measured Using Two-Dimensional Infrared Spectroscopy," *Phys. Rev. Lett.*, vol. 108, p. 157401, Apr 2012.

[4] H. Bovenkerk, F. Bundy, H. Hall, H. Strong, and R. Wentorf, "Preparation of diamond," *Nature*, vol. 184, no. 4693, pp. 1094–8, 1959.

[5] K. Lewis and J. Ogilvie, "Probing photosynthetic energy and charge transfer with two-dimensional electronic spectroscopy," *The Journal of Physical Chemistry Letters*, 2012.

[6] G. Engel, T. Calhoun, E. Read, T. Ahn, T. Mančal, Y. Cheng, R. Blankenship, and G. Fleming, "Evidence for wavelike energy transfer through quantum coherence in photosynthetic systems," *Nature*, vol. 446, no. 7137, pp. 782–786, 2007.

[7] C. Middleton, P. Marek, P. Cao, C. Chiu, S. Singh, A. Woys, J. de Pablo, D. Raleigh, and M. Zanni, "Two-dimensional infrared spectroscopy reveals the complex behaviour of an amyloid fibril inhibitor," *Nature Chemistry*, 2012.

[8] C. Froehly, B. Colombeau, and M. Vampouille, "Shaping and analysis of picosecond light pulses," in *Progress in Optics* (E. Wolf, ed.), vol. 20, pp. 65–, Amsterdam: North-Holland, 1983.

[9] A. Weiner, D. Leaird, G. Wiederrecht, and K. Nelson, "Femtosecond pulse sequences used for optical manipulation of molecular motion," *Science*, vol. 247, no. 4948, p. 1317, 1990.

[10] A. Weiner, "Femtosecond pulse shaping using spatial light modulators," *Review of Scientific Instruments*, vol. 71, p. 1929, 2000.

[11] S. Shim, D. Strasfeld, and M. Zanni, "Generation and characterization of phase and amplitude shaped femtosecond mid-ir pulses," *Optics express*, vol. 14, no. 26, pp. 13120–13130, 2006.

[12] S. Shim, D. Strasfeld, Y. Ling, and M. Zanni, "Automated 2d ir spectroscopy using a mid-ir pulse shaper and application of this technology to the human islet amyloid polypeptide," *Proceedings of the National Academy of Sciences*, vol. 104, no. 36, p. 14197, 2007.

[13] S. Shim and M. Zanni, "How to turn your pump–probe instrument into a multidimensional spectrometer: 2d ir and vis spectroscopies via pulse shaping," *Phys. Chem. Chem. Phys.*, vol. 11, no. 5, pp. 748–761, 2009.

[14] A. Peirce, M. Dahleh, and H. Rabitz, "Optimal control of quantum-mechanical systems: Existence, numerical approximation, and applications," *Physical Review A*, vol. 37, no. 12, p. 4950, 1988.

[15] S. Shi, A. Woody, and H. Rabitz, "Optimal control of selective vibrational excitation in harmonic linear chain molecules," *The Journal of chemical physics*, vol. 88, p. 6870, 1988.

[16] A. Florean, D. Cardoza, J. White, J. Lanyi, R. Sension, and P. Bucksbaum, "Control of retinal isomerization in bacteriorhodopsin in the high-intensity regime," *Proceedings of the National Academy of Sciences*, vol. 106, no. 27, pp. 10896–10900, 2009.

[17] M. Mohseni, A. Rezakhani, and D. Lidar, "Quantum-process tomography: Resource analysis of different strategies," *Physical Review A*, vol. 77, no. 3, pp. 1–15, 2008.

[18] J. Yuen-Zhou and A. Aspuru-Guzik, "Quantum process tomography of excitonic dimers from two-dimensional electronic spectroscopy. i. general theory and application to homodimers," *The Journal of chemical physics*, vol. 134, p. 134505, 2011.

[19] M. Kira, S. Koch, R. Smith, A. Hunter, and S. Cundiff, "Quantum Spectroscopy with Schrödinger-cat States," *Nature Physics*, 2011.

[20] C. Piermarocchi, "Materials spectroscopy: What would schrodinger's cat see?," *Nature Physics*, 2011.

[21] J. Zheng, K. Kwak, J. Asbury, X. Chen, I. Piletic, and M. Fayer, "Ultrafast dynamics of solute-solvent complexation observed at thermal equilibrium in real time," *Science*, vol. 309, no. 5739, pp. 1338–1343, 2005.

[22] J. Loparo, S. Roberts, and A. Tokmakoff, "2D IR Spectroscopy of Hydrogen Bond Switching in Liquid Water," in *International Conference on Ultrafast Phenomena*, Optical Society of America, 2006.

[23] M. Khalil, N. Demirdöven, and A. Tokmakoff, "Coherent 2D IR spectroscopy: Molecular structure and dynamics in solution," *The Journal of Physical Chemistry A*, vol. 107, no. 27, pp. 5258–5279, 2003.

[24] A. Remorino, I. Korendovych, Y. Wu, W. DeGrado, and R. Hochstrasser, "Residue-Specific Vibrational Echoes Yield 3D Structures of a Transmembrane Helix Dimer," *Science*, vol. 332, no. 6034, p. 1206, 2011.

[25] I. Newton, "A Letter of Mr. Isaac Newton, Professor of the Mathematicks in the University of Cambridge; Containing His New Theory about Light and Colors: Sent by the Author to the Publisher from Cambridge, Febr. 6. 1671/72; In Order to be Communicated to the R. Society," *Philosophical Transactions (1665-1678)*, vol. 6, pp. pp. 3075–3087, 1671.

[26] P. Hamm and M. Zanni, *Concepts and methods of 2D infrared spectroscopy*. Cambridge Univ Pr, 2011.

[27] R. Kubo, "A stochastic theory of line shape," *Advances in Chemical Physics*, pp. 101–127, 1969.

[28] R. Boyd, *Nonlinear Optics*. Academic Pr, 2003.

[29] M. Khalil, N. Demirdöven, and A. Tokmakoff, "Obtaining absorptive line shapes in two-dimensional infrared vibrational correlation spectra," *Physical review letters*, vol. 90, no. 4, p. 47401, 2003.

[30] J. Anna, M. Nee, C. Baiz, R. McCanne, and K. Kubarych, "Measuring absorptive two-dimensional infrared spectra using chirped-pulse upconversion detection," *JOSA B*, vol. 27, no. 3, pp. 382–393, 2010.

[31] A. Tokmakoff, "Two-dimensional line shapes derived from coherent third-order nonlinear spectroscopy," *The Journal of Physical Chemistry A*, vol. 104, no. 18, pp. 4247–4255, 2000.

[32] M. Zanni, S. Gnanakaran, J. Stenger, and R. Hochstrasser, "Heterodyned two-dimensional infrared spectroscopy of solvent-dependent conformations of acetylproline-nh2," *The Journal of Physical Chemistry B*, vol. 105, no. 28, pp. 6520–6535, 2001.

[33] M. Nee, C. Baiz, J. Anna, R. McCanne, and K. Kubarych, "Vibrational coherence decay in metal carbonyls: Solvent dependence of coherence lifetimes studied with mdir," *Ultrafast Phenomena XVI*, pp. 322–324, 2009.

[34] C. Baiz, R. McCanne, and K. Kubarych, "Structurally Selective Geminate Rebinding Dynamics of Solvent-Caged Radicals Studied with Nonequilibrium Infrared Echo Spectroscopy," *Journal of the American Chemical Society*, vol. 131, no. 38, pp. 13590–13591, 2009.

[35] M. Ji, S. Park, and K. Gaffney, "Dynamics of ion assembly in solution: 2dir spectroscopy study of lincs in benzonitrile," *The Journal of Physical Chemistry Letters*, vol. 1, no. 12, pp. 1771–1775, 2010.

[36] J. King, C. Baiz, and K. Kubarych, "Solvent-dependent spectral diffusion in a hydrogen bonded vibrational aggregate," *The Journal of Physical Chemistry A*, 2010.

[37] J. Anna and K. Kubarych, "Watching solvent friction impede ultrafast barrier crossings: A direct test of kramers theory," *The Journal of chemical physics*, vol. 133, p. 174506, 2010.

[38] J. King, J. Anna, and K. Kubarych, "Solvent-hindered intramolecular vibrational redistribution," *Phys. Chem. Chem. Phys.*, 2011.

[39] J. King, M. Ross, and K. Kubarych, "Water-Assisted Vibrational Relaxation of a Metal Carbonyl Complex Studied with Ultrafast 2D-IR," *The Journal of Physical Chemistry B*, 2012.

[40] P. Hamm, M. Lim, and R. Hochstrasser, "Structure of the amide I band of peptides measured by femtosecond nonlinear-infrared spectroscopy," *The Journal of Physical Chemistry B*, vol. 102, no. 31, pp. 6123–6138, 1998.

[41] M. Zanni and R. Hochstrasser, "Two-dimensional infrared spectroscopy: a promising new method for the time resolution of structures," *Current opinion in structural biology*, vol. 11, no. 5, pp. 516–522, 2001.

[42] A. Smith and A. Tokmakoff, "Probing local structural events in β-hairpin unfolding with transient nonlinear infrared spectroscopy," *Angewandte Chemie*, vol. 119, no. 42, pp. 8130–8133, 2007.

[43] T. Jansen and J. Knoester, "Two-dimensional infrared population transfer spectroscopy for enhancing structural markers of proteins," *Biophysical journal*, vol. 94, no. 5, pp. 1818–1825, 2008.

[44] L. DeFlores, Z. Ganim, R. Nicodemus, and A. Tokmakoff, "Amide i - ii 2d ir spectroscopy provides enhanced protein secondary structural sensitivity," *Journal of the American Chemical Society*, vol. 131, no. 9, pp. 3385–3391, 2009.

[45] M. Zanni, N. Ge, Y. Kim, and R. Hochstrasser, "Two-dimensional ir spectroscopy can be designed to eliminate the diagonal peaks and expose only the crosspeaks needed for structure determination," *Proceedings of the National Academy of Sciences of the United States of America*, vol. 98, no. 20, p. 11265, 2001.

[46] R. Ernst, G. Bodenhausen, A. Wokaun, *et al.*, *Principles of nuclear magnetic resonance in one and two dimensions*, vol. 332. Clarendon Press Oxford, 1987.

[47] E. Geva, "Graduate spectroscopy." Course Notes, 2007.

[48] S. Naraharisetty, V. Kasyanenko, and I. Rubtsov, "Bond connectivity measured via relaxation-assisted two-dimensional infrared spectroscopy," *The Journal of chemical physics*, vol. 128, p. 104502, 2008.

[49] I. Rubtsov, "Relaxation-assisted two-dimensional infrared (ra 2dir) method: Accessing distances over 10 å and measuring bond connectivity patterns," *Accounts of chemical research*, vol. 42, no. 9, pp. 1385–1394, 2009.

[50] D. Kurochkin, S. Naraharisetty, and I. Rubtsov, "A relaxation-assisted 2D IR spectroscopy method," *Proceedings of the National Academy of Sciences*, vol. 104, no. 36, p. 14209, 2007.

[51] S. Woutersen, Y. Mu, G. Stock, and P. Hamm, "Hydrogen-bond lifetime measured by time-resolved 2d-ir spectroscopy: N-methylacetamide in methanol," *Chemical Physics*, vol. 266, no. 2-3, pp. 137–147, 2001.

[52] Y. Kim and R. Hochstrasser, "Chemical exchange 2d ir of hydrogen-bond making and breaking," *Proceedings of the National Academy of Sciences of the United States of America*, vol. 102, no. 32, p. 11185, 2005.

[53] J. Zheng, K. Kwak, X. Chen, J. Asbury, and M. Fayer, "Formation and dissociation of intra-intermolecular hydrogen-bonded solute-solvent complexes: Chemical exchange two-dimensional infrared vibrational echo spectroscopy," *Journal of the American Chemical Society*, vol. 128, no. 9, pp. 2977–2987, 2006.

[54] D. Moilanen, D. Wong, D. Rosenfeld, E. Fenn, and M. Fayer, "Ion–water hydrogen-bond switching observed with 2d ir vibrational echo chemical exchange spectroscopy," *Proceedings of the National Academy of Sciences*, vol. 106, no. 2, pp. 375–380, 2009.

[55] D. Rosenfeld, K. Kwak, Z. Gengeliczki, and M. Fayer, "Hydrogen bond migration between molecular sites observed with ultrafast 2d ir chemical exchange spectroscopy," *The Journal of Physical Chemistry B*, vol. 114, no. 7, pp. 2383–2389, 2010.

[56] J. Zheng, K. Kwak, J. Xie, and M. Fayer, "Ultrafast carbon-carbon single-bond rotational isomerization in room-temperature solution," *Science*, vol. 313, no. 5795, pp. 1951–1955, 2006.

[57] J. Cahoon, K. Sawyer, J. Schlegel, and C. Harris, "Determining transition-state geometries in liquids using 2D-IR," *Science*, vol. 319, no. 5871, p. 1820, 2008.

[58] J. Anna, M. Ross, and K. Kubarych, "Dissecting enthalpic and entropic barriers to ultrafast equilibrium isomerization of a flexible molecule using 2dir chemical exchange spectroscopy," *The Journal of Physical Chemistry A*, vol. 113, no. 24, pp. 6544–6547, 2009.

[59] G. Fleming and M. Cho, "Chromophore-solvent dynamics," *Annual review of physical chemistry*, vol. 47, no. 1, pp. 109–134, 1996.

[60] S. Woutersen, Y. Mu, G. Stock, and P. Hamm, "Subpicosecond conformational dynamics of small peptides probed by two-dimensional vibrational spectroscopy," *Proceedings of the National Academy of Sciences*, vol. 98, no. 20, p. 11254, 2001.

[61] J. Asbury, T. Steinel, C. Stromberg, S. Corcelli, C. Lawrence, J. Skinner, and M. Fayer, "Water dynamics: Vibrational echo correlation spectroscopy and comparison to molecular dynamics simulations," *The Journal of Physical Chemistry A*, vol. 108, no. 7, pp. 1107–1119, 2004.

[62] P. Hamm, "Three-dimensional-IR spectroscopy: Beyond the two-point frequency fluctuation correlation function," *The Journal of chemical physics*, vol. 124, p. 124506, 2006.

[63] K. Lazonder, M. Pshenichnikov, and D. Wiersma, "Easy interpretation of optical two-dimensional correlation spectra," *Optics letters*, vol. 31, no. 22, pp. 3354–3356, 2006.

[64] S. Roberts, J. Loparo, and A. Tokmakoff, "Characterization of spectral diffusion from two-dimensional line shapes," *The Journal of chemical physics*, vol. 125, p. 084502, 2006.

[65] K. Kwak, S. Park, I. Finkelstein, and M. Fayer, "Frequency-frequency correlation functions and apodization in two-dimensional infrared vibrational echo spectroscopy: A new approach," *Journal of Chemical Physics*, vol. 127, no. 12, pp. 124503–124503, 2007.

[66] J. Asbury, T. Steinel, K. Kwak, S. Corcelli, C. Lawrence, J. Skinner, and M. Fayer, "Dynamics of water probed with vibrational echo correlation spectroscopy," *The Journal of Chemical Physics*, vol. 121, p. 12431, 2004.

[67] C. Baiz, R. McCanne, M. Nee, and K. Kubarych, "Orientational dynamics of transient molecules measured by nonequilibrium two-dimensional infrared spectroscopy," *The Journal of Physical Chemistry A*, vol. 113, no. 31, pp. 8907–8916, 2009.

[68] S. Arrivo, T. Dougherty, W. Grubbs, and E. Heilweil, "Ultrafast infrared spectroscopy of vibrational co-stretch up-pumping and relaxation dynamics of w (co) 6," *Chemical physics letters*, vol. 235, no. 3-4, pp. 247–254, 1995.

[69] V. Kleiman, S. Arrivo, J. Melinger, and E. Heilweil, "Controlling condensed-phase vibrational excitation with tailored infrared pulses," *Chemical physics*, vol. 233, no. 2-3, pp. 207–216, 1998.

[70] C. Ventalon, J. Fraser, M. Vos, A. Alexandrou, J. Martin, and M. Joffre, "Coherent vibrational climbing in carboxyhemoglobin," *Proceedings of the National Academy of Sciences of the United States of America*, vol. 101, no. 36, p. 13216, 2004.

[71] C. Wong, R. Alvey, D. Turner, K. Wilk, D. Bryant, P. Curmi, R. Silbey, and G. Scholes, "Electronic coherence lineshapes reveal hidden excitonic correlations in photosynthetic light harvesting," *Nature Chemistry*, 2012.

[72] J. Yuen-Zhou, M. Mohseni, and A. Aspuru-Guzik, "Quantum process tomography via photon echo experiments," *Arxiv preprint arXiv:1006.4866*, 2010.

[73] P. Shor, "Polynomial-time algorithms for prime factorization and discrete logarithms on a quantum computer," *Arxiv preprint quant-ph/9508027*, 1995.

[74] L. Grover, "A fast quantum mechanical algorithm for database search," in *Proceedings of the twenty-eighth annual ACM symposium on Theory of computing*, pp. 212–219, ACM, 1996.

[75] J. D. Yung, Man-hong Whitfield, S. Boixo, D. G. Tempel, and A. Aspuru-guzik, "Introduction to quantum algorithms for physics and chemistry," *Arxiv preprint*, 2012.

[76] O. Golonzka, M. Khalil, N. Demirdöven, and A. Tokmakoff, "Coupling and orientation between anharmonic vibrations characterized with two-dimensional infrared vibrational echo spectroscopy," *Journal of Chemical Physics*, vol. 115, p. 10814, 2001.

[77] C. Middleton, D. Strasfeld, and M. Zanni, "Polarization shaping in the mid-ir and polarization-based balanced heterodyne detection with application to 2d ir spectroscopy," *Optics express*, vol. 17, no. 17, pp. 14526–14533, 2009.

[78] R. Bloem, S. Garrett-Roe, H. Strzalka, P. Hamm, and P. Donaldson, "Enhancing signal detection and completely eliminating scattering using quasi-phase-cycling in 2d ir experiments," *Optics Express*, vol. 18, no. 26, pp. 27067–27078, 2010.

[79] J. Myers, K. Lewis, P. Tekavec, and J. Ogilvie, "Two-color two-dimensional fourier transform electronic spectroscopy with a pulse-shaper," *Optics express*, vol. 16, no. 22, pp. 17420–17428, 2008.

[80] H. Tan and W. Warren, "Mid infrared pulse shaping by optical parametric amplification and its application to optical free induction decay measurement," *Optics Express*, vol. 11, no. 9, pp. 1021–1028, 2003.

[81] T. Witte, K. Kompa, and M. Motzkus, "Femtosecond pulse shaping in the mid infrared by difference-frequency mixing," *Applied Physics B: Lasers and Optics*, vol. 76, no. 4, pp. 467–471, 2003.

[82] J. Prawiharjo, H. Hung, D. Hanna, and D. Shepherd, "Theoretical and numerical investigations of parametric transfer via difference-frequency generation for indirect mid-infrared pulse shaping," *JOSA B*, vol. 24, no. 4, pp. 895–905, 2007.

[83] R. A. Kaindl, M. Wurm, K. Reimann, P. Hamm, A. M. Weiner, and M. Woerner, "Generation, shaping, and characterization of intense femtosecond pulses tunable from 3 to 20 μm," *Optical Society of America B*, vol. 17, no. 12, pp. 2086–2094, 2000.

[84] G. Cerullo and S. De Silvestri, "Ultrafast optical parametric amplifiers," *Review of scientific instruments*, vol. 74, p. 1, 2003.

[85] M. R. Ross, F. Yu, J. T. King, A. M. White, E. J. Arthur, V. L. Pecoraro, and K. J. Kubarych, "Nonequilibrium Active Site Dynamics of *de novo* Metalloenzymes Probed with 2D-IR," *Ultrafast Phenomena 2012*, 2012.

[86] M. Nee, R. McCanne, K. Kubarych, and M. Joffre, "Two-dimensional infrared spectroscopy detected by chirped pulse upconversion," *Optics letters*, vol. 32, no. 6, pp. 713–715, 2007.

[87] C. Baiz and K. Kubarych, "Ultrabroadband detection of a mid-ir continuum by chirped-pulse upconversion," *Optics Letters*, vol. 36, no. 2, pp. 187–189, 2011.

[88] C. Iaconis and I. Walmsley, "Spectral phase interferometry for direct electric-field reconstruction of ultrashort optical pulses," *Optics Letters*, vol. 23, no. 10, pp. 792–794, 1998.

[89] P. Baum, S. Lochbrunner, and E. Riedle, "Zero-additional-phase spider: full characterization of visible and sub-20-fs ultraviolet pulses," *Optics letters*, vol. 29, no. 2, pp. 210–212, 2004.

[90] S. Yoshikawa, K. Shinzawa-Itoh, R. Nakashima, R. Yaono, E. Yamashita, N. Inoue, M. Yao, M. Fei, C. Libeu, T. Mizushima, H. Yamaguchi, T. Tomizaki, and T. Tsukihara, "Redox-coupled crystal structural changes in bovine heart cytochrome c oxidase," *Science*, vol. 280, pp. 1723–1729, 1998.

[91] H. Alper and J. Edward, "Reactions of iron pentacarbonyl with compounds containing the no linkage," *Canadian Journal of Chemistry*, vol. 48, no. 10, pp. 1543–1549, 1970.

[92] K. Hayakawa and H. Schmid, "Iron carbonyl induced reactions of norbornene derivatives with substituted acetylenes," *Helvetica Chimica Acta*, vol. 60, no. 7, pp. 2160–2170, 1977.

[93] G. Tanguy, B. Weinberger, and H. des Abbayes, "Catalytic phase transfer carbonylation of benzyl halides with iron pentacarbonyl.," *Tetrahedron Letters*, vol. 24, no. 37, pp. 4005–4008, 1983.

[94] T. Suzuki, O. Yamada, K. Fujita, Y. Takegami, and Y. Watanabe, "Coal hydroliquefaction using iron pentacarbonyl as a catalyst precursor," *Fuel*, vol. 63, no. 12, pp. 1706–1709, 1984.

[95] R. Massoudi, J. Kim, R. King, and A. King Jr, "Homogeneous catalysis of the reppe reaction with iron pentacarbonyl: the production of propionaldehyde and 1-propanol from ethylene," *Journal of the American Chemical Society*, vol. 109, no. 24, pp. 7428–7433, 1987.

[96] M. Periasamy, C. Rameshkumar, and A. Mukkanti, "Conversion of alkynes to cyclic imides and anhydrides using reactive iron carbonyls prepared from Fe $(CO)_5$ and $Fe_3(CO)_{12}$," *Journal of organometallic chemistry*, vol. 649, no. 2, pp. 209–213, 2002.

[97] N. Memon, S. Tse, J. Al-Sharab, H. Yamaguchi, A. Goncalves, B. Kear, Y. Jaluria, E. Andrei, and M. Chhowalla, "Flame synthesis of graphene films in open environments," *Carbon*, 2011.

[98] M. Rafique and J. Iqbal, "Production of carbon nanotubes by different routesa review," *Journal of Encapsulation and Adsorption Sciences*, vol. 1, no. 2, pp. 29–34, 2011.

[99] K. Suslick, S. Choe, A. Cichowlas, and M. Grinstaff, "Sonochemical synthesis of amorphous iron," *Nature*, vol. 353, no. 6343, pp. 414–416, 1991.

[100] B. Ahr, M. Chollet, B. Adams, E. Lunny, C. Laperle, and C. Rose-Petruck, "Picosecond x-ray absorption measurements of the ligand substitution dynamics of fe (co) 5 in ethanol," *Phys. Chem. Chem. Phys.*, vol. 13, no. 13, pp. 5590–5599, 2011.

[101] J. Lessing, X. Li, T. Lee, and C. Rose-Petruck, "Structure of solvated fe (co) 5: Complex formation during solvation in alcohols," *The Journal of Physical Chemistry A*, vol. 112, no. 11, pp. 2282–2292, 2008.

[102] J. Van't Hoff, *Etudes de dynamique chimique*. F. Muller & Co., 1884.

[103] S. Arrhenius, "On the reaction velocity of the inversion of cane sugar by acids," *Zeitschrift für physikalische Chemie*, vol. 4, p. 226, 1889.

[104] E. Carter, G. Ciccotti, J. Hynes, and R. Kapral, "Constrained reaction coordinate dynamics for the simulation of rare events," *Chemical Physics Letters*, vol. 156, no. 5, pp. 472–477, 1989.

[105] P. Heidelberger, "Fast simulation of rare events in queueing and reliability models," *ACM Transactions on Modeling and Computer Simulation*, vol. 5, pp. 43–85, January 1995.

[106] R. Allen, D. Frenkel, and P. Rein ten Wolde, "Simulating rare events in equilibrium or nonequilibrium stochastic systems," *Journal of Chemical Physics*, vol. 124, no. 2, p. 024102, 2006.

[107] J. Berryman and T. Schilling, "Sampling rare events in nonequilibrium and non-stationary systems," *Journal of Chemical Physics*, vol. 133, no. 24, p. 244101, 2010.

[108] H. Kramers, "Brownian motion in a field of force and the diffusion model of chemical reactions," *Physica*, vol. 4, pp. 284–304, 1940.

[109] P. Hänggi, P. Talkner, and M. Borkovec, "Reaction-rate theory: fifty years after Kramers," *Reveiw of Modern Physics*, vol. 62, pp. 251–341, Apr 1990.

[110] P. Hänggi, P. Talkner, and M. Borkovec, "Reaction-rate theory: fifty years after Kramers," *Reviews of Modern Physics*, vol. 62, no. 2, p. 251, 1990.

[111] G. Fleming and P. Hänggi, "Activated barrier crossing: applications in Physics, Chemistry, and Biology," *Chemistry and Biology. World Scientific, River Edge, New Jersey*, 1993.

[112] L. Longobardi, D. Massarotti, G. Rotoli, D. Stornaiuolo, G. Papari, A. Kawakami, G. P. Pepe, A. Barone, and F. Tafuri, "Thermal hopping and retrapping of a Brownian particle in the tilted periodic potential of a NbN/MgO/NbN Josephson junction," *PHYSICAL REVIEW B*, vol. 84, NOV 4 2011.

[113] Y. Zhao and W. Liang, "Charge transfer in organic molecules for solar cells: theoretical perspective," *Chem. Soc. Rev.*, vol. 41, pp. 1075–1087, 2012.

[114] S. Plotkin and J. Onuchic, "Understanding protein folding with energy landscape theory part i: basic concepts," *Quarterly Reviews of Biophysics*, vol. 35, no. 02, pp. 111–167, 2002.

[115] S. Tucker, "Variational Transition State Theory in Condensed Phases," in *New Trends in Kramers' Reaction Rate Theory* (P. Talkner and P. Hänggi, eds.), ch. 2, pp. 5–46, Kluwer Academic Pub, 1995.

[116] M. Smoluchowski, "Versuch einer mathematischen theorie der koagulationskinetik kolloider lösungen," *Z. phys. Chem*, vol. 92, no. 129-168, p. 9, 1917.

[117] J. Hynes, "Statistical mechanics of molecular motion in dense fluids," *Annual Review of Physical Chemistry*, vol. 28, no. 1, pp. 301–321, 1977.

[118] R. Grote and J. Hynes, "The stable states picture of chemical reactions. ii. rate constants for condensed and gas phase reaction models," *The Journal of Chemical Physics*, vol. 73, p. 2715, 1980.

[119] R. Grote and J. Hynes, "Energy diffusion-controlled reactions in solution," *The Journal of Chemical Physics*, vol. 77, p. 3736, 1982.

[120] R. Berry, "Correlation of rates of intramolecular tunneling processes, with application to some group v compounds," *The Journal of Chemical Physics*, vol. 32, p. 933, 1960.

[121] O. Golonzka, M. Khalil, N. Demirdöven, and A. Tokmakoff, "Coupling and orientation between anharmonic vibrations characterized with two-dimensional infrared vibrational echo spectroscopy," *The Journal of Chemical Physics*, vol. 115, p. 10814, 2001.

[122] M. Nee, C. Baiz, J. Anna, R. McCanne, and K. Kubarych, "Multilevel vibrational coherence transfer and wavepacket dynamics probed with multidimensional ir spectroscopy," *The Journal of chemical physics*, vol. 129, p. 084503, 2008.

[123] C. Baiz, K. Kubarych, and E. Geva, "Molecular Theory and Simulation of Coherence Transfer in Metal Carbonyls and Its Signature on Multidimensional Infrared Spectra," *The Journal of Physical Chemistry B*, 2011.

[124] M. Karplus, "Role of conformation transitions in adenylate kinase," *Proceedings of the National Academy of Sciences*, vol. 107, no. 17, p. E71, 2010.

[125] A. Fafarman and S. Boxer, "Nitrile bonds as infrared probes of electrostatics in ribonuclease s," *The Journal of Physical Chemistry B*, 2010.

[126] L. Xu, A. Cohen, and S. Boxer, "Electrostatic fields near the active site of human aldose reductase: 2. new inhibitors and complications due to hydrogen bonds," *Biochemistry*, 2011.

[127] A. T. Fafarmana, P. A. Sigalab, J. P. Schwansb, T. D. Fennc, D. Herschlagb, and S. G. Boxer, "Quantitative, directional measurement of electric field heterogeneity in the active site of ketosteroid isomerase," *Proceedings of the National Academy of Sciences*, vol. 109, pp. 1824–1825, February 7 2012.

[128] Y. Lu, N. Yeung, N. Sieracki, and N. Marshall, "Design of functional metalloproteins," *Nature*, vol. 460, no. 7257, pp. 855–862, 2009.

[129] M. Zastrow, A. Peacock, J. Stuckey, and V. Pecoraro, "Hydrolytic catalysis and structural stabilization in a designed metalloprotein," *Nature Chemistry*, vol. 4, no. 2, pp. 118–123, 2011.

[130] J. Kaplan and W. DeGrado, "De novo design of catalytic proteins," *Proceedings of the National Academy of Sciences of the United States of America*, vol. 101, no. 32, p. 11566, 2004.

[131] W. DeGrado, C. Summa, V. Pavone, F. Nastri, and A. Lombardi, "De novo design and structural characterization of proteins and metalloproteins," *Annual review of biochemistry*, vol. 68, no. 1, pp. 779–819, 1999.

[132] K. Oohora, S. Burazerovic, A. Onoda, Y. Wilson, T. Ward, and T. Hayashi, "Chemically programmed supramolecular assembly of hemoprotein and streptavidin with alternating alignment," *Angewandte Chemie International Edition*, 2012.

[133] M. Creus, A. Pordea, T. Rossel, A. Sardo, C. Letondor, A. Ivanova, I. LeTrong, R. Stenkamp, and T. Ward, "X-ray structure and designed evolution of an artificial transfer hydrogenase," *Angewandte Chemie International Edition*, vol. 47, no. 8, pp. 1400–1404, 2008.

[134] S. Kamerlin and A. Warshel, "At the dawn of the 21st century: Is dynamics the missing link for understanding enzyme catalysis?," *Proteins: Structure, Function, and Bioinformatics*, vol. 78, no. 6, pp. 1339–1375, 2010.

[135] G. Bhabha, J. Lee, D. Ekiert, J. Gam, I. Wilson, H. Dyson, S. Benkovic, and P. Wright, "A dynamic knockout reveals that conformational fluctuations influence the chemical step of enzyme catalysis," *Science*, vol. 332, no. 6026, p. 234, 2011.

[136] M. Roca, B. Messer, D. Hilvert, and A. Warshel, "On the relationship between folding and chemical landscapes in enzyme catalysis," *Proceedings of the National Academy of Sciences*, vol. 105, no. 37, p. 13877, 2008.

[137] A. Pisliakov, J. Cao, S. Kamerlin, and A. Warshel, "Enzyme millisecond conformational dynamics do not catalyze the chemical step," *Proceedings of the National Academy of Sciences*, vol. 106, no. 41, pp. 17359–17364, 2009.

[138] B. T. Farrer, N. P. Harris, K. E. Balchus, and V. L. Pecoraro, "Thermodynamic model for the stabilization of trigonal thiolato mercury(ii) in designed three-stranded coiled coils," *Biochemistry*, vol. 40, no. 48, pp. 14696–14705, 2001. PMID: 11724584.

[139] C. Middleton, A. Woys, S. Mukherjee, and M. Zanni, "Residue-specific structural kinetics of proteins through the union of isotope labeling, mid-ir pulse shaping, and coherent 2d ir spectroscopy," *Methods*, vol. 52, no. 1, pp. 12–22, 2010.

[140] C. Supuran, "Carbonic anhydrases: novel therapeutic applications for inhibitors and activators," *Nature Reviews Drug Discovery*, vol. 7, no. 2, pp. 168–181, 2008.

[141] T. Yamashita and G. A. Voth, "Insights into the Mechanism of Proton Transport in Cytochrome c Oxidase," *Journal of the American Chemical Society*, vol. 134, no. 2, pp. 1147–1152, 2012.

[142] J. Treuffet, K. Kubarych, J. Lambry, E. Pilet, J. Masson, J. Martin, M. Vos, M. Joffre, and A. Alexandrou, "Direct observation of ligand transfer and bond formation in cytochrome c oxidase using mid-infrared chirped-pulse upconversion," *Ultrafast Phenomena XVI*, pp. 541–543, 2009.

[143] J. Owrutsky, M. Li, B. Locke, and R. Hochstrasser, "Vibrational relaxation of the CO stretch vibration in hemoglobin-CO, myoglobin-CO, and protoheme-CO," *The Journal of Physical Chemistry*, vol. 99, no. 13, pp. 4842–4846, 1995.

[144] S. Kaziannis, J. Wright, M. Candelaresi, R. Kania, G. Greetham, A. Parker, C. Pickett, and N. Hunt, "The role of cn and co ligands in the vibrational relaxation dynamics of model compounds of the [fefe]-hydrogenase enzyme," *Phys. Chem. Chem. Phys.*, vol. 13, no. 21, pp. 10295–10305, 2011.

[145] E. Park and S. Boxer, "Origins of the sensitivity of molecular vibrations to electric fields: Carbonyl and nitrosyl stretches in model compounds and proteins," *The Journal of Physical Chemistry B*, vol. 106, no. 22, pp. 5800–5806, 2002.

[146] M. Devereux, N. Plattner, and M. Meuwly, "Application of multipolar charge models and molecular dynamics simulations to study stark shifts in inhomogeneous electric fields," *The Journal of Physical Chemistry A*, vol. 113, no. 47, pp. 13199–13209, 2009.

[147] N. Plattner and M. Meuwly, "The role of higher co-multipole moments in understanding the dynamics of photodissociated carbonmonoxide in myoglobin," *Biophysical Journal*, vol. 94, no. 7, pp. 2505–2515, 2008.

[148] P. Changenet-Barret, C. T. Choma, E. F. Gooding, W. F. DeGrado, and R. M. Hochstrasser, "Ultrafast dielectric response of proteins from dynamics stokes shifting of coumarin in calmodulin," *The Journal of Physical Chemistry B*, vol. 104, no. 39, pp. 9322–9329, 2000.

[149] S. Boxer, "Stark realities," *The Journal of Physical Chemistry B*, vol. 0, no. 0, 0000.

[150] C. Baiz and K. Kubarych, "Ultrafast vibrational stark-effect spectroscopy: Exploring charge-transfer reactions by directly monitoring the solvation shell response," *Journal of the American Chemical Society*, 2010.

[151] P. Theulé, A. Callegari, T. Rizzo, and J. Muenter, "Dipole moments of hdo in highly excited vibrational states measured by stark induced photofragment quantum beat spectroscopy," *The Journal of chemical physics*, vol. 122, p. 124312, 2005.

[152] M. J. Frisch, G. W. Trucks, H. B. Schlegel, G. E. Scuseria, M. A. Robb, J. R. Cheeseman, G. Scalmani, V. Barone, B. Mennucci, G. A. Petersson, H. Nakatsuji, M. Caricato, X. Li, H. P. Hratchian, A. F. Izmaylov, J. Bloino, G. Zheng, J. L. Sonnenberg, M. Hada, M. Ehara, K. Toyota, R. Fukuda, J. Hasegawa, M. Ishida, T. Nakajima, Y. Honda, O. Kitao, H. Nakai, T. Vreven, J. A. Montgomery, Jr., J. E. Peralta, F. Ogliaro, M. Bearpark, J. J. Heyd, E. Brothers, K. N. Kudin, V. N. Staroverov, R. Kobayashi, J. Normand, K. Raghavachari, A. Rendell, J. C. Burant, S. S. Iyengar, J. Tomasi, M. Cossi, N. Rega, J. M. Millam, M. Klene, J. E. Knox, J. B. Cross, V. Bakken, C. Adamo, J. Jaramillo, R. Gomperts, R. E. Stratmann, O. Yazyev, A. J. Austin, R. Cammi, C. Pomelli, J. W. Ochterski, R. L. Martin, K. Morokuma, V. G. Zakrzewski, G. A. Voth, P. Salvador, J. J. Dannenberg, S. Dapprich, A. D. Daniels, Ö. Farkas, J. B.

Foresman, J. V. Ortiz, J. Cioslowski, and D. J. Fox, "Gaussian 09 Revision A.1."

[153] C. Jackson, S. Schmitt, Q. Dou, and J. Kodanko, "Synthesis, characterization, and reactivity of the stable iron carbonyl complex [fe (co)(n4py)](clo$_4$) 2: Photoactivated carbon monoxide release, growth inhibitory activity, and peptide ligation," *Inorganic Chemistry*, 2011.

[154] M. Lobino, D. Korystov, C. Kupchak, E. Figueroa, B. Sanders, and A. Lvovsky, "Complete characterization of quantum-optical processes," *Science*, vol. 322, no. 5901, pp. 563–566, 2008.